Using Machine Learning and Computer Simulations to Analyse Neuronal Activity in the Cerebellar Nuclei During Absence Epilepsy

Parimala Alva

October 2015

Submitted to the University of Hertfordshire in partial
fulfilment of the requirements of the degree of
Doctor of Philosophy

Acknowledgements

First and foremost, I would like to express sincere gratitude to my supervisors: Dr. Volker Steuber, Dr. Neil Davey and Prof. Rod Adams. In this research, I had the opportunity to learn and implement a variety of techniques thanks to their expert guidance. I benefitted hugely from their combined knowledge and different styles of supervision. I could not have asked for a better team of supervisors.

I would like to thank my collaborators, Freek and his team for the experimental data, inputs and constructive criticisms.

A warm thank you to my friends: Parivash, Maria, Weam, Kirsty, Dimitris, Sylvia and Thiago for all the fun times and lively discussions we had during our coffee breaks and DDS meetings. Specially, I want to acknowledge Maria Psarrou for spending the time and effort to submit the thesis on my behalf. A special thanks to Yi for all the discussions on machine learning we had during our walks to the Forum.

I also want to thank Kathy Lee for being very helpful during the final submission process.

Most importantly, I would not have been able to complete this research without the unwavering patience, love and support of my husband, Sahir. I would also like to thank my parents for their love and support. Finally, thanks to my sister and brother-in-law for encouraging me to come to the UK and for providing me a place to live during the first few months.

Abstract

Absence epilepsy is a neurological disorder that commonly occurs in children [44]. Some studies [14] have shown that absence seizures predominantly originate either in the thalamus or the cerebral cortex. Some cerebellar nuclei (CN) neurons project to these brain areas, as explained further in Fig. 2.6 in Chapter 2. Also, some CN neurons have been observed to show modulation during the absence seizures [41]. This indicates that they somehow participate in the seizure and hence are referred to as "participating neurons" in this thesis. In this research, I demonstrate how machine learning techniques and computer simulations can be applied to investigate the properties and the input conditions present in these participating (CN) neurons. My investigation found a sub-group of CN neurons, with similar interictal spiking activity, spiking activity between the seizures, that are most likely to participate in seizures. To investigate the input conditions present in the CN neurons that produce this type of interictal activity, I used a morphologically realistic conductance based model of an excitatory CN projection neuron [66] and optimised the input parameters to this model using an Evolutionary Algorithm (EA). The results of the EA revealed that these participating CN neurons receive a synchronous and bursting input from Purkinje cells and bursting input with long intervals(approx. 500ms) from mossy fibre. The same interictal activity can also be produced when the Purkinje cell input to the CN neuron is asynchronous. The excitatory input in this case also had long interburst intervals but there is a decrease in excitatory and inhibitory synaptic weight. Surprisingly, a slight change in these input parameters can change the interictal spiking pattern to an ictal spiking pattern, the spiking pattern observed during absence seizures. I also discovered that it is possible to prevent a participating CN neuron from taking part in the seizures by blocking the Purkinje cell input.

Contents

Chapter 1

Introduction

Contents

1.1 Motivation

MAchine learning methods are used to analyse data, in this case neuroscientific data taken from in vitro or in vivo experiments, recorded using a variety of techniques. Computer simulations of mathematical models of the nervous system are used to aid in understanding and to make predictions about the operation of the nervous system at various levels of detail. In my research, I use a combination of machine learning methods and computer simulations to investigate the role of the cerebellar nuclei (CN) in absence epilepsy. In the following sub-sections, first, I give a brief overview of machine learning, computer simulations and their applications in neuroscience. Then

I detail my motivation behind the study of the CN neurons with respect to absence epilepsy.

1.1.1 Machine Learning

Machine learning algorithms are rapidly gaining popularity in many diverse fields such as robotics, pharmacy, astronomy, data mining, image processing, which contain many problems that involve analysing large amounts of data and extracting useful information from the data.

Machine learning algorithms can be divided into three main categories: unsupervised learning algorithms, supervised learning algorithms and reinforcement learning algorithms. In this research, I implement two of these methods as listed below:

- **Unsupervised Learning Algorithms:** Unsupervised learning algorithms are capable of finding naturally occurring patterns or groups in unlabelled data. The patterns are learnt entirely from the features of the data based on the similarities of the features. These algorithms are very useful in cases where information about the data is limited and we do not have the knowledge of the number of groups present in the data.

- **Supervised Learning Algorithms:** These algorithms require that the data are labelled. Each data item/input in the data has an output which may be a class label or a numeric value. Typically, a supervised learning algorithm is able to predict the class or the numeric output of unseen data based on the learning it has done on the associations or relationships between the input and the output of already available data.

In this research, I use an unsupervised learning algorithm to perform clustering in order to investigate a dataset obtained from different types of CN neurons: some of which alter their output during absence seizures and some which do not, as explained further in Section 1.1.3. Further, I use a supervised learning algorithm to perform non-linear regression on the features of the interictal activity. Interictal activity refers to the spiking activity of the CN neuron in between the absence seizures. The point of this is that it may be important to predict the likelihood of the CN neuron modulating its spiking output during absence seizures.

1.1.1.1 Application of Machine Learning Methods in Neuroscience

In the field of neuroscience, much useful information is difficult to obtain. For example, when extracellular recordings are taken from a neuron of an awake animal, the electrode picks up the spikes emitted not just by the neuron of interest but also from the neighbouring neurons. Filtering out only the desired spikes from the recording is not always an easy task. The spikes from different types of neuron can be recognised in this mix due to the fact that each type of neuron fires spikes which have a distinctive shape and may vary in amplitude when compared to the spikes from other neurons. Unsupervised and supervised machine learning algorithms can be used in this task to group the spikes into different clusters based on the features that measure or describe the shape and amplitude of the spikes.

Machine learning algorithms can also be used to classify different types of neurons based on their firing characteristics instead of the spike shape. In a recent paper, Gert Van Dijck and collaborators [19] showed that a Gaussian Process Classifier can be used to identify Purkinje Cells, Golgi cells, granule cells, mossy fibres and basket/stellate cells based on the features describing the spiking activity of the neurons. The advantage of using this method is that the models developed using the firing characteristics can be standardised and used across different laboratories. This is difficult in the previous method as the spike shape is dependent on several factors such as the type of electrode used or the geometric positioning of the electrode when recording.

Machine learning algorithms have also been used in the modeling of neurons and neurological processes by fitting parameters to experimental data. Traditionally, computational models of neurons were tuned by using methods such as hand tuning [51] or brute force [6, 22]. However, studies have shown that machine learning methods can accomplish the same task with less difficulty. For instance, Huys et al. [36] have used machine learning methods for smoothing of and parameter estimation of single cell models from noisy biophysical recordings. Montes et al. [49] have used machine learning methods to model the behaviour of synapses.

Machine learning algorithms have also found applications in EEG analysis. Some neurological diseases and conditions such as epilepsy and cerebral ischemia, which may be a result of stroke, can be diagnosed by the means of EEG analysis. The detection of specific EEG waveform patterns are key to this process and can be improved by the application of machine learning algorithms. For instance, Support Vector Machines Machine(SVMs) have been shown to be able to detect the EEG patterns which are indicative of seizures [25]. Also, SVMs, k-Nearest Neighbours (kNNs) and Deep Belief Nets (DBNs) has been used by classify and detect special EEG patterns which are indicative of abnormal brain activity [11], such as spike and sharp wave, generalised periodic epileptiform (GPED) and triphasic, periodic lateralized epileptiform discharge (PLED) and eye blinks [73].

The identification of different EEG patterns by machine learning algorithms have also led to their use in the development of brain-computer interfaces [62, 50]. Brain-computer interfaces (BCIs) decode the brain's EEG activity and generate computer commands which allow the user to control computational devices without physically touching them. To create a BCI, the EEG activities associated with different physical movements have to be learnt. To learn the EEG pattern associated with a particular physical movement, the physical movement is performed a number of times and the corresponding EEG signal is recorded. A machine learning algorithm then analyses these training samples and learns the EEG pattern associated with that particular physical movement. Once the pattern is learnt, the BCI can be used to convert intentions to actions.

1.1.2 Application of Computer Simulations in Neuroscience

Computer simulations may involve modelling a single neuron or a collection of neurons that are as realistic as possible. These computer models enable us to conduct a large variety of simulations and test hypotheses which may not be experimentally testable or may involve experiments that are difficult to conduct.

An integrate and fire model of a neuron was created by Lapique [8] as early as 1907 and this model is used widely even to this day. The biopyhsical mechanisms of how an action potential is initiated and propagated was modelled by Hodgkin and Huxley and was published as a series of 5 papers in 1952 [30, 29, 31, 32, 33]. Since then, there have been many advances in this field. Several models of neurons such as the Purkinje cell [16], cerebellar nuclei (CN) neurons [66] and so on have been developed. These neuronal models are very detailed. They are morphologically realistic, that is, the neuron models were reconstructed from the morphologies of actual neurons. The morphology of the CN neuron model was reconstructed with the help of a software package called Neurolucida (MBF Bioscience, Williston, VT USA). Also, the electrophysiological properties of the neuron were modeled using software such as GENESIS [7] or NEURON [28]. Active channels were introduced and the channel densities were distributed in the model such that the spiking output of the neuron model matched the spiking behaviour observed in actual neurons. In the Purkinje cell model, 10 different voltage dependent channels, which included a fast and persistent Na^+ channel, 3 voltage dependent K^+ channels, T-type and P-type Ca^{2+} channels and Ca^{2+} activated K^+ channels, described by Hodgkin-Huxley equations were introduced in the model. The Purkinje cell model is also able to produce the simple and complex spikes as observed in real Purkinje cells. The CN neuron model was similarly modelled to resemble an actual CN neuron in morphology and spiking behaviour. This model is described in detail in Chapter 2 section 2.4. With the help of these models, many research questions are being explored such as the mechanism of pattern recognition by Purkinje cells [65], rate and time coding of Purkinje cell pauses by the cerebellar nuclei [67, 17], to name a few.

1.1.3 Absence Epilepsy

Absence Epilepsy, or *petit mal*, is characterised by a sudden onset of brief non-convulsive seizures accompanied by an increase in muscle stiffness. The term "absence" epilepsy was coined by Calmeil in 1984 [68]. This type of epilepsy was so named because the physical symptoms that were associated with other type of eplilepsies, such as convulsions and foaming at the mouth, were absent. This type of epilepsy is also referred to as 'childhood epilepsy' since it is predominantly found in children [12] and in approximately 70% of the cases the disorder recedes as the child approaches adolescence. Though it is not considered as serious as the other convulsive types of epilepsy, people affected by this disorder experience approximately 200 or more brief (approx.10 seconds) seizures per day, which can affect their quality of life and learning.

Some studies [14] suggest that the absence seizures primarily originate either in the thalamus or the cerebral cortex. The Cerebellar Nuclei (CN) neurons, which provide the main output from the cerebellum, have upstream

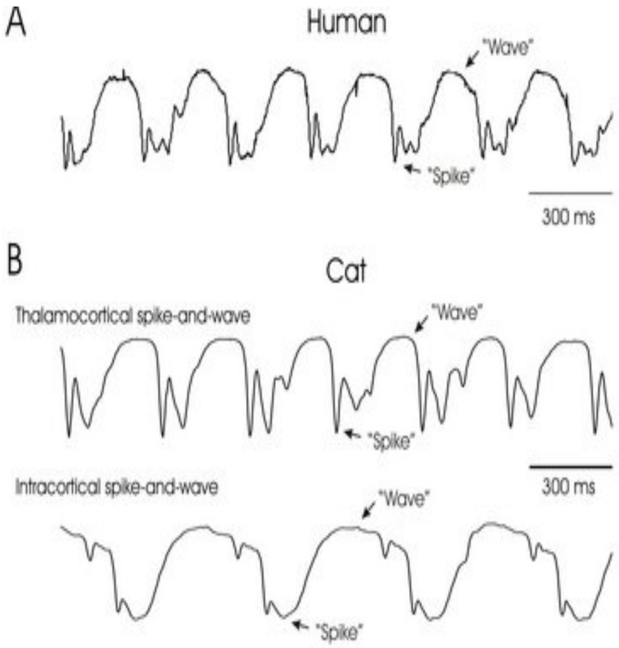

Figure 1.1: (A) shows spike-and-wave discharges (SWDs) observed during absence epilepsy in a human (B) shows the SWDs induced in a cat obtained by infusion of convulsants to cortex either in the intact thalamocortical system (top) or after removal of the thalamus (bottom). Source: [18]

connections to the thalamus and the cerebral cortex, as discussed further in Chapter 2: Section 2.3.1. However, the role of the CN neurons in absence epilepsy remains unexplored.

The absence seizures are identified by the appearance of spike-and-wave discharges (SWDs) in the electroencephalogram (EEG). A SWD is a particular type of EEG pattern which is observed during the occurrence of absence seizures. The EEG pattern may appear slightly different in different animal species as shown in the Fig. 1.2, but it typically consists of a regular, repeating pattern of a spike followed by a wave.

The SWDs observed in the tottering mice, in our experiment, were as shown in the bottom panel of Fig. 1.1 (a) and (b). The recordings in the top panels of Fig. 1.1 (a) and (b) are taken from the CN neurons of tottering mice recorded simultaneously with the EEG. Tottering mice, an established

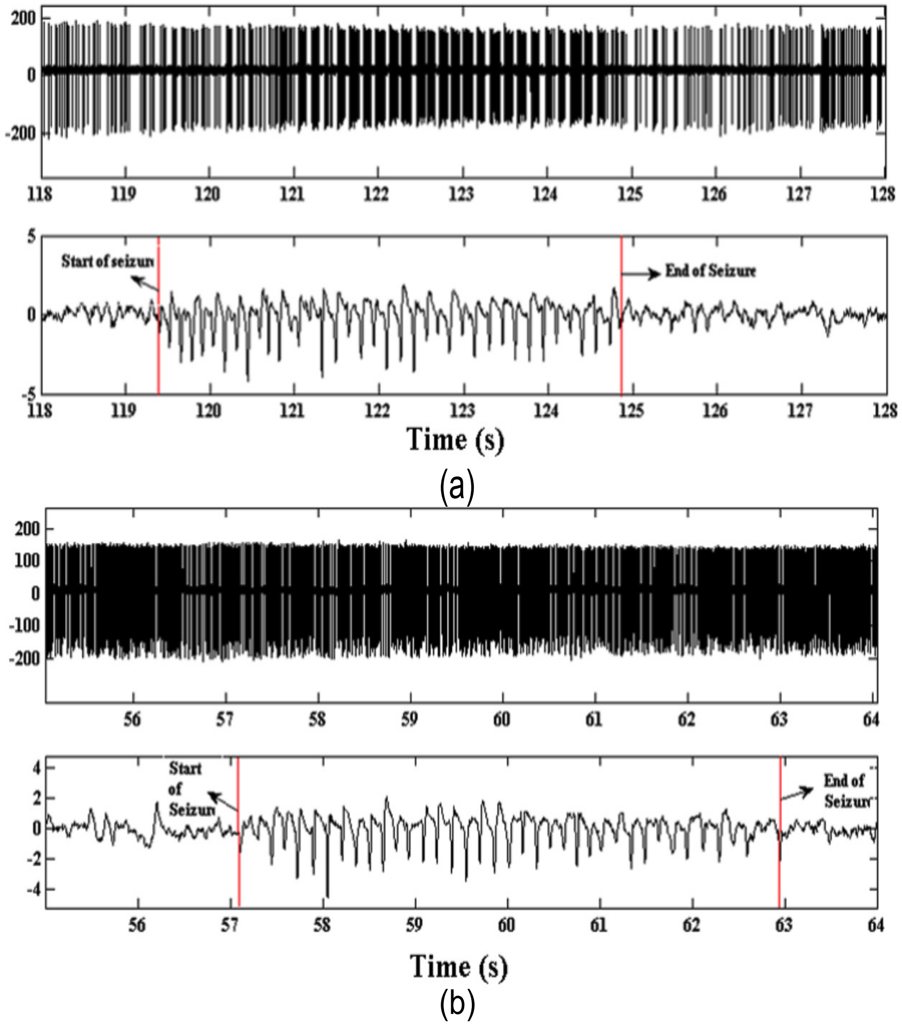

Figure 1.2: The top panels in both (a) and (b) show extracellular recordings taken from a CN neuron of a tottering mouse and the bottom panels in (a) and (b) show a simultaneous EEG recording. (a) The CN neuron's spikes show phase-locked spiking with the spikes of the SWDs in the EEG. (b) the CN neuron shows no change in its spiking behaviour and does not phase-lock its spikes with the spikes of the SWDs in the EEG.

exemplar of absence epilepsy, suffer from hundreds of absence seizures per day. They are called tottering mice as a genetic defect in these mice causes their cerebellum to dysfunction [21] which in turn affects their motor skills causing them to walk unsteadily.

Interestingly, when extracellular recordings from CN neurons from these

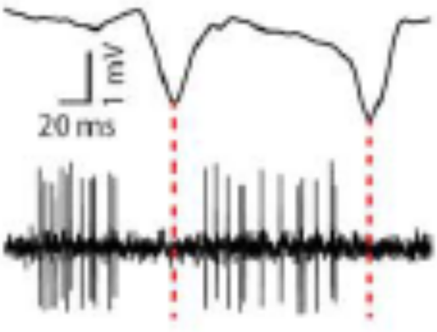

Figure 1.3: Some CN neurons in the tottering mice showed phase-locked firing with the SWDs in the EEG during absence seizures. Here, a CN neuron is shown firing during the wave portions of the SWDs and pausing during the spikes in the SWDs (shown by the red dotted lines). Source: [41]

tottering mice [41] were recorded simultaneously with the EEG, some CN neurons showed a phase-locked firing pattern with the SWDs as shown in Fig.1.1 (a) and Fig. 1.3. In Fig. 1.3, the CN neuron shows a burst of spikes during the wave part of the SWD and a pause in firing during the spike of the SWD [41]. This phase-locking with the SWDs in the EEG is sometimes slightly shifted in phase but still follows a pattern of firing and pausing as dictated by the SWDs. This shows that these neurons in some sense are participating in the seizures since their firing pattern changes. Other CN neurons do not show this behaviour during these seizures as shown in Fig. 1.1(b). I therefore refer to the former group of neurons as "participating" and the latter group as "non-participating". The measures *FFT based Z-score* and *modulation frequency*, defined in Chapter 3, quantify the phase-locking activity and decide if the CN neuron is "participating" or "non-participating". I also perform clustering in Chapter 4, to analyse the properties of CN neurons that participate in absence seizures.

1.2 Objectives

My objectives are:

- To analyse, with the help of machine learning methods, the properties of CN neurons that participate in absence seizures.
- To investigate, with the help of a CN neuron model, the input conditions leading to the spike patterns found in the CN neurons that participate in absence seizures.
- To investigate the change in input conditions that moves the CN neuron spiking pattern from an interictal spiking pattern, observed in between the absence seizures, to an ictal spiking pattern, observed during absence seizures.

1.3 Contributions to Knowledge

There has been recent interest in using machine learning to analyse neuronal data. I have shown that many interesting features of neuronal data can be found using both supervised and unsupervised data analysis techniques. Moreover, I have shown that the parameter space of model neurons can be successfully explored using evolutionary algorithms.

I have two major contributions to the knowledge: the first is the result of my investigation into how interictal spiking activity can characterise participating and non-participating CN neurons. I use a clustering method, Growing Neural Gas (GNG), that discovered properties of the type of CN neuron that is more likely to participate in absence seizures. Interestingly, these participating CN neurons were located primarily in the lateral and interpositus region of the cerebellum.The CN neurons in these regions are known to project to the thalamus and cerebral cortex, as shown in the Fig. 2.6 in Chapter 2, so changing the output of these neurons can affect the propagation of the absence seizure. Secondly, I used computerised optimisation (an Evolutionary Algorithm) to discover the most important factors in the input conditions leading to CN neuron spike patterns present during the interictal periods of the participating CN neurons.

Specifically I discovered that :

- There were five key input parameters: Purkinje cell synchronicity, inhibitory interburst interval, inhibitory burst duration, excitatory interburst interval and inhibitory synaptic weight, that affected the simulation of the spiking activity, giving an activity similar to that observed in the interictal periods of real participating CN neurons. In other words, a participating CN neuron receives a synchronous and bursting input from the Purkinje cells and a bursting input from the mossy fibre with long intervals(approx. 500ms) in between bursts during the interictal periods.

- It is possible to simulate the interictal activity of participating CN neurons when the input from the Purkinje cell is not synchronous. In this case, the input parameters: excitatory interburst interval, inhibitory synaptic weight and excitatory synaptic weight are the key parameters which affect the CN neuron's participation in absence seizures. The most interesting point to note in this experiment is that when the Purkinje cell input is asynchronous, the excitatory input to the CN neuron should be reduced (supported by the decrease in excitatory synaptic weight) to achieve the desired results.

- Instead of a dramatic change in input conditions of the participating CN neurons, a small change, that is, a change in the duration of the interburst interval of the excitatory input, is sufficient to change the output from an interictal spiking pattern to an ictal spiking pattern.

- It is possible to stop a participating CN neuron from participating in absence seizures by blocking the Purkinje cell input to the CN neuron.
- It is possible to predict the *FFT based Z-score*, a measure that quantifies the phase-locking behaviour of the CN neuron's spikes with the spikes of the SWDs in the EEG during absence seizures as explained in Chapter 3: Section 3.1, from the interictal activity of the CN neuron.

1.4 Overview of the Thesis

This section lists the upcoming chapters in this thesis and gives a brief overview of each chapter.

- **Chapter 2: Background**. This chapter gives the background on the topics such as absence epilepsy, cerebellum, CN neurons and the CN neuron model. This chapter lays the foundation needed to understand the rest of the thesis.
- **Chapter 3: Electrophysiological Data and Feature Extraction**. In this chapter, the measures used to label the CN neuron as Participating or Non-participating based on the extent of phase-locking of the CN neuron's spikes with the spikes of the SWDs in the EEG during absence seizures, are defined. Further, the various measures used to describe the interictal and ictal spiking activity of the CN neurons are explained. Also, a time series analysis of the spike-trains, using these measures, is done to visualise the different types of spiking patterns observed during and in between seizures in the CN neuron spike-trains.
- **Chapter 4: Analysis of Clustering Interictal data**. In this chapter, I use an unsupervised machine learning algorithm: Growing Neural Gas(GNG), to cluster the interictal spike-train data of the CN neuron,

in order to analyse the properties of the CN neurons that participate in absence seizures.

- **Chapter 5: Regression**. In this chapter, I use Gaussian Regression to determine if the two measures: *FFT based Z-score* and *modulation frequency* of the CN neuron can be predicted by the interictal activity of the CN neuron.

- **Chapter 6: Computer Simulations and Evolutionary Algorithm**. In this chapter, I use a CN neuron model, described in Chapter 2, to study the input conditions in the CN neuron which produce spiking activity that is similar to the interictal activity of CN neurons that are most likely to modulate their spiking activity during seizures. Since the problem involves multi-parameter optimisation, I implemented an Evolutionary Algorithm (EA) to search the input space for all possible configurations of the input conditions that can produce the desired results. I also used the EA to investigate the change in input conditions in the CN neuron model when the spiking activity changes from interictal to ictal spiking pattern. Furthermore I used the EA to study the conditions required to stop a participating CN neuron from taking part in the absence seizures.

- **Chapter 7: Conclusion**. This chapter summarises the conclusions drawn from each experiment and the contributions to knowledge provided by this research. This chapter also explores possible extensions to this research in the future. Also, a list of publications written by me during the course of my PhD is provided.

Chapter 2

Background

Contents

This chapter gives a brief overview of topics such as absence epilepsy, the cerebellum, CN neurons and gives the background needed to understand the experiments later on in the thesis.

2.1 Absence Epilepsy

Absence epilepsy is a neurological disorder commonly observed in children [44]. "Typical absence seizures are marked by brief staring spells, unresponsiveness to external stimuli and stiffness in the body" [14] . The seizures start and end abruptly and last only for a few seconds (approximately 10 seconds) with the person experiencing the seizures resuming normal activity after the seizures without knowledge of the seizure occurring. Absence seizures can be detected in the electroencephalogram (EEG) where they appear as spike-wave discharges (SWDs), which have a frequency of 2.5-4Hz in humans [13] and about 6-9Hz in mice models. An example of the spike-wave-discharges observed in the tottering mice during absence epilepsy is shown in Fig. 1.1 in Chapter 1.

The most recent classification of epileptic seizures as stated by the International League Against Epilepsy(ILAE)[5] broadly divides all epileptic seizures into either generalised or focal seizures. Generalised seizures occur and spread so rapidly that it is often difficult to identify the focal point (the origin) of the seizures and they generally engage both hemispheres of the brain. Even though the seizures, in this type of epilepsy, may appear localised, their onset location may vary. Focal seizures, on the other hand, "usually originate within networks and are limited to one hemisphere" [5]. Also, the onset region for the seizure is consistent from one seizure to another [5]. Absence seizures are classified by ILAE as generalised.

2.1.1 Etiology

Seizures can occur as a result of genetic, structural, metabolic, immune, infectious or other unknown disorders. Absence seizures have been attributed to genetic defects present in the patient. A study by Jouvenceau et al. [39] showed that the mice exemplars, see 2.1.2, which are afflicted by ataxia and absence epilepsy have mutations in the P/Q type channel in common. Further, the study found that the same mutations may also exist in humans having absence epilepsy. The mutation responsible for absence epilepsy in these patients is present in the *CACANA1A* gene. This gene is responsible for encoding the pore-forming subunit of the P/Q-type Ca^{2+} channel, which is a high-voltage-gated calcium channel that is present at synaptic terminals and responsible for the release of neurotransmitter[52].

2.1.2 Rodent Exemplars

Since the absence seizures occur mainly in children and usually recede by adulthood with limited consequences, and due to the similarities between the human and animal absence seizures, the experiments are conducted mostly on animals. The symptoms of absence epilepsy are identical in humans and the animal exemplars except for the frequency of SWDs. After several animal species were examined, it was noticed that the frequency of the SWDs was species dependent.

There are several established rodent models of absence epilepsy such as: Genetic Absence Epilepsy Rats from Strasbourg (GAERS)[71, 46], WAG/Rij rats[37] and several mice models such as tottering mice[53], leaner, lethargic and stargazer mice. Unlike the rat exemplars, the mice models also exhibit other neurological symptoms such as ataxia and lethargic behaviour apart from absence epilepsy. For my study, the tottering mice were used. The tottering mice exhibit hundreds of spontaneous seizures per day while in an awake state. The tottering mice are characterised by a loss of function of P/Q-type of calcium channels. As mentioned before, the mutation is present in the gene that encodes the Ca^{2+} channel. The P/Q-type voltage gated calcium channels are mainly distributed in the Purkinje cell terminals and possibly in the cerebellar nuclei (CN) neurons. In a study conducted by Hoebeek et al.[34], Purkinje cell terminals of tottering mice and wild type mice were observed during different stages of development. The presence of the mutation produced abnormalities in the Purkinje cells that started when the tottering mice were 3-5 weeks old and lasted through their adult life. The Purkinje cells terminals were enlarged and the number of vacuoles, whorled bodies and mitochondria were higher in number compared to the wildtype mice. Although the latency of the Purkinje cell's inhibition to the postsynaptic neurons was unaltered when compared to the wildtype mice, the output of the CN neurons, which receive the inhibitory input from Purkinje cells, was higher in frequency and irregularity.

2.1.3 Potential Foci

As mentioned in section 2.1, absence epilepsy is classified as a generalised type of epilepsy, that is, the seizures in this type of epilepsy initiate and spread so rapidly that it is difficult to pin point the area of origin (also called focus). However, recordings of different regions of the brain, in a study by Danober et al.[14] on absence seizures and other studies [27, 12], have revealed that the cortex and the thalamus play a predominant role in the development of absence seizures. Neither the thalamus nor the cortex are able to sustain the SWDs that underlie the seizures on their own. So the communication between these two regions or, in other words, the thalamo-cortical network is strongly linked to absence seizures.

The thalamo-cortical network is made up of connections between the cerebral cortex, the relay nuclei situated in the dorsal thalamus and the reticular nucleus of the ventral thalamus. It has been observed that the rhythmic oscillations that are required for the generation of SWDs are created in the thalamus [14, 12]. It has been hypothesised that the SWDs may be generated due to excessive thalamic oscillations due to hypersynchronization. In this case, the main reason for the generation of the SWDs is attributed to the thalamus. The cortex can also be the leading cause for the generation of SWDs as shown by Gloor et al. [27] when they induced generalised epilepsy in cat by the injection of pencillin. They noticed that the hyperexcitable cortical neurons, brought about by the injection of penicillin, slowly trans-

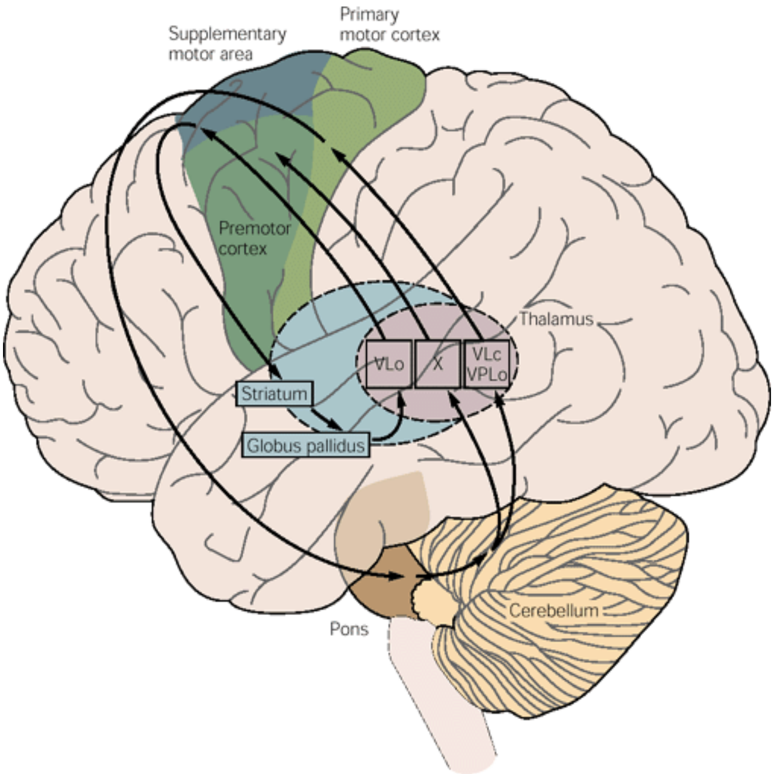

Figure 2.1: shows the location of the cerebellum and its connection to the thalamus and cerebral cortex. The output of the cerebellum projects to the thalamus. The thalamus in turn projects to the primary motor cortex and the premotor cortex areas. The cerebellum also receives input from the primary motor cortex through the Pons. Source: [40].

formed natural occurring oscillations underlying physiological processes, that occur before slow-wave sleep and during periods of quite wakefulness, in the thalamus, into SWDs.

Some studies have shown [57, 4] that direct stimulation of either the thalamus or the cerebral cortex is able to suppress the SWDs. Another possible way of controlling the generation of SWDs is by modulating the input to the thalamus and the cerebral cortex. The cerebellum, in particular the cerebellar nuclei (CN) neurons that form the main output of the cerebellum, are located in a very interesting position with respect to the thalamus and the cerebral cortex as shown in Fig. 2.1. The output of the CN neurons project to the ventral thalamus where the reticular nuclei are present and they therefore also project indirectly to the cerebral cortex; these connections are explained in detail in section 2.3.1 and also depicted in Fig.2.1. Also, there is a feedback loop from the cerebral cortex to the cerebellum through the pontine nuclei which eventually acts as input to the CN neurons. Due to the unique location of the CN neurons and our collaborator's initial observation that some CN neurons showed phase-locked spiking with spikes of the SWDs during the absence seizures, we hypothesized that the output from the CN neurons may play a role in the absence seizures and that it may be possible to control or alleviate the seizures by modulating the output of the CN neurons.

To study the role of the CN neurons in absence epilepsy, it is first important to understand the cerebellum, its organisation, the different types of CN neurons, and their connection to the thalamus and the cerebral cortex. These topics are discussed in the following sections.

2.2 Cerebellum

The cerebellum is situated at the back of the brain under the occipital and temporal lobes and forms a small separate structure as shown in Fig. 2.2.

It is densely packed with neurons (more than 50% of the neurons found in the whole brain) which are arranged in a regular, repeating pattern. The cerebellar cortex can be divided into three regions: lateral hemisphere, intermediate hemisphere and the vermis, based on the input and output projections as shown in Figure 2.3. By observing the output of these three regions, it is apparent that the cerebellum plays an important role in motor planning and execution. The cerebellum receives extensive information from the premotor cortex, motor cortex and the spinal chord and brainstem. Although the cerebellum does not initiate movement, it is thought to act as fine tuner by reconciling the differences between the plans and execution of movement.

The cerebellum is made up of three layers: the cerebellar cortex which

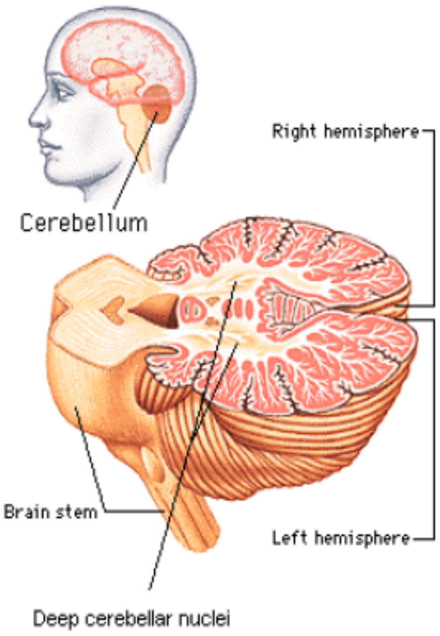

Figure 2.2: shows the location of the cerebellum. The cerebellum is located below the occipital and temporal lobes of the brain and forms a small separate structure. The enlarged figure of the horizontal cross section of the cerebellum shows the location of the cerebellar nuclei. Source:[42].

is the outer grey matter, the internal white matter and the cerebellar nuclei which are discussed further in section 2.3. The cerebellar cortex itself consists of three layers: the molecular layer, the Purkinje cell layer and the granular layer. The molecular layer forms the outermost part of the cerebellar cortex and contains two types of inhibitory interneurons, the stellate and the basket cells. The excitatory axons of the granule cells from the granular layer and Purkinje cell dendrites, whose cell bodies are located in the Purkinje cell layer, are also present in this layer as shown in Figure 2.4. The Purkinje cell layer is entirely made up of the cell bodies of Purkinje cells. The granular layer contains Golgi cells, unipolar brush cells and granule cells. The axons of the granule cells extend up to the molecular layer, split into parallel fibres as seen in Figure 2.4 and provide input to the Purkinje cell dendrites and the molecular layer interneurons. The Purkinje cell axons extend through the

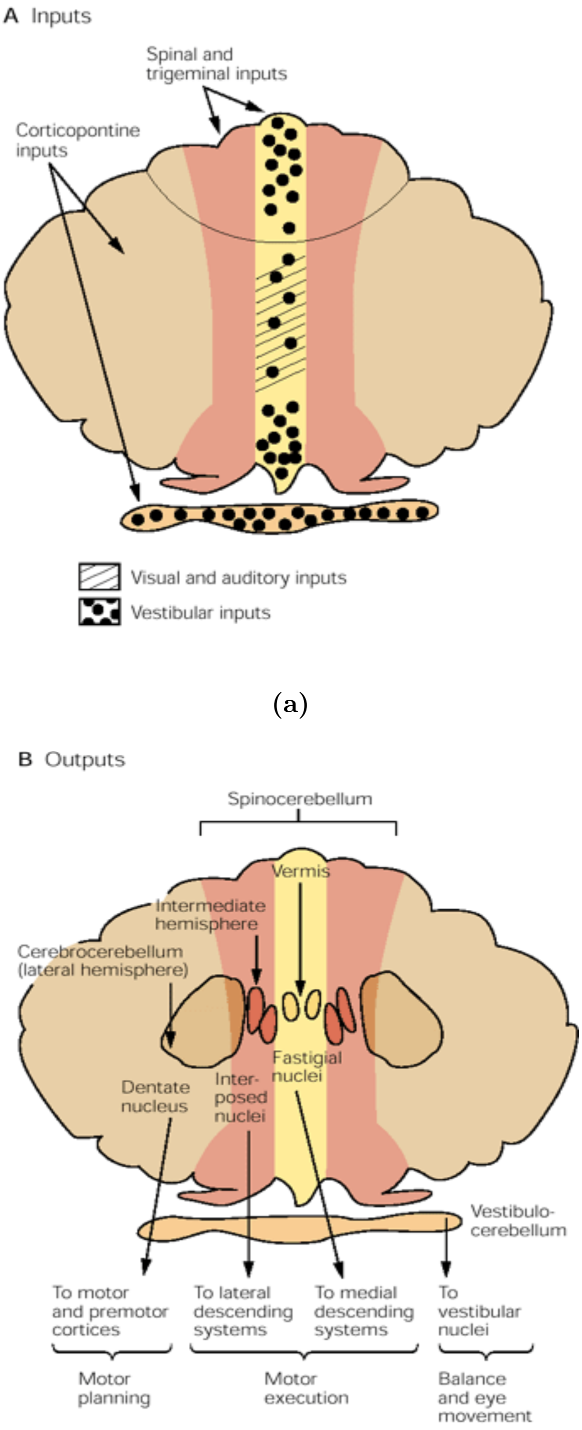

(a)

(b)

Figure 2.3: (a) & (b) show a superior (top) view of the cerebellum. They show that the cerebellum can be divided into three regions: lateral, intermediate and vermis, based on the input and the output projections to and from each region. Source: [40]

.

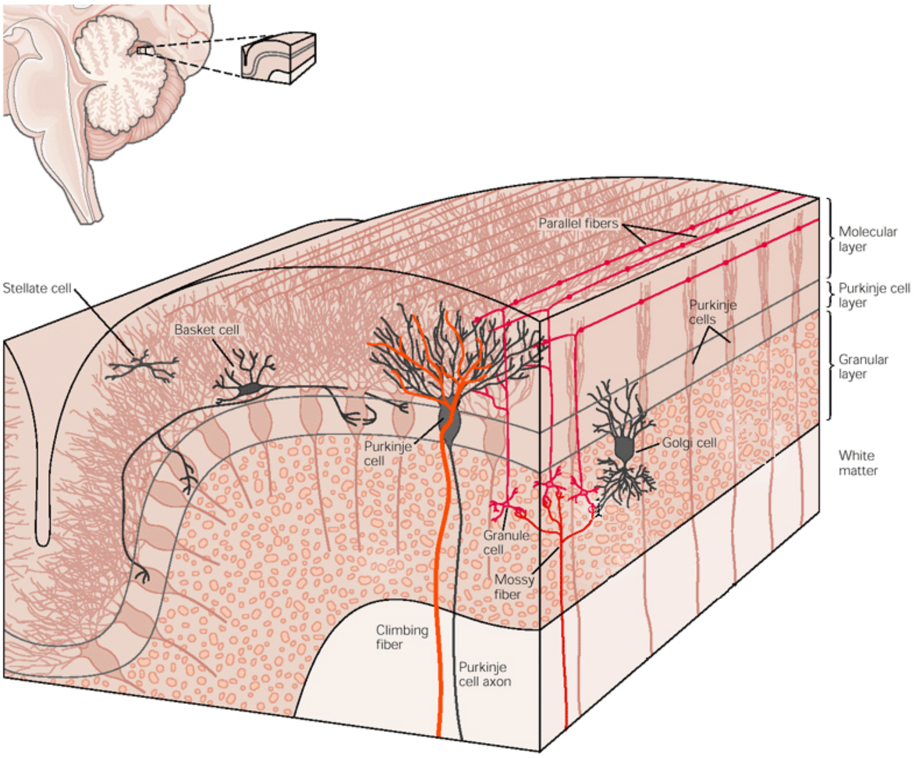

Figure 2.4: shows the three layers of the cerebellar cortex. The molecular layer contains basket and stellate cells. The Purkinje cell layer is made up of Purkinje cell somata. The granular layer contains Golgi cells and granule cells. Source: modified from [40].

white matter and provide an inhibitory input to the CN neurons. In between the Purkinje cell layer and the granular layer, spindle shaped cells, called the Lugaro cells, can be found. These Lugaro cells taper at both ends and relay information from the Purkinje cells to the cells in both the molecular layer (basket and stellate cells) and granular layer (Golgi cells).

2.3 Cerebellar Nuclei Neurons

Almost all output from the cerebellar cortex is processed by the CN neurons, with the exception of the flocculonodular lobe, a part of the cerebellar cortex whose output projects to the lateral and medial vestibular nuclei in the brain stem. Each CN neuron receives two types of input: excitatory input and

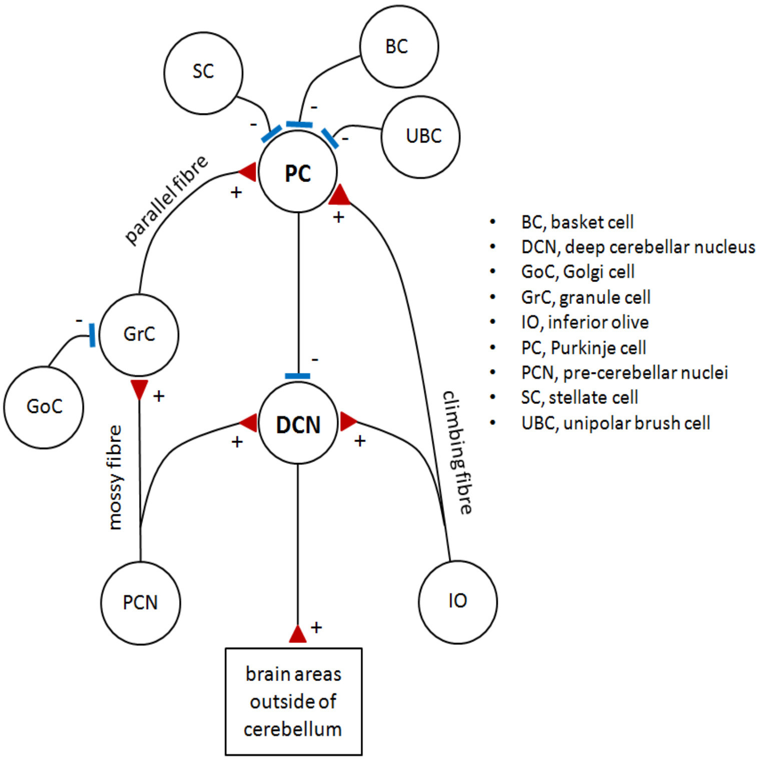

Figure 2.5: shows the different inputs to the CN neuron. The CN neuron receives excitatory inputs from the mossy fibres and climbing fibres, and inhibitory input from the Purkinje cells. The diagram also shows how the other cells in the cerebellar cortex indirectly affect the input to the CN neuron and how they are involved in the processing of information that comes into the cerebellum. Source: [42].

inhibitory input. A CN neuron receives excitatory input from the mossy fibres, which originate from the spinal cord and brain stem and provide the CN neuron with information that originates indirectly from the cerebral cortex. Moreover, there is a second excitatory input through climbing fibres from the inferior olive. The CN neuron also receives inhibitory input from the Purkinje cells. The exact number of mossy fibres and Purkinje cells converging onto a single CN neuron is not known. An early study estimated that 860 Purkinje cells converge onto a single CN neuron [56], but more recent data indicate that the Purkinje cell - CN neuron convergence ratio is closer to 50 [58]. The other neurons of the cerebellar cortex also indirectly affect the input to the CN neuron as shown in Figure 2.5.

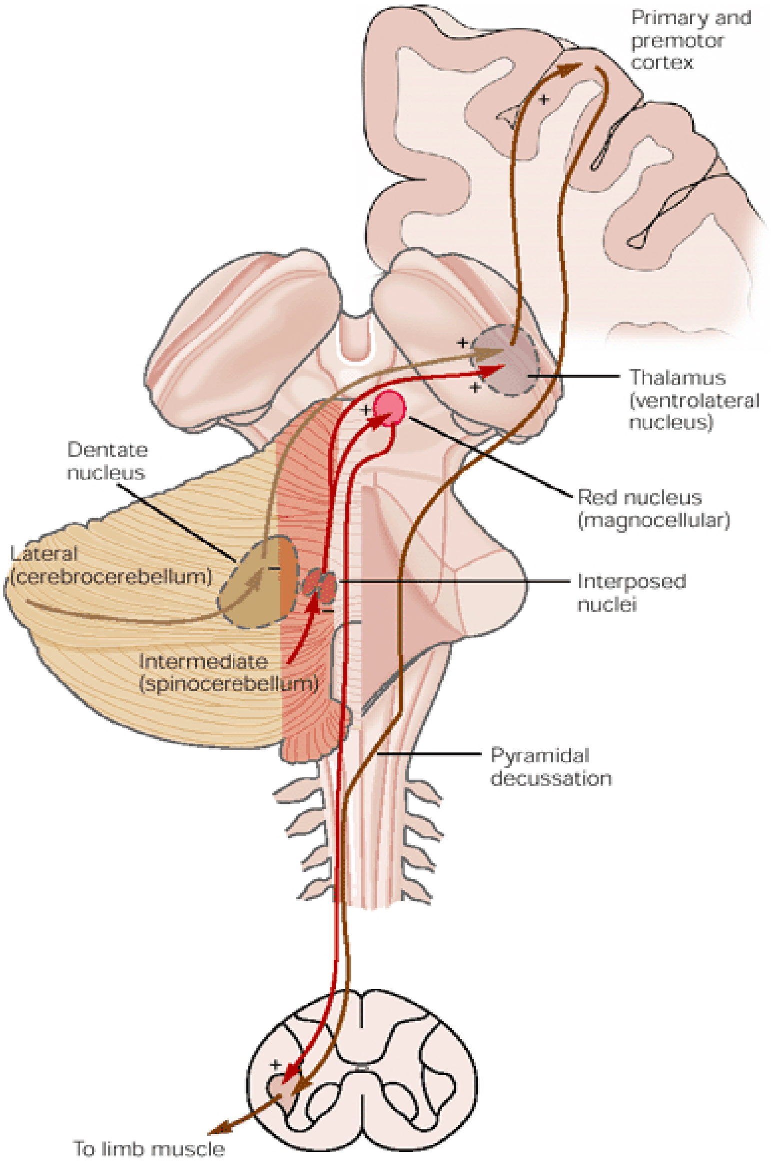

Figure 2.6: shows that the CN neurons located in different regions of the cerebellum project to different regions of the brain. The dentate nucleus present in the lateral region of the cerebellum projects to the ventrolateral nuclei in the thalamus which in turn project to the primary and premotor cortex. The CN neurons present in the intermediate region of the cerebellum project to the red nucleus and the thalamus Source:[40].

2.3.1 Types of Cerebellar Nuclei Neurons

The cerebellar nuclei neurons can be classified into different types based on different criteria. One way to classify the CN neurons is based on the their lo-

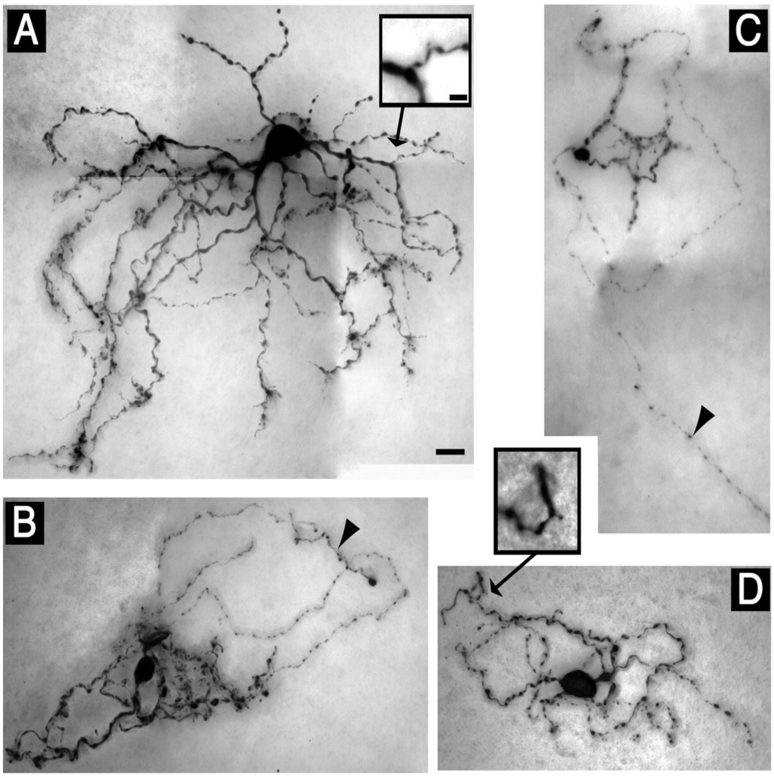

Figure 2.7: (A) & (B) show the morphology of non-GABAergic (GAD-) CN neurons. (C) & (D) show the morphology of GABAergic (GAD+) CN neurons. GAD- neurons appear larger and have more complex dendritic structure than GAD+ neurons. However, when morphometric parameters are compared, as shown in Fig. 2.8, it is clear that there is an overlap in the morphometric measures of GAD+ and GAD-. The arrowheads indicate the axon of the CN neuron and the inset shows the existence of spines on the dendrites. Source: [70].

cation in the cerebellum. As explained previously with the help of Figure 2.3, the cerebellum can be divided into three regions based on the input and output projections: lateral, intermediate and the vermis. The lateral hemisphere of the cerebellar cortex projects to the dentate nucleus, the intermediate hemisphere provides input to the interposed nucleus and the vermis projects to the fastigial nucleus. The output of the dentate nuclei projects to the neurons present in the ventrolateral nuclei in the thalamus that in turn project to the motor and premotor cortices, which are involved in motor planning as shown in Fig. 2.6. The motor planning areas, the premotor area and the supplementary motor areas, project to the primary motor cortex. Therefore, the output from the dentate nuclei is often assumed to influence the execution of fine movements. The interposed nuclei project to the red nucleus and also to the ventrolateral nuclei in the thalamus. However, in this case, the cells in the thalamus project directly to the motor cortex. Hence, the output of the interposed nuclei influences the motor system more quickly. Therefore, the output from the interposed nuclei is thought to influence the execution of quick movements. A small portion of the fastigial nuclei also project to the thalamus and the primary cortex but the majority of the output from the fastigial nuclei project to the vestibular nuclei and reticular formation, which influence posture and balance. The dentate, interposed and fastigial nuclei are terms used for CN in humans; the corresponding nuclei are called lateral, interpositus and medial CN, respectively, in mice. Henceforth in this thesis, I will be referring to the terminology for CN neurons used for mice.

In 1977, Chan-Palay [9] showed an alternate way to classify CN neurons based on morphological differences. Six different types of CN neurons were identified using these criteria. However, recent studies [70, 69] have suggested that the morphological differences alone are not sufficient to categorise the different types of CN neurons as even the neurons that have similar morphologies exhibit different electrophysiological and intrinsic properties.

Based on the transmitter content and the connectivity of the neurons, studies by Hillman and Fredette [10, 23] showed that the CN neurons can also be classified as excitatory projection neurons that project to the red nucleus and thalamus and have the neurotransmitter glutamate, that is, they are glutamatergic, inhibitory projection neurons that project to the inferior olive and have the neurotransmitter GABA (they are GABAergic) and CN neurons that form local circuits that are also GABAergic.

Further, a study was conducted by Uusisaari et. al [70] where glutamate decarboxylase 67-green fluorescent protein (GFP) knock-in mice were used to identify GABAergic and non-GABAergic CN neurons. The GABAergic neu-

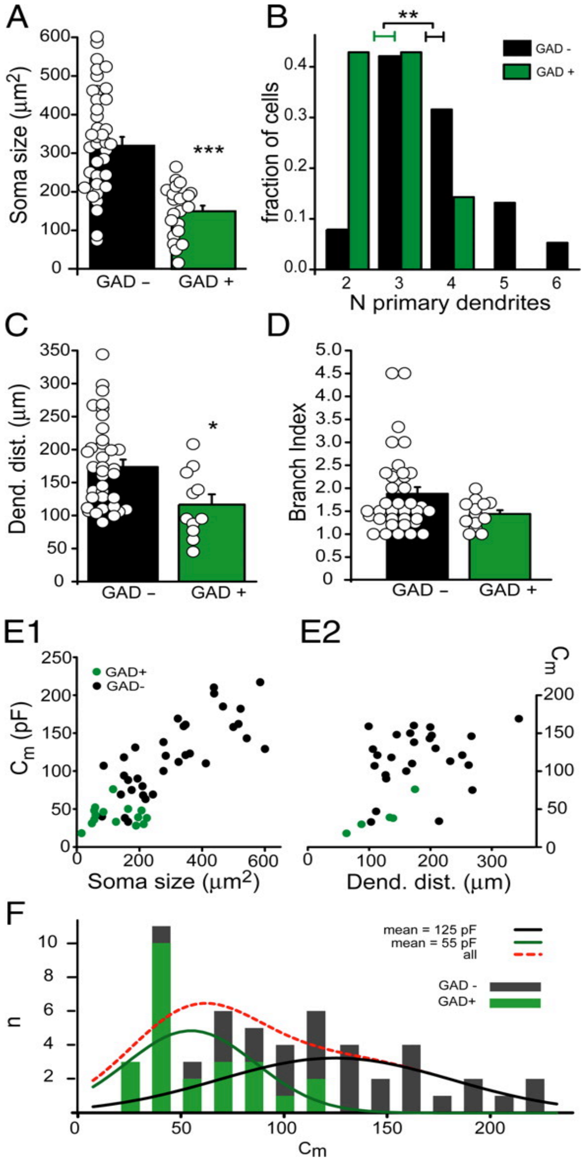

Figure 2.8: shows the comparison of morphometric measures for GAD+ (green) and GAD- (black) neurons. The circles indicate the actual individual values observed in each case. (A) shows the soma size of GAD+ and GAD- neurons. (B) shows the distribution of primary dendrites. The mean and Standard Error are shown by the horizontal bars (C) & (D) show the number of dendrites and branches crossing the $30\mu m$ circle around the soma centre. (E1) & (E2) show the membrane capacitance C_m for each neuron plotted against soma size and dendritic distance respectively. Larger neurons have a larger value of C_m. (F) shows the Gaussian distribution of the C_m value for both GAD+ and GAD- CN neurons. The bin size is $15pF$. The red line shows the Gaussian distribution over both GAD+ and GAD- combined. Based on the combined Gaussian curve, only cells with a $C_m > 150pF$ can be identified as GAD- cells without any doubt. Source: [70]

rons are indicated by GAD+ and the non-GABAergic neurons by GAD- in Fig. 2.7. The morphology of the GAD- neurons is shown in Fig. 2.7(A) and (B) and that of GAD+ is shown in Fig 2.7(C) and (D). From the figures, it is clear that the GAD+ and GAD- cells exhibit a variety of dendritic morphologies. Both types were found to have local and distal connections. Even though GAD- neurons (presumed glutamatergic neurons) exhibited larger cell bodies and more complex morphologies, a more detailed study of the morphology of the GAD+ and GAD-, as shown in Fig. 2.8, revealed that the distinction between GAD+ and GAD- neurons is not that clear since there is an overlap between the GAD+ and GAD- neurons in most of the morphometric measures. The graphs in 2.8(E1)&(E2) suggest that there is a positive correlation between soma size and the membrane capacitance C_m. The graph 2.8(F) shows that it is possible to predict the type of CN neuron from C_m only if the value of $C_m > 150pF$. Therefore, morphometric parameters alone cannot determine the type of CN neuron.

A more recent publication from the same author [69] revealed further subtypes of CN neurons in the lateral cerebellar nuclei. In the previous studies, the different types of CN neurons were identified by the presence of certain proteins, called marker proteins, on the cell membrane. For instance, glutamic acid decarboxylase (GAD67) is an enzyme which produces GABA and is a marker for GABAergic neurons. Similarly, glycine transporter (GlyT2) is a marker for glycinergic neurons. In recent studies [69], transgenic mouse lines which express green fluorescent protein (GFP), a protein that causes the Aequorea Victoria jellyfish to glow, under the control of GAD67 and GlyT2 promoters are used. A promoter is a region of the DNA which promotes transcription. The GFP gene is inserted downstream of these promoters in the transgenic mice. This makes these cells glow in the presence of light enabling easy detection. Using this method,they identified 5 sub-types in the lateral cerebellar nuclei: GAD negative Large (GADnL), GAD negative Small

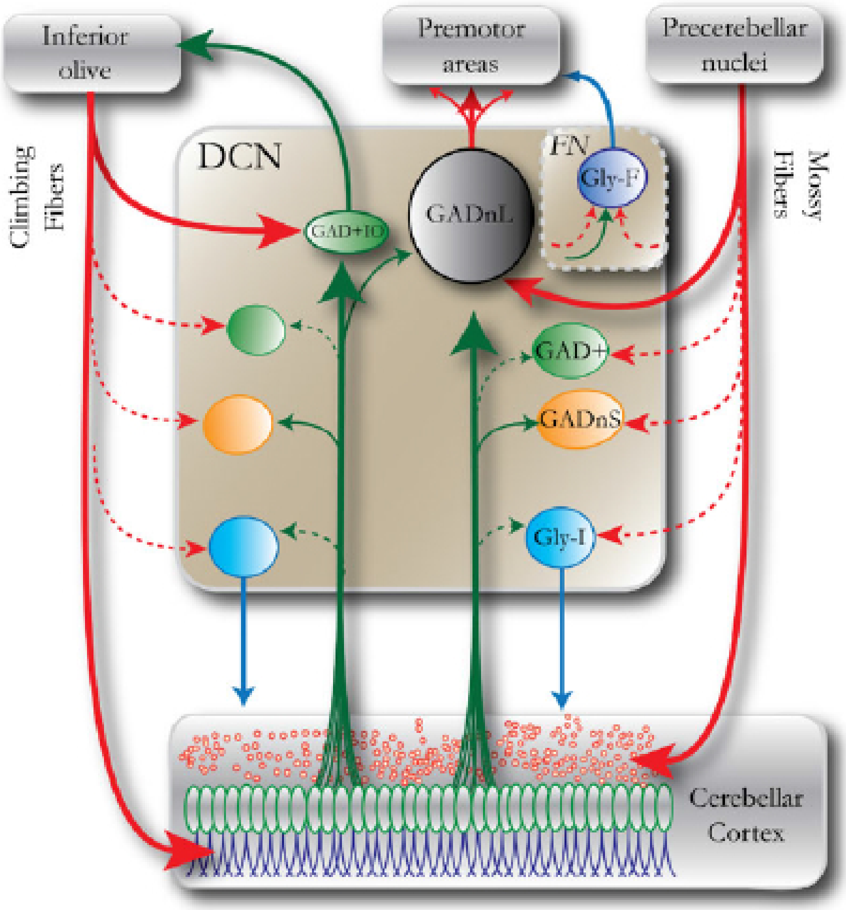

Figure 2.9: shows that there are two separate information flow loops: the olivo-cortico-nucleo-olivary (OCNO) loop shown to the left and the mossy fiber-cortico-nucleo pathway shown to the right. The red lines show excitatory connections and the green lines inhibitory connections. The GADnL neurons receive excitatory connections from the mossy fibers where as the GAD+IO receive excitatory connections from the climbing fibers originating from the inferior olive. Source:[69].

(GADnS), GAD positive (GAD+), GLY-I (Glycenergic cells), and GAD positive projecting to the inferior olive (GAD+IO). The GAD+IO neurons are similar to the GAD+ neurons but are separated out into a different type because these neurons are very small compared to the other GAD+ neurons and they project to the inferior olive. The GADnL, GADnS, GAD+ are all spontaneously firing neurons where as GLY-I and GAD+IO do not fire spontaneously. The projections and the inputs to each sub-type of CN neuron, as shown in Fig. 2.9, reveal that there are two separate information flows: the olivo-cortico-nucleo-olivary (OCNO) loop (left) and the mossy fiber-cortico-nucleo pathway. Moreover, the GLY-I neurons project to the cerebellar cortex. With this new information, again the morphometric parameters were compared. However, even with this additional information, it was still clear that the CN neurons cannot be differentiated based on morphology alone.

In our study, we do not have any information about the detailed electrophysiology or the morphology of the CN neurons from which the data were collected. Our information is limited to the recording location of the CN neuron in the cerebellum and the extracellular spike times. As explained further in chapter 4, we try to identify the type of CN neuron that is most likely to participate in absence seizures based on the interictal spiking patterns of the CN neurons alone.

2.4 CN Neuron Model

The CN neuron model used in this study is a multi-compartmental conductance-based model of an excitatory CN projection neuron. This model was implemented in NEURON by Luthman et al. [43], who translated it from its original implementation in GENESIS [66]. The morphology of the CN neuron model, as shown in Figure 2.10, was reconstructed from a biocytin stained CN neuron using Neurolucida (MicroBrightField, Inc.) as detailed in [64]. The passive parameters for the model were determined with the help of a genetic algorithm [64]. The model contains nine active conductances, which were selected based on experimental studies of CN neurons. These channels, as detailed in [66], were a fast sodium current, a mixture of fast Kv3 and slow Kv2 delayed rectifiers, which form a TEA sensitive Kdr current, a tonic non-specific cation current, a high-voltage activated (HVA) calcium current and a purely calcium-gated potassium (Sk) current. According to [66], these six

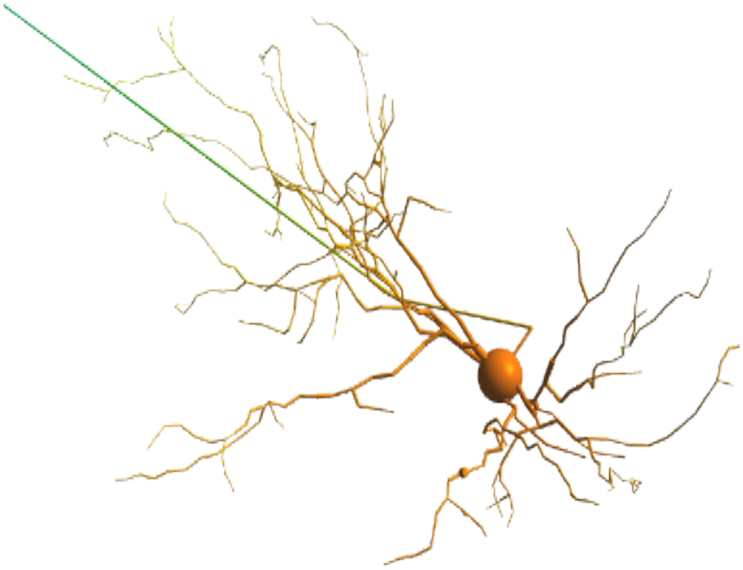

(a)

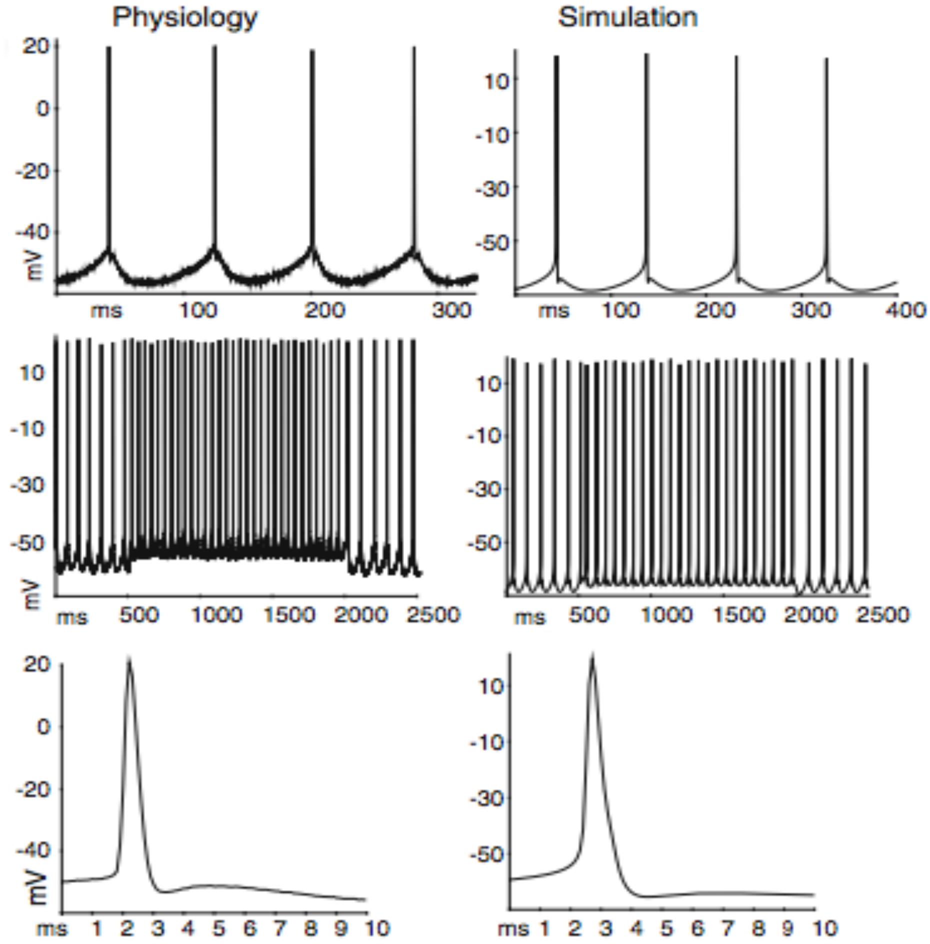

(b)

Figure 2.10: (a) A morphologically realistic, multi-compartmental conductance-based model of an excitatory CN projection neuron.(b) The left column shows the slice recording taken from a typical CN neuron. The right column shows that the simulations produced from the CN neuron model match the spike-trains in the left column with regard to spike shape and after hyperpolarization properties. [66].

conductances were sufficient to match physiological spontaneous spiking and responses to depolarizing current injection pulses. Moreover, to replicate the rebound behaviour that followed strong hyperpolarization three more channels, a hyperpolarization-activated cyclic nucleotide gated (HCN) current, a Cav3.1 low-voltage activated (LVA) calcium current and a persistent sodium (NaP) current, were added to the model [66, 43]. The intracellular calcium concentration, as detailed in [66, 43], was modelled as a sub membrane shell with calcium inflow from the HVA current and an exponential decay with a time constant of 70ms.

The CN neuron model receives excitatory input from 150 mossy fibre synapses, 50 of which were placed in the soma and the remaining were distributed into randomly chosen dendritic compartments. The model also receives inhibitory input from 450 Purkinje cell synapses. Again, 50 of these synapses were placed in the soma and the rest were distributed to randomly chosen dendritic compartments. The spike-trains originating from the Purkinje cells and the mossy fibres were generated using a modification of NEURON's NetStim object, GammaStim, as detailed in [43]. The GammaStim object provides the ability to set the irregularity of the spike-train produced. The irregularity of the inputs are controlled via noise parameters during the simulations as explained further in Chapter 6: Section 6.1.

2.5 Chapter Conclusions

Absence seizures are generalised seizures with a genetic etiology. Previous studies [14, 12] have narrowed down the focal regions of the seizures to the thalamus or the cerebral cortex. The CN neurons, which have afferent connections to both these regions, are placed in a strategic position and may provide an alternate way to control and alleviate these type of seizures.

CHAPTER 3

Electrophysiological Data and Feature Extraction

Contents

As discussed in Chapter 1 (Section 1.1.3), some CN neurons in the dataset collected by our collaborators in Rotterdam showed modulation in their spiking behaviour, that is, the CN neurons phase-locked their spikes with the spikes of the SWDs in the EEG during the occurrence of absence seizures, where as some other CN neurons did not. The dataset [41] consisted of 220 spike-train recordings taken from CN neurons of 4 to 30-week-old tottering mice of both genders.

To aid further analysis, first all of the CN neurons in the dataset had to be labelled as "Participating", if they showed phase-locked spiking with the spikes of the SWDs in the EEG during absence seizures, or "Non-participating" otherwise. To do so, our collaborators in Rotterdam introduced three measures: *Z-score of modulation amplitude*, *FFT based Z-score* and *modulation frequency*, which were used to measure the extent of phase-locking displayed by a CN neuron. The labelling revealed that more than 30% of the CN neurons in the dataset were Participating. These measures are described in the following section.

3.1 Measures to Characterise CN Neuron Participation

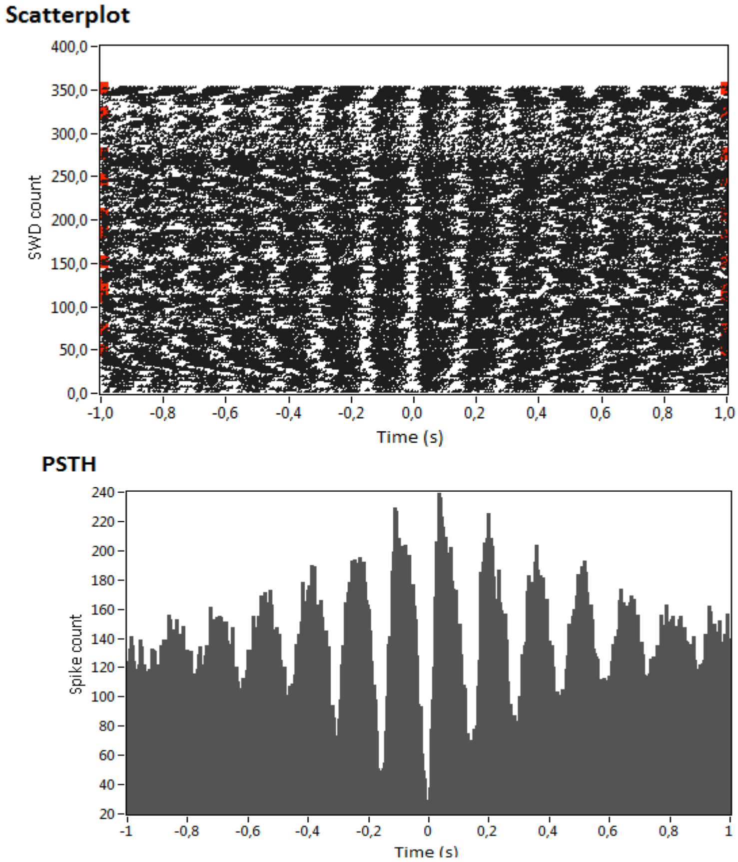

Figure 3.1: (a) shows the scatterplot created by plotting the spikes of the CN neuron with respect to the spikes in the SWDs in the EEG. Each spike in the SWD corresponds to one row in the scatterplot. The zero on the x-axis of the scatterplot indicates the time of peak of each spike of the SWD, and the spike times of the CN neuron relative to this spike are plotted on the scatter plot. The red dots along the y-axis show the different seizures observed in the spike-train. (b) shows the peri-stimulus time histogram (PSTH) created based on the scatterplot, with a bin size of 5ms.

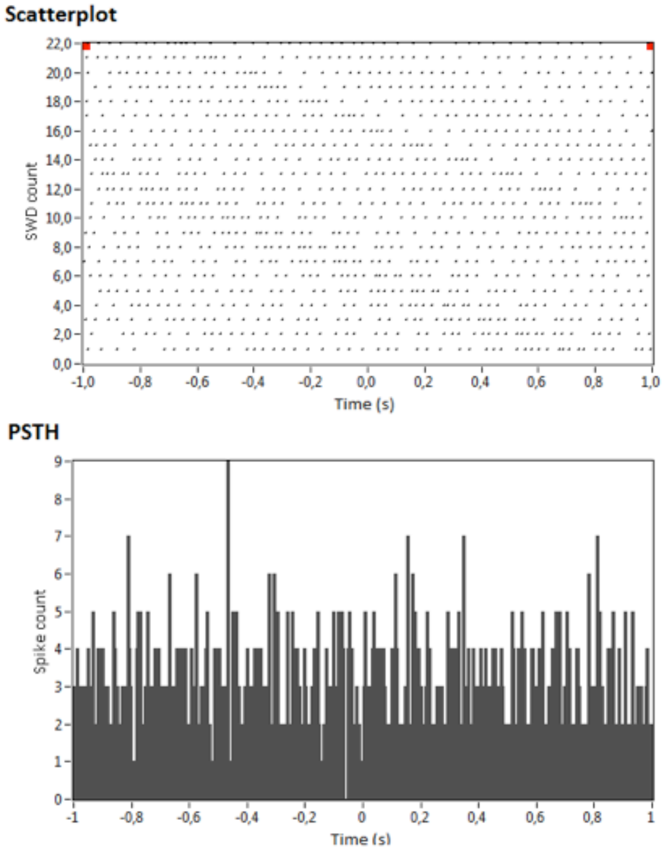

Figure 3.2: shows the activity of a CN neuron whose activity is not phase-locked with the spikes of the SWDs. (a) As in Fig. 3.1, the top panel shows the scatterplot created by plotting the spikes of the CN neuron with respect to the spikes in the SWDs in the EEG. Each spike in the SWD corresponds to one row in the scatterplot. The zero on the x-axis of the scatterplot indicates the time of peak of each spike of the SWD, and the spike times of the CN neuron relative to this spike are plotted on the scatter plot. The red dots along the y-axis show the different seizures observed in the spike-train. (b) shows the peri-stimulus time histogram (PSTH) created based on the scatterplot, with a bin size of 5ms.

First, a scatter plot was created for each spike-train that plots the occurrence of the CN neuron spikes in relation to the spikes of the SWDs, as shown in the Fig. 1.3, in the EEG during the absence seizures, as shown in the top panel of Fig. 3.1. Each seizure in the spike-train is indicated by the red dot along the y-axis. For each row in the scatter plot, the zero on the x-axis indicates the time of the peak of each SWD in the seizure. The spike-times of the CN neuron relative to this peak are plotted on either side. Then, using the scatterplot, a peri-stimulus time histogram (PSTH) is created with a bin-width of 5ms as shown in the bottom panel of Fig. 3.1. This PSTH can be used to derive the three measures: *Z-score of modulation amplitude*, *modulation frequency* and *FFT based Z-score* used to quantify the CN neuron participation in absence seizures.

The vertical distance between the peak and the trough near the time = 0 in the PSTH gives the *modulation amplitude*. When a CN neuron's activity is phase-locked with the spikes of the SWDs the peaks are sharper and the height of the peak near t = 0 is considerably higher as shown in the Fig. 3.1 than when it is not phase-locked as shown in Fig. 3.2. The *mean power* at seizure frequency(6-9Hz), which is the hallmark frequency of absence seizures in rodents, is obtained by performing a Fast Fourier Transform (FFT) on the PSTH. The peak of the power spectrum after FFT gives the dominant frequency at which the cell is modulating. A Z-score value greater than or equal to 1.96 in the SWD frequency range tells us that the cell is likely phase-locked to SWDs rather than showing a particular firing pattern by chance. The FFT gives a value (power) per frequency bin so that the mean power at seizure frequency is literally the summed value of all bins between 6 and 9 Hz divided by the number of bins.

Further, we need to assess if these two values are significant. To do so, we calculate the *Z-score* of these values. The *Z-score* is calculated by subtracting the mean from the value and dividing it by the standard deviation. The *Z-score* calculates how far the values are located from the mean. If they are within two standard deviations (<1.96) of the mean, then they could have been derived by any configuration of ISIs in the PSTH, that is, they were derived by chance. In statistics, when the mean of a population is unknown, random samples are picked to create a sample of the population and the mean of this sample is accepted as the mean. Since the mean in this case is also not known, the ISIs in the PSTH are shuffled and the modulation amplitude and mean power at seizure frequency is calculated for each iteration. If the sample size is big, then the estimated mean is closer to the actual mean of the population. Therefore, the shuffling process is repeated 500 times. The mean and standard deviation calculated from these 500 iterations are then used to calculate the *Z-score of modulation amplitude* and *FFT based Z-score.* The *modulation frequency* is determined by fitting a sine wave to the PSTH. When we construct a PSTH of CN cell action potentials triggered on the spike in a SWD it will only show peaks and troughs at SWD frequency if that cell is phase locked to the SWDs. If not modulated at all, we see a figure where all bins have approximately the same value as shown in Fig. 3.2. It is however possible that a cell bursts at for instance 3 times the seizure frequency or by chance a few pauses occurred around the spikes in SWDs. This may result in a significant Z-score of modulation amplitude even though the cell is not really modulated by SWDs. The FFT based Z-score is a stricter measure for modulation because it implies that is does not just show some modulation but it shows consistent modulation matching the frequency of the SWDs. A CN neuron was deemed to participate in the seizure if the Z-score of the *modulation amplitude* and the *FFT based Z-score* were signficantly higher than expected by chance, that is they should be greater or equal to 1.96 and the *modulation frequency* should be between 6-9 Hz. It was found that all the CN neurons which had a significant Z-score of *modulation amplitude* also had a significant *FFT based Z-score.* Therefore the two measures *FFT based Z-score* and *modulation frequency* were deemed sufficient to determine if the CN neuron participated or not.

3.2 Measures to Characterise CN Neuron Spike-trains

Once all the CN neurons in the dataset were labelled by our collaborators as participating or non-participating, I set out to find the differences between the participating and the non-participating CN neurons. To do so, I compared the spike-trains of both types of neurons during seizures (ictal activity) and in-between seizures (interictal activity). However, I found that it was very difficult to characterise the spiking activity of the CN neurons just by visual analysis. Therefore, I applied several quantitative measures to characterise the spike-trains. The measures used are listed in the following section

1. **mean_CV2 and CV :**

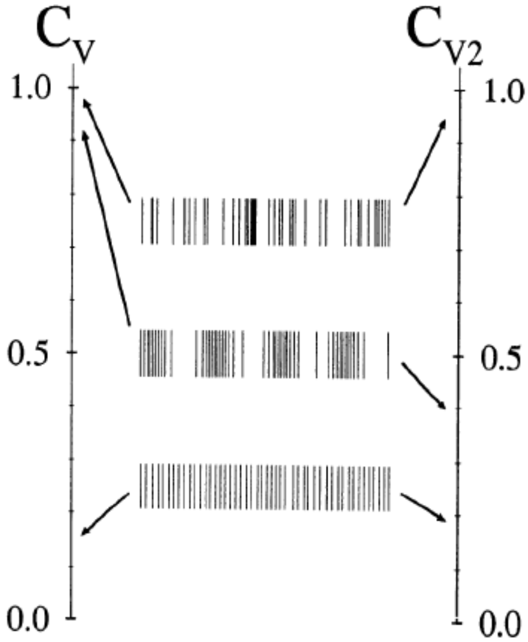

Figure 3.3: shows the value given by the measures CV and CV2 for the three spike trains. The measure CV, quantifies the top two spike trains as highly irregular and the bottom spike train as regular. The measure CV2, also quantifies the top spike train as irregular and the bottom one as regular. However, it is able to detect the local regularity of the middle spike train

These two measures are used to characterise the regularity of a spike train. The coefficient of variation (CV), calculated as shown in Eq. 3.1, captures the regularity of the entire spike train. For a Poisson process, the CV of a spike train is 1 and for a completely regular spike train, the CV is 0 as shown for the top and the bottom spike trains in the Fig. 3.3.

$$CV = \frac{std(ISIs)}{mean(ISIs)} \tag{3.1}$$

However, this measure is unable to capture the presence of local regularity in an highly irregular spike train as shown in middle spike train of Fig. 3.3. To capture this information, Holt et al. [35] introduced a new measure called CV2, also represented as C_{V2}. CV2 calculates the regularity between two consecutive ISIs only. Eq. 3.2 shows how the CV2 is calculated for the consecutive ISIs I_i and I_{i+1}. Then, as a measure of local regularity for the entire spike train, the mean CV2 for all adjacent ISIs is calculated.

$$CV2 = \frac{2|I_{i+1} - I_i|}{I_{i+1} + I_i} \tag{3.2}$$

2. **log-interval entropy:** measures the predictability of the ISIs. Log-interval entropy is calculated as shown in [19]. First, the ISIs (in ms) are expressed as their natural logarithm counterparts. Then, a histogram of the log_eISI is created with a bin width of $0.02 log_e(time)$. To lessen the effects of the arbitrary choice of bin width, a Gaussian convolution is performed. The width of the Gaussian kernel is one-sixth of the standard deviation of the ISIs. The entropy of the histogram $p(I_i)$ with N bins is calculated as:

$$Ent = \sum_{i=1}^{N} p(I_i) log_2 p(I_i) \tag{3.3}$$

3. **firing rate:** measures the frequency of CN neuron firing. This is calculated as the number of spikes divided by the duration of the observation period.

4. **permutation entropy:** The predictability of the actual value of ISIs is important and given by the log-interval entropy. Additionally, there may be information in the order in which these ISIs occur, for instance larger ISIs followed by smaller ones, and this may show the existence of some repetitive patterns in the spike-train. This is detected with the help of the measure: permutation entropy. If there exist some repeated ISI patterns in the spike-train, the permutation entropy is low, closer to zero. Permutation entropy is calculated as shown in [3].

5. **mean ISI:** This measure gives the average value of ISI observed in the spike-train.

6. **mode ISI:** A histogram of the ISIs is created with the bin centres at every 10ms. Then, the bin with the maximum number of ISIs is taken as the mode ISI.

7. **median ISI:** To get the median value of the ISI, the ISIs are sorted in an ascending order and the ISI in the middle of the list is picked. If the total number of ISIs is an even number the mean of the two ISIs in the middle of the list is considered as the median.

8. **burst index:** If two consecutive ISI's appear less than 3ms apart, they are considered to be part of a burst. The burst index is the ratio of number of burst-spikes to the number of non-burst spikes [26].

9. **pause index:** An ISI greater than or equal to 50ms indicates a pause in firing [26], and the pause index measures the ratio of the number of ISIs larger or equal to 50ms to the number of ISIs below 50ms.

10. **pause ratio:** This is similar to the pause index, however, the sum of the ISIs is considered for the calculation of the ratio [26].

11. **burst-like spike ratio:** This measure is defined as the percentage of 100ms time windows with more than 10 spikes [26]. This measure is used to describe fast spiking activity that may not necessarily be considered a burst.

    To determine the measures: mode ISI, burst index, pause index and burst-like spike ratio, some arbitrary parameters such as bin size of 10 ms for mode ISI, time window of 3 ms for burst index, 50 ms for pause index and 100 ms for burst-like spike ratio were used. These values were selected based on experimentally observed values that could separate the ictal and interictal parts of the spike-trains of participating neurons, which was necessary to conduct the experiments listed in Chapter 6, section 6.3.3 and 6.3.4.

3.3 Time Series Analysis

After selecting the measures to characterise the spiking activity of the spike-trains, I set out to conduct a cursory time-series analysis of the spike-trains. This was done in order to observe the temporal variation of the measures described in Section 3.2 during the ictal and interictal activity in participating and non-participating neurons.

The time series analysis was conducted by calculating all the measures given in section 3.2 for a 1 second wide time-window of the spike-train, then sliding the window by 0.75 seconds and calculating the same measures again for the next 1 second window. By plotting the measures for each 1 second window, a gradual change of the measures can be seen for the entire spike-train. Fig. 3.4 and Fig. 3.5 show the change of the measures, for a participating neuron and a non-participating neuron, respectively, when the time series analysis is carried out for the spike-train. In these figures, the interictal activity, spiking activity between the absence seizures (2 seconds before and after the seizure), is shown in blue and the ictal activity, spiking during the absence seizure, is shown in red.

The comparison of the two plots, Fig. 3.4 and Fig. 3.5, showed that the participating neuron had a high *CV*, high *log-interval entropy* and was more bursty when compared to the non-participating neuron. However, when all the spike-trains were analysed, the separation between participating and non-participating neurons was not as clear as initially anticipated. For example, as shown in Fig. 3.6, there were some CN neurons which showed a spiking pattern similar to the participating neurons, that is, they exhibited a high *CV* (>0.5), high *log-interval entropy* and were bursty but these CN neurons did not participate in the absence seizures. Similarly, I observed CN neurons which had a low *CV* and low burstiness but they participated in absence seizures. In order to study more systematically, whether the CN neurons can be divided into two classes: participating and non-participating, based on their electrophysiological properties, I conducted clustering on the dataset which is explained further in Chapter 4.

3.4 Chapter Conclusions

Each CN neuron in the dataset was labelled as Participating or Non-participating with the help of the measures *FFT based Z-score* and *modulation frequency.* The labelling of the data revealed than more than 30% of the neurons in the dataset were Participating. In order to characterise the spiking behaviour of the CN neurons, several measures were defined. A cursory time-series analysis of the Participating and Non-participating neurons, using these measures, showed that many participating CN neurons had a high *CV* and high

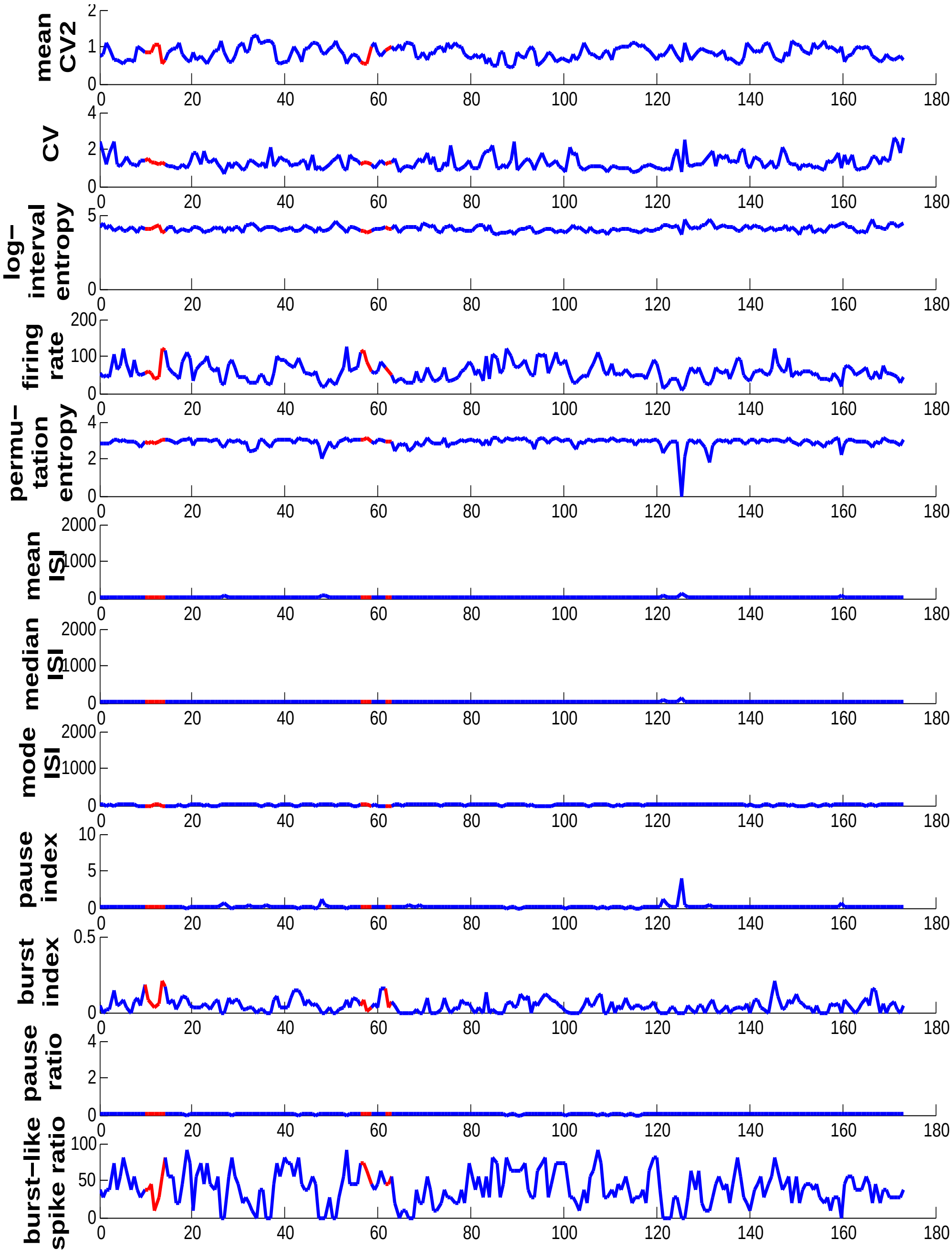

Figure 3.4: shows a time series analysis of a participating neuron. The subplots show the values of the different measures calculated over a 1 second sliding time window with a 0.25 second overlap. The red lines indicate the periods during the absence seizures and the blue lines indicate the periods in between the seizures. This spike-train shows a high *CV*, high *log-interval entropy* and high burstiness.

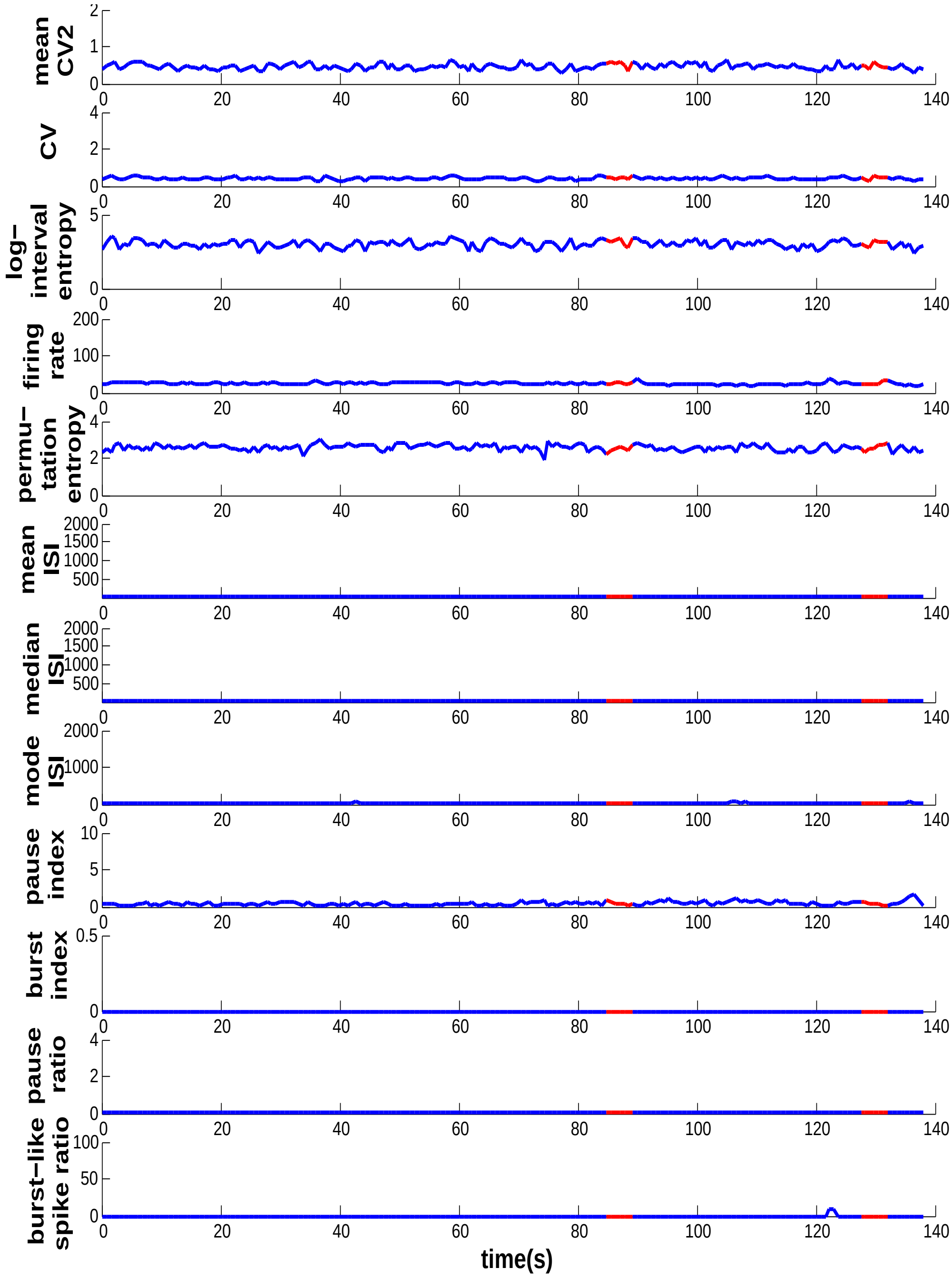

Figure 3.5: shows a time series analysis of a non-participating neuron. The subplots show the values of the different measures calculated over a 1 second sliding time window with a 0.25 second overlap. The red lines indicate the periods during the absence seizures and the blue lines indicate the periods in between the seizures. This spike-train shows a low *CV*, low *log-interval entropy* and low burstiness.

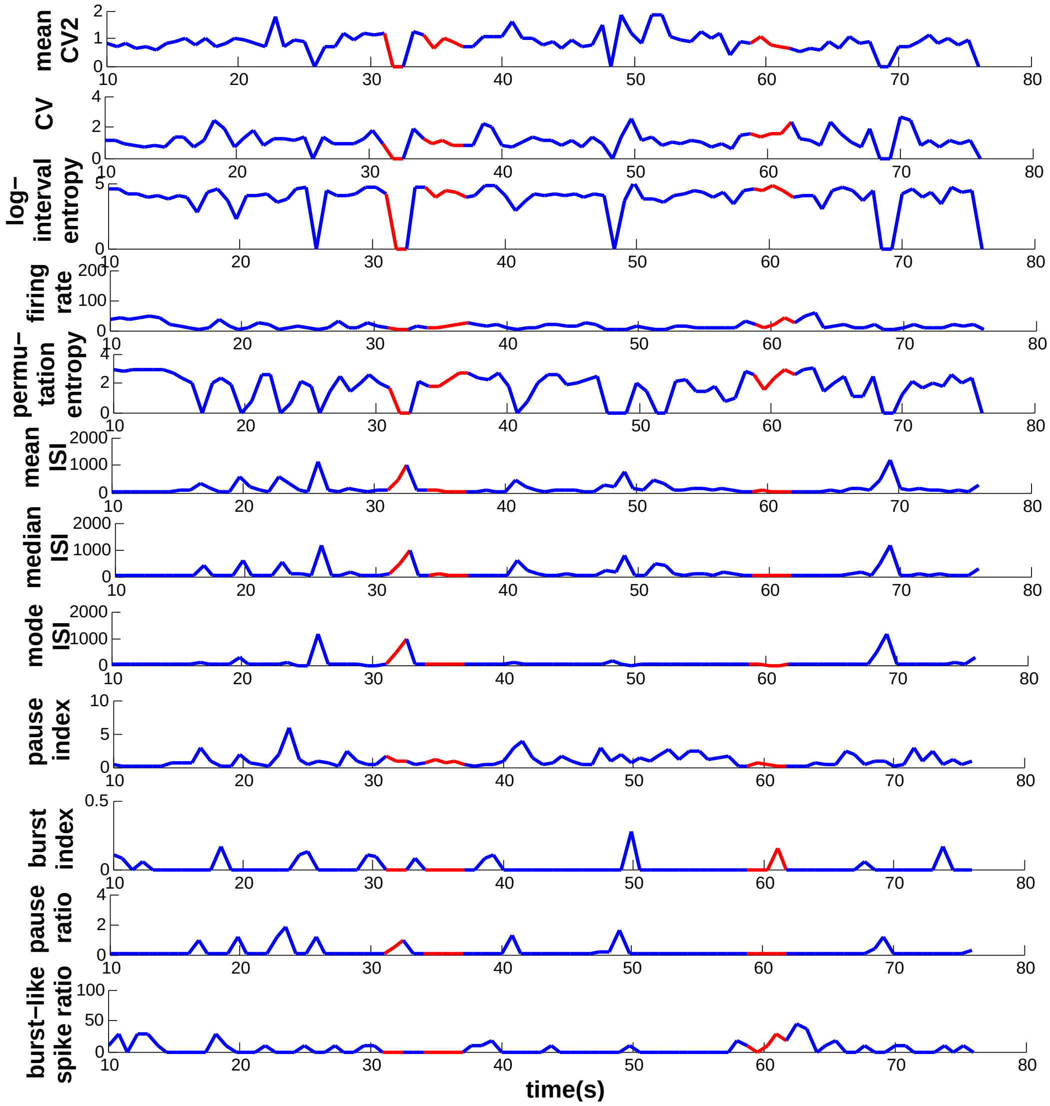

Figure 3.6: shows a time series analysis of a non-participating neuron. The subplots show the values of the different measures calculated over a 1 second sliding time window with a 0.25 second overlap. The red lines indicate the periods during the absence seizures and the blue lines indicate the periods in between the seizures. This spike-train shows a high *CV*, high *log-interval entropy* and high burstiness but the neuron was not deemed to participate in seizures.

log-interval entropy and they were more bursty, when compared to the non-participating neurons. However, I found that no measure could clearly classify the Participating and Non-participating neurons into two distinct groups.

Chapter 4

Analysis of Clustering Interictal data

Contents

In the previous chapter, the measures *FFT based Z-score* and *modulation frequency* were used to characterise the CN neurons as "Participating", if the *FFT based Z-score* $>=$1.96 and *modulation frequency* was between 6-9Hz, and "Non-participating" otherwise. The analysis revealed that the dataset had more than 30 percent of neurons which were participating. While 30 percent is a significant percentage, it also indicates that not all CN neurons alter their spiking behaviour during the absence seizures. The next step was to analyse the properties of the CN neurons which participate.

4.1 Clustering

"Clustering is the process of grouping together unlabelled data items based on similarity" [38]. Jain et al. [38] describe clustering as "an unsupervised classification of patterns (observations, data items, feature vectors) into groups (clusters)". A good clustering technique ensures that the "members of a cluster are more similar to each other than they are to members of other clusters" [74, 38].

Clustering is different from supervised learning algorithms, where each data item is associated with a label and the main aim is to label the unseen, newly encountered data based on the learning done on the labeled data. Since I also use supervised learning on my data, in Chapter 5, the supervised learning method is explained further in that chapter together with an explanation of how I applied it to my data, with the help of Gaussian Process Regression, a supervised learning algorithm.

4.1.1 Steps in Clustering:

The process of clustering typically consists of four steps [74] as depicted in Fig. 4.1:

1. **Feature selection and extraction:** The first task when it comes to clustering data, is representation of data. A proper representation of the data can improve the results of clustering considerably. A dataset

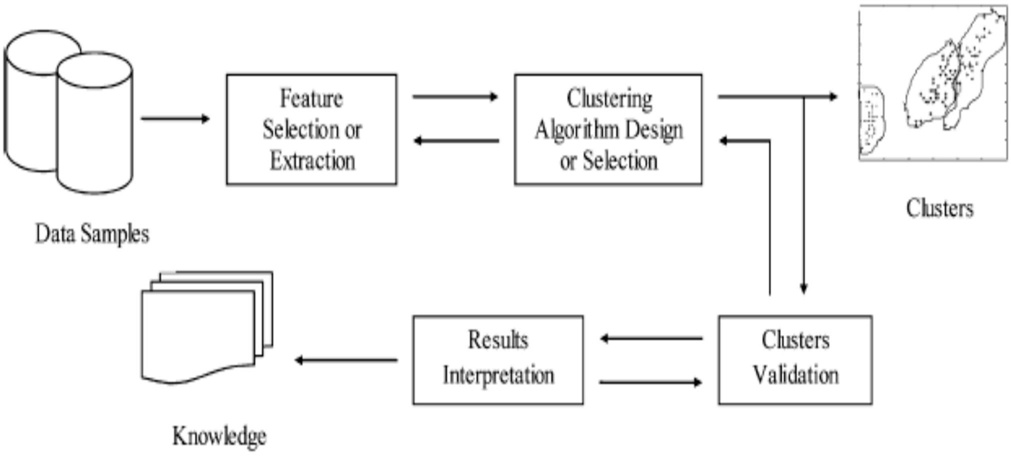

Figure 4.1: Typical steps in the clustering process. Source:[74].

is composed of a number of data items which have to be grouped into different clusters. Thus the dataset can be represented as a vector of data items that is, $\mathbf{X}$ is the dataset, $\mathbf{X} = (\mathbf{x}_1, \mathbf{x}_2, ..., \mathbf{x}_n)$, where $\mathbf{x}_i$ is a single data item. A single data item $\mathbf{x}_i$ is itself composed of several components which describe the data item. So, $\mathbf{x}_i = (x^i_1, ...x^i_d)$, where d is the dimensionality of the data space. These components are called features. Features such as *firing rate*, *mode ISI*, *burst-like spike ratio* and so on, explained in Chapter 3: Section 3.2, can either be Quantitative (continuous, discrete, interval values) or Qualitative (nominal that is unordered, ordinal). Once the data are represented by means of the features, the next step is Feature selection. "Feature selection is the process of identifying the most effective set of features for clustering" [38]. This set may be the entire set of features available or a subset. The final set of features used for clustering is typically decided by the method of trial and error as indicated by the reverse arrows in Fig. 4.1. If the existing set of features are not able to provide satisfactory results, some of the features may be transformed to give rise to new features. This process is called Feature Extraction [38].

2. **Clustering Algorithm Design or Selection:** After the publication of "Principles of taxonomy" by Sokal and Sneath in 1963 [63], the popularity of clustering algorithms increased in various fields such as image processing, pattern recognition, archaeology, biology, astrophysics, mathematics to name a few. Since the fields using the clustering algorithms are so diverse, many algorithms to cluster data have also emerged. Due to the availability of such a large number of algorithms, the process of selecting the most appropriate clustering algorithm can become a bit overwhelming for the user. Some clustering methods are more effective with a particular type of dataset than others. There are many ways to classify clustering algorithms. Jain et. al [38] have depicted one way to broadly classify the different clustering algorithms based on the approach used for clustering, as shown in Fig. 4.2. The different types of clustering algorithms shown in this figure are briefly reviewed in Section 4.2.

3. **Cluster Validation :** Due to the nature of the clustering algorithms, all clustering algorithms may find clusters which may or may not correspond with our intuitive notion of a cluster. It is therefore very important to evaluate whether the clusters produced by the clustering algorithm are actually valid. There is no definitive method in the literature to determine if the clusters produced are valid. This process is very subjective and based on the domain knowledge of the user. However, it is possible to determine by means of statistical methods that the clusters produced were not a case of chance.

4. **Result Interpretation :** The final step in clustering is result interpretation. At this point, the user analyses the clusters formed and determines if the resulting clusters contribute to knowledge about the original data. The results achieved at this stage may not be the final set of clus-

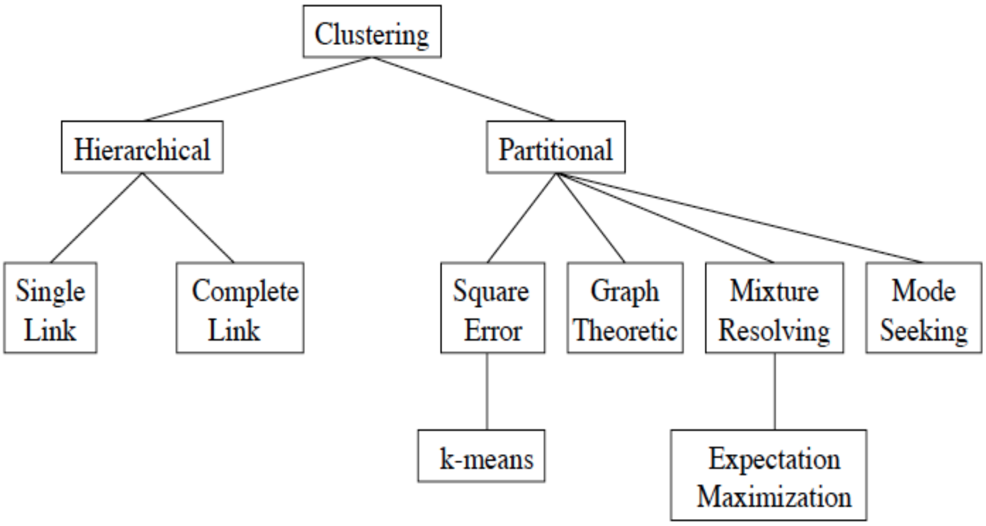

Figure 4.2: Classification of different clustering methods depending on the approach used for clustering . Source: [38].

ters but the interim results may serve to provide information about the effectiveness of feature set, proximity measures and the algorithm used for clustering.

4.2 Types of Clustering algorithms

Jain et al. classify clustering algorithms into two main categories : Hierarchical and Partitional.

4.2.1 Hierarchical Clustering

Hierarchical clustering algorithms perform clustering by grouping the data into a series of nested partitions. This nesting of the partitions is usually represented by a dendogram. Hierarchical clustering algorithms can be divisive or agglomerative. In the divisive method, all the data items are assigned to a single cluster. The clustering recursively divides this cluster into further partitions. In the agglomerative approach, each data item is initially assigned to a cluster or a partition. Then, the closest clusters are merged to form bigger clusters. The proximity of the clusters can be calculated in different ways, and this has given rise to variations in hierarchical clustering algorithms such as the single-link and the complete-link algorithms. In both algorithms, the proximity of the clusters is determined by the distance between all possible pairs of data items, one drawn from each cluster. In single-link algorithms, this proximity is determined by the minimum of all distances calculated and in complete-link, the proximity is the maximum of all the distances. In both cases, if the proximity between two clusters is below a certain distance threshold, they are merged to form a single cluster. Hierarchical clustering algorithms are advantageous in cases were the number of clusters is not known prior to clustering. The main drawback of hierarchical algorithms is that they are inefficient when large multi-dimensional datasets are considered.

4.2.2 Partitional Clustering

Partitional clustering algorithms, unlike the Hierarchical clustering algorithms, produce a single partition of the data. The partitional algorithms are more advantageous than the hierarchical algorithms when the dataset is large or where speed of execution is a criteria. However, the disadvantage of partitional clustering algorithms is that most partitional algorithms rely on the prior knowledge of the user about the number of clusters possible in the data. Also, the clustering output can change based on the initial placement of the cluster centres. The algorithms usually have to be run multiple times and the clustering output which is most meaningful to the user has to be selected.

4.2.2.1 Error Based Algorithms

The squared error clustering algorithms work by initially deciding on the number of output clusters. Then, a number of cluster centres, equal to the number of output clusters, are placed optimally in the data. Each pattern in the data is assigned to the cluster whose cluster centre is closest to the pattern. On the next iteration, new cluster centres are picked and the process is repeated. The clustering process is repeated until the clusters are stable. A popular squared error clustering algorithm method is the K-means clustering algorithm.

4.2.2.2 Graph Theoretic Algorithms

In graph theoretic clustering algorithms, a graph structure is constructed by constructing a minimal spanning tree of the data. A minimal spanning tree connects together all the vertices of the graph such that the sum of the distances between all the vertices is minimised. Then, the edges with the length exceeding a certain limit are deleted to create the clusters. Martinez and Schulten [48] introduced a graph theoretic method which was later adapted to create the Growing Neural Gas (GNG) algorithm by Fritzke [24]. These two methods are explained in detail in Section 4.3.

4.2.2.3 Mixture Resolving Algorithms

Mixture resolving algorithms are parametric methods which assume that the data to be clustered is drawn from one of the known distributions (e.g. Gaussian distribution) and the task is to find the parameters of these distributions. These methods make very strong assumptions about the data distribution, and the estimations of the parameters is not trivial. Expectation Maximization is a well-known mixture resolving algorithm.

4.2.2.4 Mode Seeking Algorithms

Mode seeking clustering algorithms, unlike the mixture resolving algorithms, are non-parametric algorithms. No prior knowledge of the number of clusters is necessary in this case. The most popular mode seeking algorithm is the mean shift clustering algorithm. The number of clusters centres are determined by identifying the locations in the data where the data is more dense. The "modes" of the data points are identified by using a kernel density estimator and by computing its gradient. Then, the data points are moved towards the "modes" to which they are closest to. The final clusters consist of the data points that converge to the same mode.

4.3 Growing Neural Gas Algorithm

Growing Neural Gas (GNG) [24] is a partitional (graph theoretic) type of clustering algorithm. As explained earlier, most partitional clustering algorithms are based on the assumption that the number of output clusters are known to the user. However, in many real world problems, very little information about the data is available. This is also the case in our data, we know that there exist different types of CN neurons but we do not have information about how many types of CN neurons are actually present in our dataset. However, GNG overcomes this disadvantage and is able to find clusters without having to know the number of output clusters beforehand. This flexibility along with speed of execution gave GNG considerable advantage over other algorithms during our clustering algorithm selection process.

4.3.1 Background

Growing Neural Gas is an algorithm based on the principles of Competitive Hebbian Learning (CHL) as given in[47] and Neural Gas (NG) [48]. In CHL, as described by Martinez [47], a fixed number of centres are first placed randomly in the high-dimensional data space, P(ξ). Then, for each data item, the two closest centres to the data item are connected by an edge. The proximity of the centres is measured using Euclidean distance. The resulting graph shows a "Delaunay triangulation" [54] with respect to the centres as shown in Fig. 4.3. Using this graph, a second graph called an "induced Delaunay triangulation" is constructed as shown in Fig.4.3. The "induced Delaunay Triangulation" graph is basically obtained by retaining only the edges whose common *Voronoi* edges lie (at least partially) in an area where P(ξ)>0.

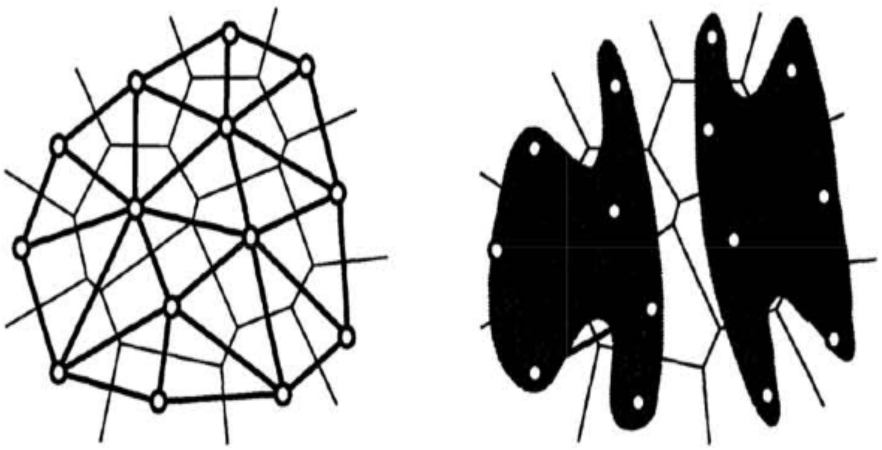

(a) **(b)**

Figure 4.3: (a) shows the "Delaunay Triangulation" (thick lines) produced by creating an edge between the points who have adjacent *Voronoi polygons* (thin lines) (b) the "induced Delaunay Triangulation"(shaded area) is produced by retaining only the edges whose common *Voronoi* edges lie (at least partially) in an area where P(ξ)>0. Source: [24].

However, the results of CHL are influenced by the placement of the centres. Only the centres which are close to some inputs are connected by edges, the rest are not used. These centres are called "dead units". To make the placement of the centres more efficient, Martinetz and Schulten developed the NG algorithm. The NG algorithm uses an adaptation parameter, k which has an adaptation strength of s. Initially k is set to a high value. For every input signal, $\mathbf{x}$, k nearest centres are moved towards $\mathbf{x}$ by a value of s. After every iteration, the adaptation parameter k and s are decreased so that finally only the nearest centre to $\mathbf{x}$ is moved by a small amount s. After the application of NG algorithm, to effectively place the centres, the CHL algorithm can now be executed to produce the "induced Delaunay Triangulation". Martinetz and Schulten also showed that it is possible to combine the two algorithms to run concurrently. However, this produced the problem of edges which were invalidated because of the movement of centres. To remove these edges, Martinetz and Schulten introduced *edge aging*, whereby obsolete edges were deleted. Although the combination of CHL and NG was an effective way to find clusters in the data, some problems existed in the practical implementation. The number of centres and the number of adaptation steps for the NG algorithm had to be determined beforehand. If the parameters used did not produce the expected result, repeated runs with different values for the parameters were necessary. Bernd Fritzke showed that his algorithm, GNG [24], could eliminate these problems. The GNG algorithm is explained in detail in Algorithm 2 in Appendix A. GNG follows the same basic principles of CHL and NG. The nodes are placed in the input space where $P(\xi)>0$. The joining of the nodes via edges creates the "Delaunay Triangulation" as in CHL. The concept of *edge aging* gets rid of obsolete edges as the algorithm progresses. GNG implements "soft competition" that is when a node wins, not only the winning node is moved closer to the data point but also its neighbours are moved closer to the data point although to a slightly lesser degree. Resetting the edge age to zero every time a node wins ensures that the edges closest to the input data points do not age much and hence are not deleted. The local *error* variable for each node indicates where there is a need to insert a new node. All the nodes which do not have edges emanating from them are removed after every iteration, thus ensuring that there are no "dead units".

4.3.2 Implementation

As mentioned before, there are typically four steps in the clustering process. The following sub-sections detail how each step was applied to our dataset.

4.3.2.1 Feature Selection and Extraction

The first step of clustering is the representation of the dataset, feature selection and extraction. The data that was available to me originally was in the form of a vector for each CN neuron, indicating the spike times of the CN neuron from which it was recorded. I also had the EEG that was recorded simultaneously and the start and stop times of the absence seizures. This vector could not be used directly for clustering. So I had to extract features which describe the spike-time vectors more effectively. As detailed in the previous chapter these features were *mean_ CV2*, *CV*, *log CV*, *log-interval entropy*, *permutation entropy*, *firing rate*, *mode ISI*, *mean ISI*, *median ISI*, *min ISI*, *burst index*, *burst-like spike ratio*, *pause index*, *pause ratio*. The spike trains were initially divided into ictal and interictal parts depending on the times when the corresponding EEG showed spike-wave-discharges of 6-9Hz. Then the previously mentioned features were calculated separately for the ictal and interictal parts of each spike train. Then, I used only the interictal features for clustering. After clustering, I labeled the neurons as participating or non-participating. The purpose of using only the interictal features, the features which show the actual spiking nature of the neuron when not affected by seizure activity, is to see if different groups of CN neuron are present in the data and if after labelling, some pure clusters emerge. If some purely participating clusters emerge, that will indicate that the CN neurons with certain interictal spiking properties are more likely to modulate their output during absence seizures.

A strong negative or positive correlation between the features used for clustering can affect the distance measures and hence clustering [38]. Therefore, a correlation matrix was constructed between the features of interictal parts of the spike-trains as shown in Table 4.1. Only subsets of the feature set consisting of not strongly correlated parameters were considered for clustering.

	mean_CV2	***CV***	*log CV*	*log-interval entropy*	*firing rate*	*permutation entropy*	*mean ISI*	***mode ISI***	*median ISI*	*min ISI*	*pause index*	*burst index*	*pause-ratio*	***burst-like spike ratio***
mean_ CV2	1.0	0.7	-0.9	0.8	-0.2	-0.2	0.1	0.0	-0.2	-0.4	-0.1	0.2	-0.1	0.0
CV	0.7	1.0	-0.6	0.8	0.1	0.0	-0.1	**-0.3**	-0.5	-0.5	-0.2	0.3	-0.2	**0.2**
log CV	-0.9	-0.6	1.0	-0.6	0.5	0.6	-0.6	-0.4	-0.1	0.0	-0.3	0.0	-0.2	0.2
log-interval entropy	0.8	0.8	-0.6	1.0	0.1	0.1	-0.2	-0.3	-0.5	-0.6	-0.3	0.2	-0.3	0.2
firing rate	-0.2	0.1	0.5	0.1	1.0	0.8	-0.8	-0.7	-0.7	-0.6	-0.5	0.4	-0.3	0.8
permutation entropy	-0.2	0.0	0.6	0.1	0.8	1.0	-1.0	-0.9	-0.8	-0.7	-0.8	0.2	-0.6	0.5
mean ISI	0.1	-0.1	-0.6	-0.2	-0.8	-1.0	1.0	1.0	0.8	0.8	0.8	-0.2	0.7	-0.5
median ISI	0.0	-0.3	-0.4	-0.3	-0.7	-0.9	1.0	1.0	0.9	0.9	0.9	-0.2	0.7	-0.5
mode ISI	-0.2	**-0.5**	-0.1	-0.5	-0.7	-0.8	0.8	0.9	1.0	0.9	0.8	-0.2	0.7	**-0.4**
min ISI	-0.4	-0.5	0.0	-0.6	-0.6	-0.7	0.8	0.9	0.9	1.0	0.9	-0.2	0.8	-0.4
pause index	-0.1	-0.2	-0.3	-0.3	-0.5	-0.8	0.8	0.9	0.8	0.9	1.0	-0.1	0.9	-0.2
burst index	0.2	0.3	0.0	0.2	0.4	0.2	-0.2	-0.2	-0.2	-0.2	-0.1	1.0	-0.1	0.5
pause ratio	-0.1	-0.2	-0.2	-0.3	-0.3	-0.6	0.7	0.7	0.7	0.8	0.9	-0.1	1.0	-0.1
burst-like spike ratio	0.0	**0.2**	0.2	0.2	0.8	0.5	-0.5	**-0.5**	-0.4	-0.4	-0.2	0.5	-0.1	1.0

Table 4.1: shows the correlation matrix between all the features of the interictal parts of the spike trains.The features used for clustering should not have a strong positive correlation(>0.7) or a strong negative correlation (<-0.7) as this can affect the proximity measures in the clustering algorithm [38]. Therefore, subsets of features considered for clustering were made of features that are not strongly correlated to each other. The highlighted cells in the table show that the features *mode ISI*, *burst-like spike ratio* and *CV*, which are the features used for our final results, are not strongly correlated.

If the original values of the features are used directly for GNG clustering, the features which have a larger range will minimise the effect of the features with smaller ranges. Therefore, before clustering, the feature vectors have to be normalised by taking a Z-score of the original values, that is the mean of the feature is subtracted from the data item value and this is divided by the standard deviation of the feature. This ensures that undue importance is not given to larger range features during clustering.

4.3.3 GNG Clustering Results and Cluster Validation

A number of subsets consisting of different combinations of not strongly correlated features were used to perform GNG clustering. The GNG algorithm produced a large number of clusters (approximately 60), which was not very easy to analyse. To simplify the analysis of the clusters, I applied hierarchical agglomerative clustering to the existing clusters, where the clusters whose centres were less than a certain threshold value apart were joined together into a single cluster. The joining process was stopped when further joining of the clusters resulted in more impure clusters, that is clusters having a mix of participating and non-participating neurons. To determine the purity of the clusters I designed a cluster purity algorithm which is detailed in Algorithm 1. After the implementation of this algorithm, I discovered that the concept of cluster purity and algorithms to calculate it already existed [45]. The threshold value was increased in increments of 0.1 and the resulting cluster purity was plotted against the threshold value as shown in Fig.4.4(b). Even though a high cluster purity is desired, we cannot pick a threshold value solely on this criterion. We have to select a threshold value which gives us a manageable number of clusters without affecting the cluster purity to a large extent. The dotted line in Fig.4.4(b) shows the threshold value (1.1) which we used for the final results. This value was selected because at this point the number of clusters is manageable and as seen in Fig.4.4(b), a further increase in threshold value reduces the cluster purity considerably.

From the set of features, the final set of features I used for our clustering were *CV*, *mode ISI* and *burst-like spike ratio*. The final clustering result is shown in Fig.4.4(a). This set of features was selected because this combination of features proved to be the most effective in separating the "participating"and "non-participating" neurons into different clusters.

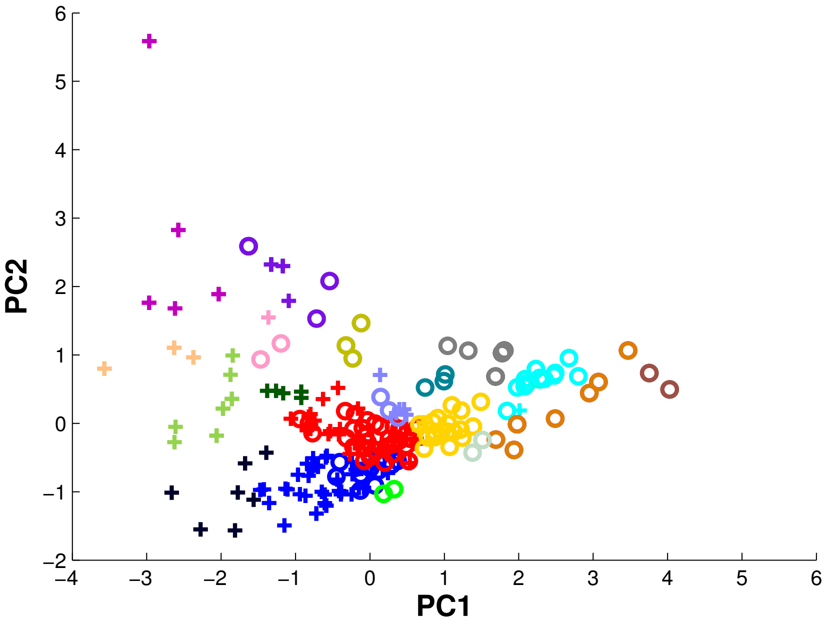

(a)

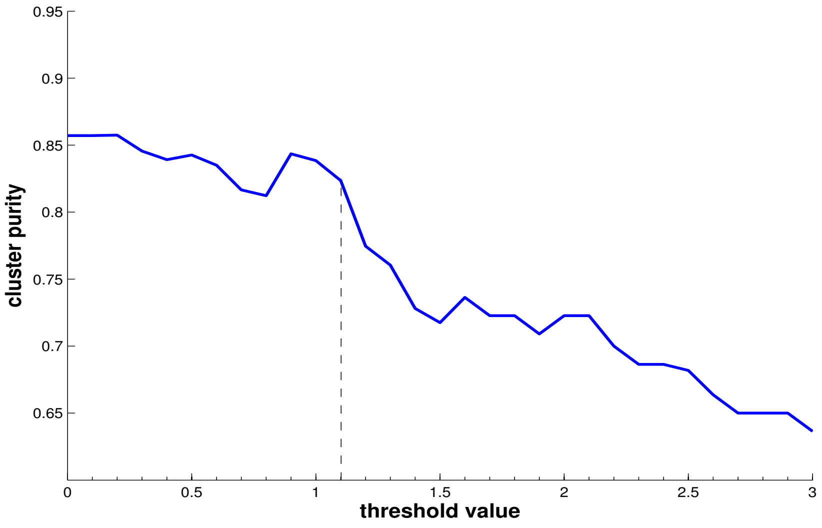

(b)

Figure 4.4: (a)shows GNG clustering of the CN neuron activity using *CV*, *mode ISI*, *burst-like spike ratio*. The results are shown in a 2D projection using PCA. The crosses (+) indicate cells that have a significant *FFT based Z-score* and a *modulation frequency* between 6-9Hz. The circles (o) represent cells that do not have a significant *FFT based Z-score* or their *modulation frequency* does not lie between 6-9Hz. (b) shows the cluster purity for each threshold value. The cluster purity value indicates the amount of mixing of the two classes of neurons, participating indicated by (+) in (a) and non-participating indicated by (o) in (a), that is present in the clusters. A high cluster purity value indicates that the clusters are predominantly made up of the same class of neurons. The dotted line indicates the value selected for the final clustering result.

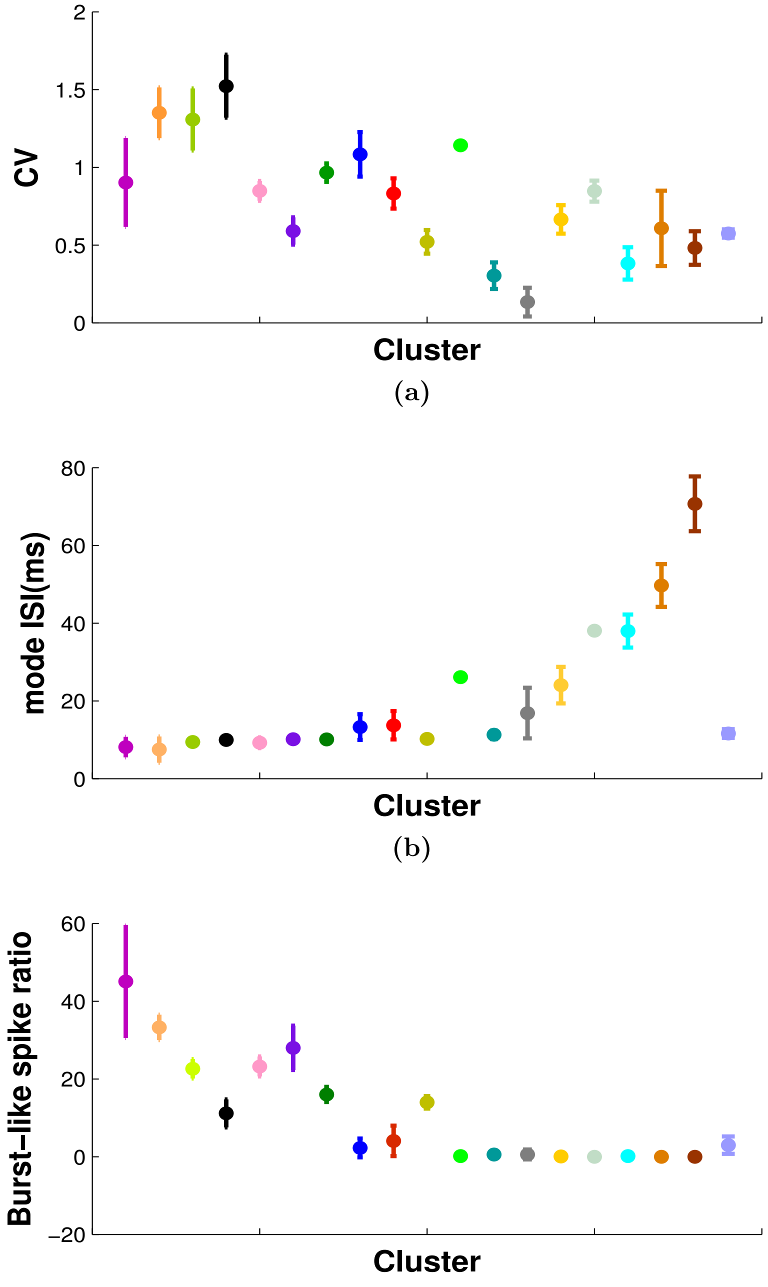

(a)

(b)

(c)

Figure 4.5: shows the mean and standard deviation of each measure - *CV*, *mode ISI*, *burst-like spike ratio* for each cluster. The clusters are colour-coded as in Fig. 4.4.

1. In the dataset, identify the number of clusters present.
2. For each cluster, the maximum number of data items belonging to the same class gives the *purity index* of the cluster.
   $purity\,index = max(num_{class1}, num_{class2}, ..., num_{classn})$
3. A *weighted purity index* for a cluster is calculated by multiplying the *purity index* by the *cluster size*.
4. Calculate the *weighted purity index* for all the clusters. The sum of all *weighted purity indices* is equal to the *weighted average*.
5. $cluster\,purity = weighted\,average/total\,cluster\,size$.

Algorithm 1: Cluster Purity

4.3.4 Visualisation of GNG Results

The original GNG algorithm gives as output a set of nodes, and the information about which nodes are connected by edges. As the number of data points is large, the graph that was produced using this information was not easy to analyse. Also, it was difficult to ascertain which data points belonged to the same cluster. To facilitate this, the GNG algorithm was modified to output the winner node information for each datapoint. After that, I designed a custom MATLAB routine to determine which data points belonged to the same cluster and coloured each cluster in a different colour. Then a 2D projection of the results, using Principal Component Analysis (PCA), was done to visualise the results. The 2D projection using PCA was particularly helpful in visualising the results when the number of dimensions was greater than 2, that is, when more than 2 features were considered for clustering. The "participating" neurons are indicated by crosses (+) and the non-participating neurons are indicated by circles (o) in Fig.4.4(a). The different colours in the Fig.4.4(a) indicate the different clusters.

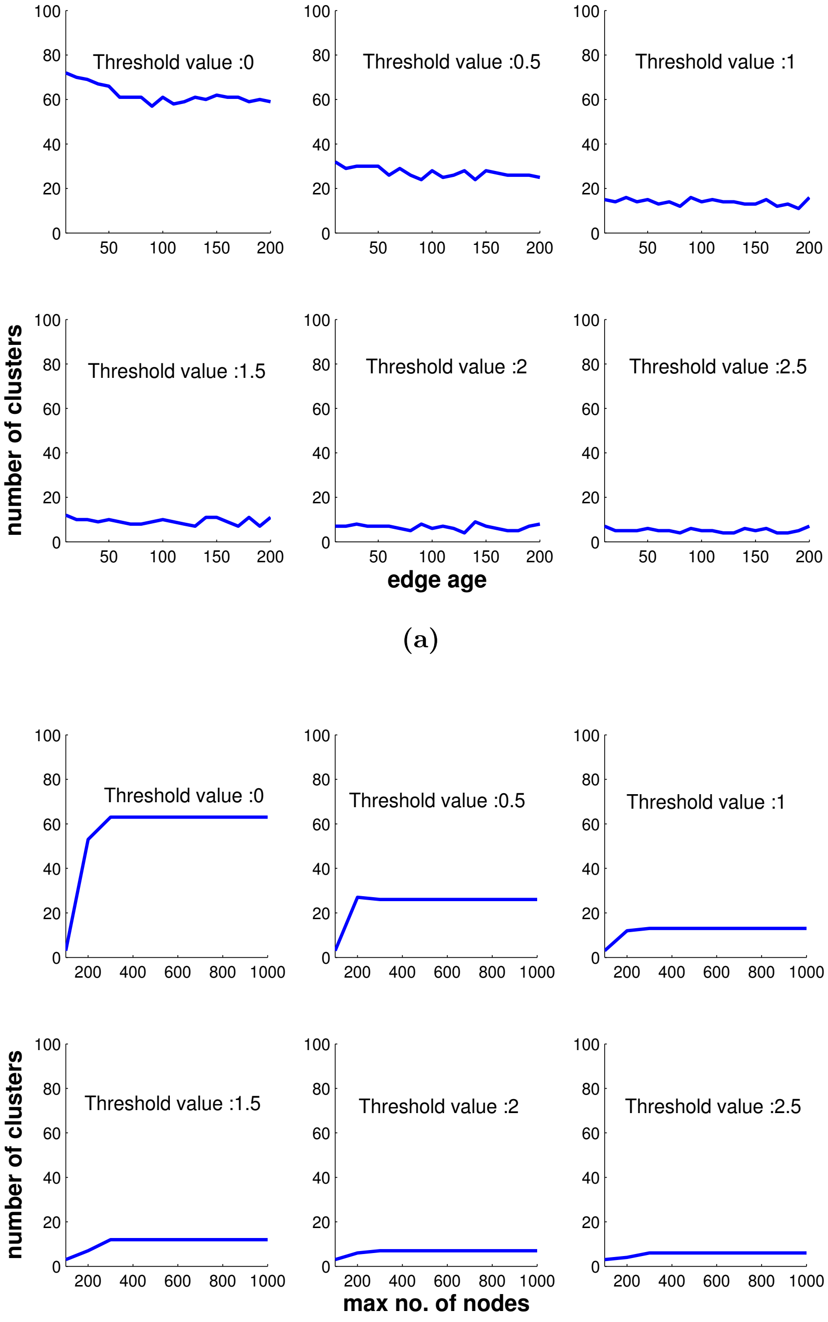

(b)

Figure 4.6: (a) shows the plot of edge age against the number of clusters for different threshold values. The graphs in all the subplots are mostly flat indicating that the edge age parameter has no effect on the number of clusters which result from the GNG algorithm. (b) shows the plot of maximum number of nodes against the number of clusters for different threshold values.

4.3.5 Free Parameters of GNG

Free parameters, unlike other parameters and constants which are constrained by a domain, can assume any value and can be adjusted by the user to a value that may give more meaningful results. There are two free parameters in the GNG algorithm - edge age and maximum number of nodes. For the original run, a value of 88 (which is a default value for edge age) and 1000 were used for edge age and maximum number of nodes, respectively. To verify that these parameters did not have an effect on the number of resulting clusters, a series of experiments were conducted using different values of edge age and maximum number of clusters. The graphs in Fig. 4.6(a) show the plots of number of clusters for different edge age values. Each subplot depicts the resulting graph when a different threshold value was used. The graphs show that for each edge age value, the number of clusters formed, for different threshold values, is approximately the same. Therefore, the value of edge age has no influence on the number of resulting clusters. A similar experiment is performed using different values for the maximum number of nodes. The graphs in Fig. 4.6(b) show the resulting number of clusters for each value of maximum number of nodes, for different threshold values. The graphs show a smaller number of clusters for values of 100 to 300, but after that a plateau is noticed. This indicates that, at a value less than 300, the GNG algorithm runs out of nodes to insert resulting in a smaller number of clusters. This is an incomplete result. Therefore it is best to set the maximum number of nodes parameter to a value higher than 300 in this scenario.

4.3.6 Location of recording(interpositus, medial or lateral)

After the clusters were finalised, it was interesting to see if we could determine the location of the CN neurons in the cerebellum that were more likely to

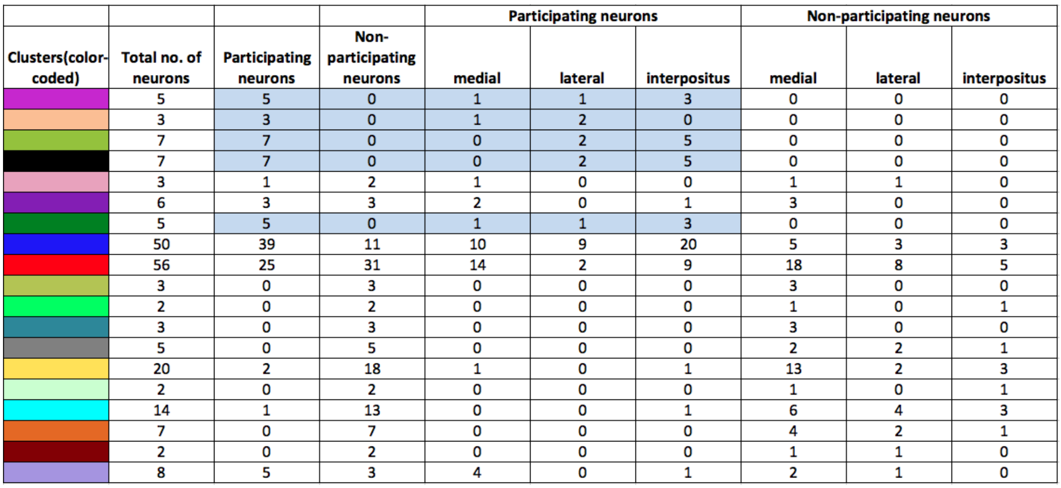

				Participating neurons			Non-participating neurons		
Clusters(color-coded)	Total no. of neurons	Participating neurons	Non-participating neurons	medial	lateral	interpositus	medial	lateral	interpositus
🟪	5	5	0	1	1	3	0	0	0
🟧	3	3	0	1	2	0	0	0	0
🟩	7	7	0	0	2	5	0	0	0
⬛	7	7	0	0	2	5	0	0	0
🟥	3	1	2	1	0	0	1	1	0
🟪	6	3	3	2	0	1	3	0	0
🟩	5	5	0	1	1	3	0	0	0
🟦	50	39	11	10	9	20	5	3	3
🟥	56	25	31	14	2	9	18	8	5
🟩	3	0	3	0	0	0	3	0	0
🟩	2	0	2	0	0	0	1	0	1
🟦	3	0	3	0	0	0	3	0	0
⬜	5	0	5	0	0	0	2	2	1
🟨	20	2	18	1	0	1	13	2	3
🟩	2	0	2	0	0	0	1	0	1
🟦	14	1	13	0	0	1	6	4	3
🟧	7	0	7	0	0	0	4	2	1
🟫	2	0	2	0	0	0	1	1	0
🟪	8	5	3	4	0	1	2	1	0

Figure 4.7: shows the number of neurons in each cluster, the total number of neurons that participate in absence seizures in each cluster and the number of "non-participating" neurons. Additionally for each cluster, the number of medial, lateral and interpositus neurons is given. The clusters are colour coded as in Fig. 4.4. The numbers (highlighted in columns: Participating neurons, Non-participating neurons, medial, lateral and interpositus neurons) suggest that in each cluster that has purely participating neurons, the neurons are predominantly recorded from the interpositus or lateral region. This suggests that interpositus and lateral CN neurons are more likely to participate in absence seizures.

participate in absence seizures. So, I formed a table for each cluster detailing the total number of neurons in each cluster, the total number participating and non-participating neurons. The clusters are color-coded as in Fig. 4.4. Next, for each cluster, I counted how many neurons are situated in the medial, lateral or interpositus for participating and non-participating neurons. We can see from this table that the clusters which have purely participating neurons have a greater number of interpositus or lateral CN neurons. This suggests that CN neurons in the interpositus or lateral region are more likely to modulate their spiking behaviour during absence seizures.

4.4 Chapter Conclusions

Some CN neurons modulate their spiking activity during absence seizures. The clustering results show that there are some purely participating clusters indicating that CN neurons having properties similar to the CN neurons in these clusters are more likely to participate in absence seizures. Interestingly, the analysis of the location of recording of the neurons in these purely participating clusters revealed that these neurons were predominantly located in the interpositus or the lateral nuclei of the cerebellum. As discussed in Chapter 2, Section 2.3.1, the cerebellar nuclei in these regions project to the thalamus and the cerebellar cortex.

Chapter 5

Regression

Contents

In the previous chapter, I used an unsupervised machine learning algorithm - GNG, to find clusters in the dataset. In this chapter, I explore another facet of machine learning: supervised learning.

As mentioned in Chapter 1: Section 1.1.1, a supervised learning algorithm requires the data to be labelled. The data in this case are made up of input-output pairs. The inputs which may be in the form of a numeric vector are called features. The output vectors corresponding to these input vectors are called targets. In other words, we have samples from a function $f : \mathbb{R}^n \longrightarrow \mathbb{R}^m$ and the aim of the supervised learning algorithm is to discover/approximate this function.

So, if there are N input vectors and N corresponding targets, the input-output pairs, where the input vector has d dimensions, can be denoted as shown in the Table 5.1. If the target $\mathbf{y}_i$ is an integer or real value, the learning problem is called regression. If the target $\mathbf{y}_i$ is a label, the learning problem is termed as classification. The Iris dataset [20] is an excellent example of a classification problem. In this dataset, the inputs to the classifier are the sepal length, sepal width, petal length and petal width of the flower. Based on these inputs, the species of the flower *l.setosa*, *l.versicolor* or *l.virginica*, has to be predicted. The outputs or the targets in this dataset, which is the particular species of the flower, are clearly not numeric values. However, even if, for simplicity of representation, numeric values such as 1, 2 and 3 are assigned to represent the different species, still this would not be a regression problem as the numeric values are just a representation of the original class label and do not hold any meaning by themselves. If, for the same Iris dataset, the inputs were sepal length, sepal width, petal length and species and we had to predict the petal width of the flower, then this problem would be a regression problem as the petal width of the flower is a real number.

Inputs	Targets
$\mathbf{x}_1$	$\mathbf{y}_1$
$\mathbf{x}_2$	$\mathbf{y}_2$
.	.
.	.
.	.
$\mathbf{x}_N$	$\mathbf{y}_N$

Table 5.1: shows that the N input vectors and the corresponding N targets.

I use a popular supervised learning algorithm, called Gaussian Processes (GP), to perform non-linear regression in order to predict the measures *FFT based Z-score* and *modulation frequency*, which are discussed in Chapter 3, from the interictal activity of the CN neuron. These measures are used to determine if a CN neuron is likely to participate in absence seizures.

I chose Gaussian Processes (GP) to perform non-linear regression as it provides some advantages over the traditional regression models. Most regression models are parametric in nature that is, they work by assuming a relationship or a function between the input and the target or output. There are a lot of functions available, for example, splines, polynomials, fourier series and so on. It is tedious to try and fit the data to all possible types of function and to adjust the free parameters associated with the function to get the best results in each case. Also, there is the problem of overfitting, that is, if I tune the free parameters of the function too much so that the function fits the existing data perfectly but has limited flexibility, the prediction for the unseen data can be poor. The predictions are better if the function fits the data well but not too well.

Gaussian Processes overcomes the problems of overfitting as it is non-parametric in nature. GP assumes that the function defining the relationship between the input and output pairs is unknown and the data are produced from a (potentially infinite) set of functions, with a Gaussian distribution in the function space [1]. Since, it is a gaussian distribution, the mean and the covariance function are crucial to GP. If the mean function is zero, "the targets are entirely generated from a joint distribution of mean zero and a covariance function" [1]. The covariance function defines how the similarity between the datapoints is calculated.

5.0.1 Prediction using a GP model

This section shows how the prediction process in a GP model works. Consider a set of input vectors, $\mathbf{X}$=$\mathbf{x}_1$...$\mathbf{x}_N$ where N is the number of input vectors, and the corresponding output vectors are given by $\mathbf{y}_1$...$\mathbf{y}_N$. As also shown in

[1], the covariance matrix (K) between all the input vectors $\mathbf{x}$ is calculated as shown below

$$K = \begin{pmatrix} k(\mathbf{x}_1, \mathbf{x}_1) & k(\mathbf{x}_1, \mathbf{x}_2) & \ldots\ldots\ldots & k(\mathbf{x}_1, \mathbf{x}_N) \\ k(\mathbf{x}_2, \mathbf{x}_1) & k(\mathbf{x}_2, \mathbf{x}_2) & \ldots\ldots\ldots & k(\mathbf{x}_2, \mathbf{x}_N) \\ \ldots\ldots\ldots & \ldots\ldots\ldots & \ldots\ldots\ldots & \ldots\ldots\ldots \\ k(\mathbf{x}_N, \mathbf{x}_1) & k(\mathbf{x}_N, \mathbf{x}_2) & \ldots\ldots\ldots & k(\mathbf{x}_N, \mathbf{x}_N) \end{pmatrix}$$

where $k(\mathbf{x}_i, \mathbf{x}_j)$ shows the similarity between $\mathbf{x}_i$ and $\mathbf{x}_j$. If now a new input vector $\mathbf{x}_*$ is added to the input space, then the corresponding $\mathbf{y}_*$ is predicted using the Eq. 5.1

$$E[\mathbf{y}_*] = \mathbf{k}_*^T (K + \sigma_n^2 I)^{-1} \mathbf{y} \tag{5.1}$$

where $\mathbf{k}_*$ is the covariance vector between $\mathbf{x}_*$ and $\mathbf{X}$, I is an identity matrix, σ_n^2 is "the variance of an identically distributed Gaussian noise" [1]. The Gaussian noise is added to the covariance function to make it more flexible. $\mathbf{y}$ is the output vector.

From the Eq.5.1, it is easy to see that the value for $\mathbf{y}_*$ is nothing but "a weighted average of the values of $\mathbf{y}$ with the weights being determined by the covariance of the $\mathbf{x}_*$ with $\mathbf{X}$" [1]. However, the weights are not just equal to the distance between the points, but given by a Gaussian function of the distance as shown in Fig. 5.1(a).

Ashrafi et al. [1] give a simple example of how a GP regression works. In this case, there is dataset consisting of two points: the first point is (x1,y1)=(1,2) and the second one is (x2,y2)=(3,4). "The task is to predict the corresponding value of y for a new value of x_*" [1]. The simplest approach is just to take the weighted value of existing ys weighted by the distance of the new point from the existing point. $y* = (d(x*, x1)y1 + d(x*, x2)y2)/2$. In actual fact, in a Gaussian Process the distance is put through a Gaussian

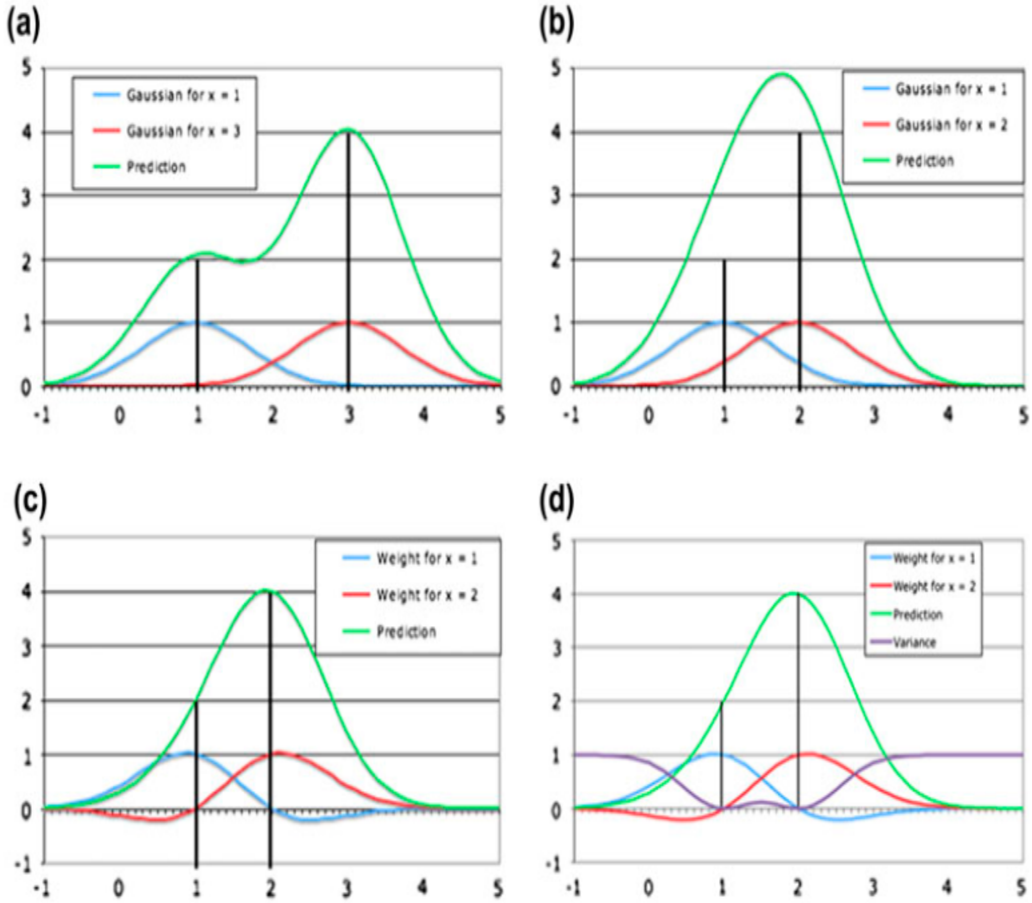

Figure 5.1: (a) shows that the prediction (green line) is a result of a Gaussian function of the weights at 1 (blue line) and 3 (red line). The prediction line passes very close to the actual values of y (shown by the black bars) when the data points are well separated and the Gaussian weights at 1 and 3 have minimal influence on each other. (b) shows that the prediction is over-estimated when the data-points are closer to each other and both the weights at 1 and 3 contribute heavily to the prediction.(c) the solution to the over-estimation is to force the weights to zero whenever the prediction passes through a data point. This time the prediction is correct. (d) shows that the variance of the prediction can also be calculated as shown by the purple line. It is clear that the variance at the actual data-points is zero and increases as we move away from the data-points. Source: [1].

function so that distant points have less impact.

In the Fig. 5.1(a), the Gaussian weights of $x = 1$ are shown by the blue line, and the Gaussian weights at $x = 3$ are shown by the red line. The prediction of y due to these two weights is shown by the green line. When the data points are well separated, as in Fig. 5.1(a), the prediction line is shown to pass very close to the actual values of y (shown by the black bars). However, if the data points are closer to each other as shown in the Fig.5.1(b), the y value is over-estimated. This happens because both the Gaussian weights at x=1 and x=2 contribute heavily to the prediction. To resolve the issue of overestimation, the Gaussian weights are forced to zero whenever they pass through any data points. The new prediction is as shown in Fig. 5.1(c).

It is also possible to derive a variance for the prediction y_* as shown by the purple line in Fig. 5.1(d). The variance of y_* is given by the Eq. 5.2

$$var[y_*] = k(x_*, x_*) - k_*^T (K + \sigma_n^2 I)^{-1} k_* \tag{5.2}$$

where $k(x_*, x_*)$ is the variance of x_*.

From Eq. 5.2, it is clear that if the new data-point is closer to an existing data-point, the weights are higher and consequently the variance is lower. If the new data-point is located further away from existing data-points, the Gaussian weights have minimal influence on the new data-point and the variance in this case is higher.

5.0.2 Covariance Functions

The selection of the covariance function is very important to the GP as it determines the type of functions that make up the prior and it determines how the closeness between the input data points is calculated. A covariance function is an example of a kernel, which is a function that takes two inputs, scalar or vector, and produces a real value as output. A function has to satisfy some conditions in order to be considered a kernel. The conditions the kernel K needs to satisy are:

For any x and y,

- The function should be symmetric, $K(x, y) = K(y, x)$.
- The function should be maximal when its two inputs are identical (after all the kernel is trying to measure similarity) that is, $K(x, x) >= K(x, y)$.
- it should be non-negative, $K(x, y) >= 0$.
- it should be a continuous function, that is, a small change in x or y (or both), should produce a small change in $K(x, y)$ that is : $\dfrac{\partial K}{\partial x}$ and $\dfrac{\partial K}{\partial y}$ are always finite.

Rasmussen et. al [59] give a list of some commonly used covariance functions as shown in Fig 5.2. The most frequently used function to do a GP regression

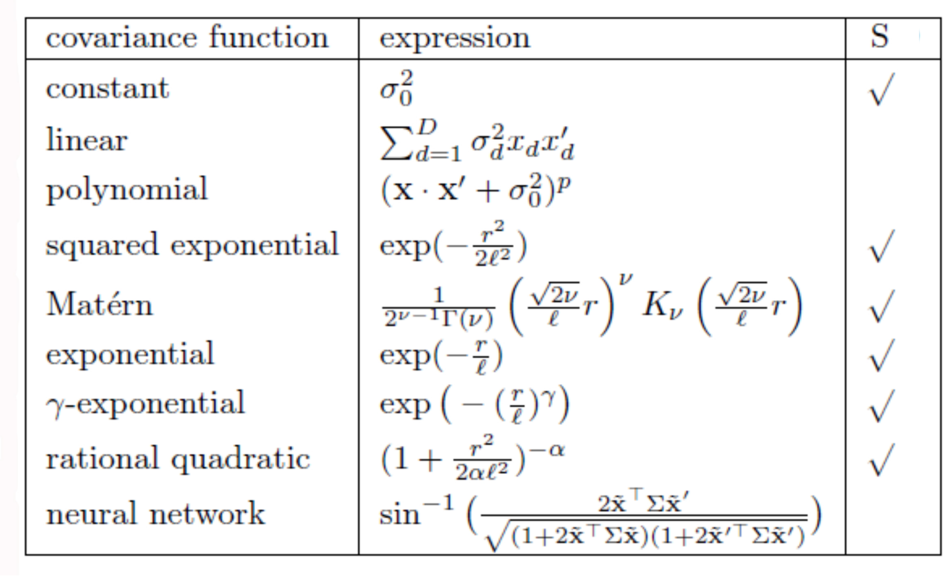

covariance function	expression	S
constant	σ_0^2	✓
linear	$\sum_{d=1}^{D} \sigma_d^2 x_d x'_d$	
polynomial	$(\mathbf{x} \cdot \mathbf{x}' + \sigma_0^2)^p$	
squared exponential	$\exp(-\frac{r^2}{2\ell^2})$	✓
Matérn	$\frac{1}{2^{\nu-1}\Gamma(\nu)} \left(\frac{\sqrt{2\nu}}{\ell} r\right)^{\nu} K_\nu \left(\frac{\sqrt{2\nu}}{\ell} r\right)$	✓
exponential	$\exp(-\frac{r}{\ell})$	✓
γ-exponential	$\exp\big(-(\frac{r}{\ell})^\gamma\big)$	✓
rational quadratic	$(1 + \frac{r^2}{2\alpha\ell^2})^{-\alpha}$	✓
neural network	$\sin^{-1}\big(\frac{2\tilde{\mathbf{x}}^\top \Sigma \tilde{\mathbf{x}}'}{\sqrt{(1+2\tilde{\mathbf{x}}^\top \Sigma \tilde{\mathbf{x}})(1+2\tilde{\mathbf{x}}'^\top \Sigma \tilde{\mathbf{x}}')}}\big)$	

Figure 5.2: shows some commonly used covariance functions in GP. The r value is calculated as the absolute distance between two points x and x' that is $r = |x - x'|$. l is the length-scale and σ is the standard deviation of the signal. The column S indicates whether the function is stationary. Source: [59]

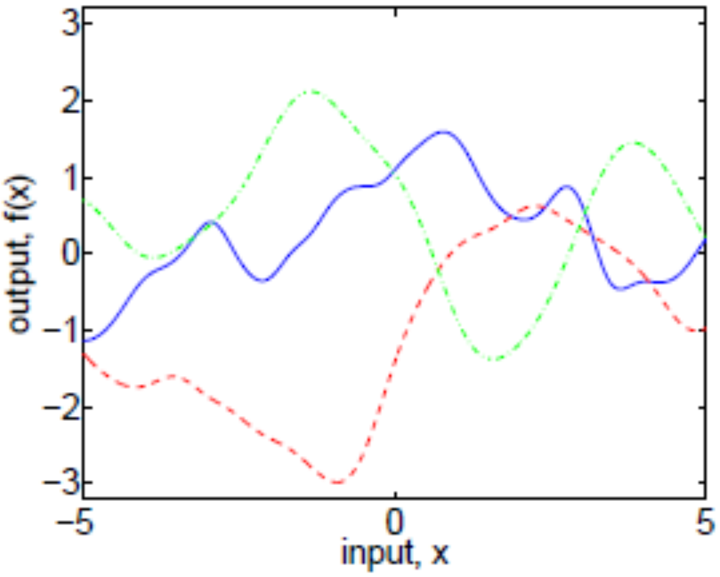

Figure 5.3: shows some random functions taken from a GP with a rational quadratic covariance function with different values for α and l=1. Source:[59]

is the Squared-exponential (SE) covariance function. It is given by the Eq. 5.3

$$k(x_p, x_q) = exp(-\frac{(x_p - x_q)^2}{2l^2}) \tag{5.3}$$

Since this function is dependent on $x_p - x_q$, this covariance function is stationary. The SE function basically states that the data points influence each other more if they are close to each other and not so much if they are further away.

Another popular covariance function is the Rational Quadratic Covariance (RQ) function shown in Fig. 5.3. It is given by the Eq. 5.4

$$k_{RQ}(x_p, x_q) = (1 + \frac{(x_p - x_q)^2}{2\alpha l^2})^{-\alpha} \tag{5.4}$$

This covariance function is similar to adding several SE covariance kernels which have varying length-scales given by l. The hyperparameter α determines the extent of variation (large or small variations) in the function. If α is very

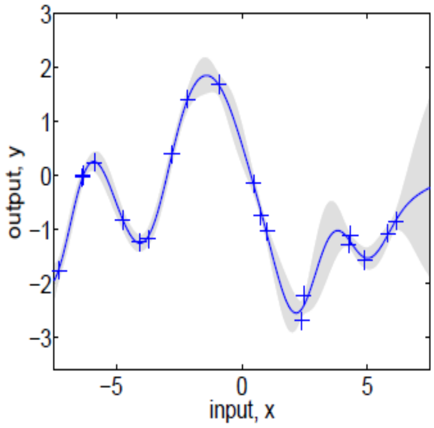

(a), $\ell = 1$

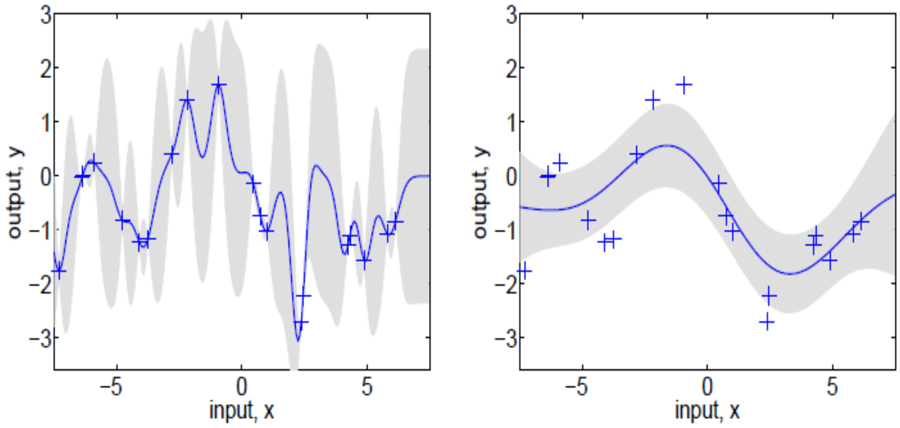

(b), $\ell = 0.3$ (c), $\ell = 3$

Figure 5.4: shows the effect of hyperparameter values on GP modeling. The data points observed are marked by +, the solid line shows the underlying mean function and the grey area around the function shows the errorbars or 2 standard devations. (a) l=1, σ_f^2= 1 and σ_n^2=0.1 (b) l=0.3, σ_f^2= 1.08 and σ_n^2=0.00005 (c) l=3, σ_f^2= 1.16 and σ_n^2=0.89. Source: [59].

large, then the RQ kernel is equivalent to the SE kernel.

In my regression experiments, I found that the RQ covariance function gave me the best result in predicting *FFT based Z-score* and *modulation frequency* as discussed in Section 5.3.

5.0.3 Hyperparameters

The equation given for the Squared- Exponential (SE) covariance function in Eq. 5.3 is based on the assumption that the observations made are noise-free. However, adding noise to the covariance function is more realistic and provides a more robust model. The Eq. 5.3 can be re-written as shown in Eq. 5.5

$$k_n(x_p, x_q) = \sigma_f^2 exp(-\frac{(x_p - x_q)^2}{2l^2}) + \sigma_n^2 \delta_{pq} \tag{5.5}$$

where l is the *length-scale*, σ_f^2 is the *signal-variance* and σ_n^2 is the noise variance multiplied by δ_{pq} (Kronecker delta) which has a value of 1 when p and q are equal and zero otherwise [1]. The length-scale parameter, l, determines the smoothness of the functions.

Rasmussen et al. [59] explain the effect of these hyperparameters with the help of a simple example as shown in Fig. 5.4. In Fig. 5.4(a), the length-scale parameter is set to 1. The values for σ_f^2 and σ_n^2 is determined as 1 and 0.1 respectively by a model selection method such as cross-validation or marginal likelihood. The error bars show 2 standard deviations. It can be seen that the function is smooth and the errorbars are smaller where data are present and larger where there is no data. If the value for the length-scale was changed to 0.3 but the x-axis and the other parameters was maintained the same, the function line will become more wiggly in appearance.

However, if the value for the hyperparameter, l is changed to 0.3, and the other parameters are set by picking the optimal parameters as dictated by a model selection method such as marginal likelihood or cross-validation, then we would see a function as seen in Fig. 5.4(b). The parameters σ_f^2 and σ_n^2 would take the value of 1.08 and 0.00005 respectively. The lower value for noise is due to the higher value of σ_f^2, that is, there is greater flexibility for the signal, so a higher value for the noise is not required. Also, any sharp variations in the data, which was previously attributed to noise, is now entirely attributed to the variation in the underlying function, therefore the errors bars in between the data points rapidly move away.

In contrast, if the length-scale is too long as in Fig. 5.4(c), with the value of $l = 3$, the noise value selected by using a model selection method is 0.89 and the *alpha* is set as 1.16. In the case of a longer *length-scale*, much of the variance is attributed to noise, so the function itself varies very little as shown by the smooth function of Fig. 5.4(c). This example illustrates that the selection of the correct values for the hyperparameters is crucial to GP modeling. In this example, if a model selection method such as cross-validation is used, it would chose the hyperparameter values as shown in Fig. 5.4(a) as this function gives the best fit.

5.1 Model Selection

In Fig. 5.4, we can see that a lot of variation is possible in the type of function produced even when the same covariance function is used for GP modeling. Therefore, we need a way to compare different models produced by GP modeling and select the model best suited to predict unseen data. The most commonly used method to compare models produced by GP modeling is cross-validation.

5.1.1 Model Building and Testing

To select the model for GP regression, the dataset is divided into n segments. The first $n-1$ segments form the training set and the nth segment is chosen as the test set. The training set and the test set should be disjoint, that is, no rows found in the training set should appear in the test set. The GP regression modeling is carried out on the training set. During the training, the GP model learns the relationship between the input and its corresponding targets. The covariance function and the hyperparameters are selected for the GP model in this stage.

Once the training is complete, unseen data in the test set are now presented to the model. The performance of the model is determined by calculating the mean square error (MSE) between the predicted and the actual target values. This process is repeated n times by shuffling the segments in the test and training set such that each segment in the data set has an opportunity to be the test set once. The GP model which produces the least MSE for the n trials is selected as the final version of the model.

5.2 Measuring Performance of a Classification Task

Apart from performing regression, I also perform classification on the results produced by the GP regression model by using the assumption that a CN neuron is likely to participate if its *FFT based Z-score* >=1.96 and *modulation frequency* is between 6-9 Hz, as explained further in the Section 5.3. Here, I explain how the performance of the classification results is measured.

In a classification task where there are two equally sized classes, measuring performance is straight forward. You simply report accuracy, the proportion of the test data that you accurately classify. For example, a classifier that is right 80% of the time is definitely better than one that gets it right 60% of the time. However most tasks, including mine, do not have balanced classes and simply reporting accuracy may be misleading. For example, if one class has 98% of the data, and the other class has the remaining 2%, then the performance of 80% is not good at all and may actually be worse than the accuracy of 60%. The reason for this, is that simply by making the useless prediction that **everything** is in the majority class will give you an accuracy

	Predicted Positives	Predicted Negatives
Actual Positives	True Postive (TP)	False Negative (FN)
Actual Negatives	False Positive (FP)	True Negative (TN)

Table 5.2: shows a *confusion matrix*

of 98% without telling you anything about the real class of the data.

To facilitate the discussion, we describe our test data as consisting of positive and negative examples of our class of interest (for example, participating neurons). For the case of so-called unbalanced data, as my data is, specialised measures must be used. I primarily use the *F-score*, and to obtain this a *confusion matrix* should be constructed. For this, the four measures: True Positive, True Negative, False Positive and False Negative need to be found. A prediction can be either correct or incorrect. A correct prediction for an item of positive class is called a True Positive (TP). In fact, the four cases can be identified as shown in the Table 5.2 and as shown in [60]. Based on this *confusion matrix* the values for *Accuracy*, *Recall*, *Precision* can be calculated as shown in the Equations 5.6 , 5.7 and 5.8; also shown in[60].

$$Accuracy = \frac{True\ Positives + True\ Negatives}{Total\ no.\ of\ items} \tag{5.6}$$

$$Recall = \frac{True\ Positives}{Actual\ Positives} \tag{5.7}$$

$$Precision = \frac{True\ Positives}{Predicted\ Positives} \tag{5.8}$$

where Actual Positive is True Positives + False Negatives and Predicted

Item No.	Class Label	Model A Results	Model B Results
1	+	+	-
2	-	+	-
3	+	+	+
4	+	+	-
5	-	+	-
6	+	-	-

Table 5.3: Example data

Positives is True Positives + False Positives.

For example, consider the unbalanced data shown in the Table 5.3. The data consists of 6 items, out of which 4 are actual positives and 2 are actual negatives. Now, suppose the classifier predicts 3 of the actual positives as positives and none of negatives are correctly identified, then the confusion matrix can be formed as shown in Table 5.4.

	Predicted Positives	Predicted Negatives
Actual Positives (4)	TP = 3	FN = 1
Actual Negatives (2)	FP = 2	TN = 0

Table 5.4: shows an example (Model A results in Table 5.3) of a *confusion matrix* for good *Recall* and poor *Precision*.

Now, from the *confusion matrix*, the following measures can be calculated. Firstly, "*Recall* measures the proportion of the actual positives that are predicted" [60], in this case 75% (3 of 4), and the "*Precision* measures the proportion of positive predictions that are correct" [60] which is 60% (3 of 5). To interpret this, our predictor is good at recalling the True Positives but does this at cost of the prediction by predicting too many positives.

However, if for the same data the classifier predicts only 1 of the actual positives as positive and identifies both of the actual negatives as negative the confusion matrix would be as shown in the Table 5.5. The *Recall* in this case is poor at 25% (1 of 4). However, the *Precision* is excellent at 100%. This predictor is also not good as it is not good at recalling True Positives. Obviously a good balance is needed between good *Recall* and *Precision* and a normal way of combining them is to use the *F-Score*, calculated as shown in Eq. 5.9 and [60], which rewards both high *Recall* and high *Precision*. Fig. 5.5 shows how the *F-score* penalises poor *Precision* and poor *Recall* compared to a measure which calculates the average of *Precison* and *Recall*.

	Predicted Positives	Predicted Negatives
Actual Positives (4)	TP =1	FN = 3
Actual Negatives (2)	FP = 0	TN = 2

Table 5.5: shows an example(Model B results in Table 5.3) of a *confusion matrix* for good *Precision* and poor *Recall*.

$$F - score = \frac{2 \times Recall \times Precision}{Recall + Precision} \tag{5.9}$$

5.3 Results

The purpose of using a GP model in my research is to predict the two measures: *FFT based Z-score* and *modulation frequency* from the interictal activ-

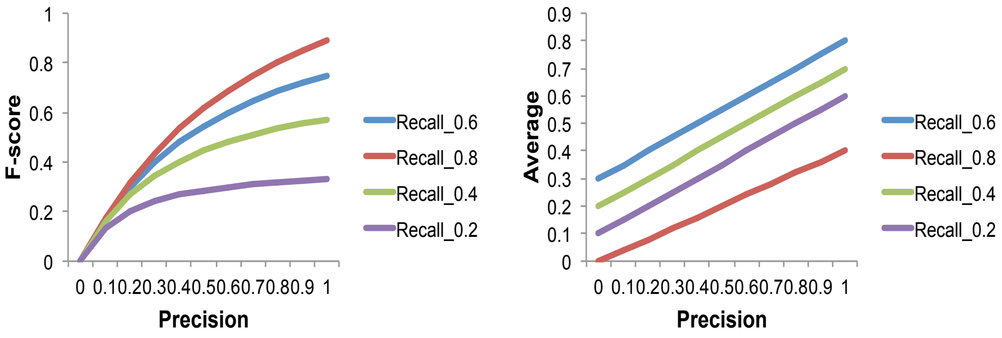

(a) (b)

Figure 5.5: (a) shows the value of *F-score* for different values of *Precision* and *Recall*. The *F-score* is low for poor *Precision* values even when the *Recall* values are high. That is *F-score* penalises poor *Precision* and poor *Recall*. (b) shows the average. This measure is not a good measure because it does not penalise low values of *Recall* or *Precision* and does not reward high *Recall* values even when the *Precision* is high as shown by the red line. The main point is that when we have a precision of 0, the *F-score* says that the classifier is useless whereas the average says it is still useful.

ity of the CN neurons. Since both the measures are continuous values, the prediction of the values is a regression problem.

I constructed two separate GP models: one to predict the *FFT based Z-score* and the other to predict the *modulation frequency*. The measures, as detailed in Chapter 3: Section 3.2, which describe the interictal activity of the CN neurons were selected as the features to the GP model. We used subsets consisting of different combinations of these features. For each of these combinations, the GP regression was performed using different covariance functions, listed in Fig. 5.2, and different values for hyperparameters.

The hyperparameters were selected using the method of cross-validation as detailed in Section 5.1. That is, the data set which consisted of 208 rows of data was divided into 5 segments: out of which 4 segments were used for training and the remaining segment was used as the test set. The process was repeated 5 times such that each segment had the chance to be the test set. For the five runs, the Pearson correlation coefficient r was calculated for the

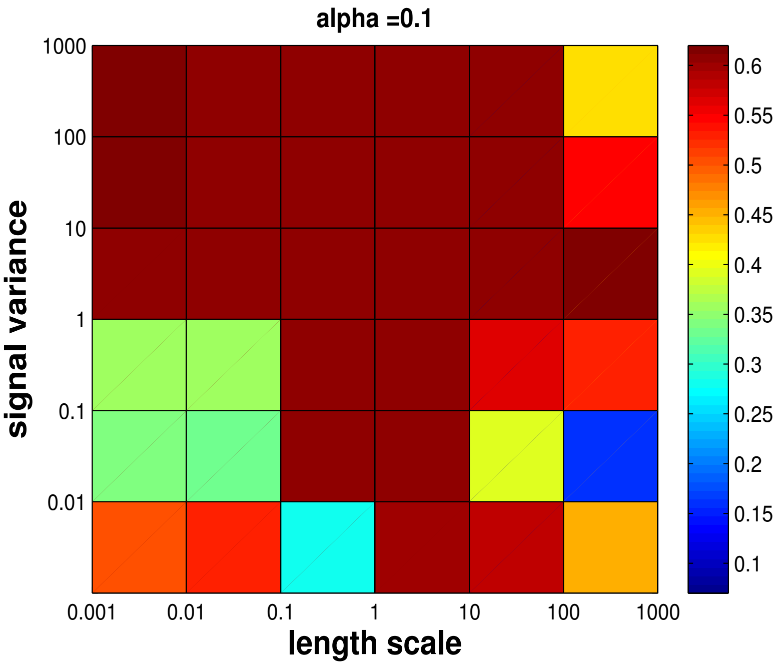

Figure 5.6: shows a coarse grid search for the best values for hyperparameters: *length-scale* and *signal-variance* when *alpha* =0.1 using the cross-validation method. The colormap shows the values for the Pearson correlation coefficient r. We can see that the r value is the best in region where *signal-variance* $>$10 and *length-scale*$<$0.01. Also, a high value for r was observed when *length-scale* $>$100 and *signal-variance* is between 1-10. This is a snapshot of the search conducted for the hyperparameter values. This search was also done for different values of *alpha* ranging from 10^{-3} to 10^{+3}. Further, a fine grid search was conducted in areas where the r value was the highest.

actual vs. the predicted value of *FFT based Z-score*. The r value was taken as the measure of performance of the GP model.

To select the values for the hyperparameters, first, a coarse grid search was conducted with the values for each hyperparameter: *length-scale*, *signal-variance* and *alpha*, consisting of logarithmic values, that is, for each power of 10 ranging from 10^{-3} to 10^{+3}. Fig. 5.6 shows a snapshot of the search conducted for the best values for the hyperparameters: *length-scale* and *signal-variance*, when the hyperparameter *alpha*=0.1. The colormap in Fig. 5.6 shows the range of r values. We observe that a high r value is obtained when the *signal-variance* $>$10 and *length-scale*$<$0.01. Also, a high value of r is no-

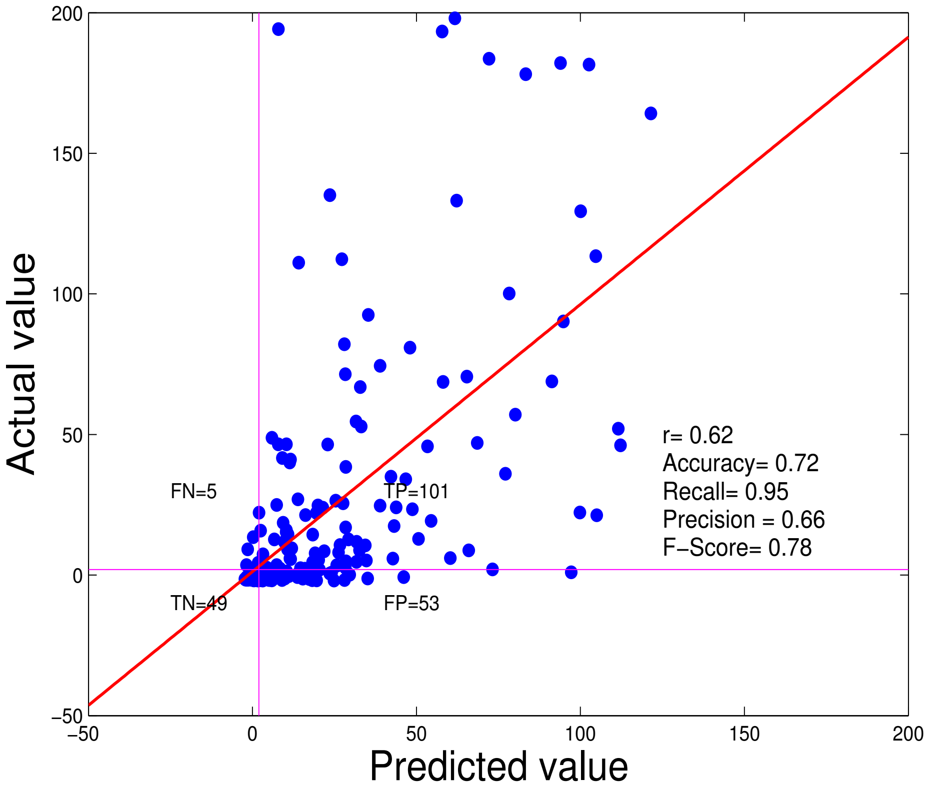

Figure 5.7: shows the plot of actual vs. predicted value of *FFT based Z-score* produced by the GP model. I was able to achieve a good prediction rate (Pearson correlation coefficient) (r) of 0.62. Further, I created a *confusion matrix* on the assumption that a *FFT based Z-score* of 1.96 or higher was required for the CN neuron to participate. The 1.96 threshold is shown by the pink lines. I classified the CN neurons that were actually participating and were predicted as participating as true positive (TP), the CN neurons that were actually not participating and were identified as such as true negative (TN). The CN neurons which were either participating or non-participating but were incorrectly identified as non-participating and participating were termed as False Negative (FN) and False Positive (FP) respectively. I achieved a precision of 0.66 which means that 66% of the CN neurons which were identified as participating were actually participating. Also I achieved a recall of 0.95 which means I identified 95% of the neurons of the total participating neurons.

ticed when *length-scale* >100 and *signal-variance* is between 1-10. This figure does not show the entire search conducted and is merely a snapshot when *alpha*=0.1. Further, a logarithmic search was also conducted for different values of *alpha* for each power of 10 in the range of 10^{-3} to 10^{+3}. Finally, a fine grid search was conducted in the areas where coarse grid search showed a higher value for r. We were able to achieve the best r value (r=0.62) when *signal-variance* was 1, *length-scale* was 120 and *alpha* was 0.1.

The combination of features that gave us the best prediction for *FFT based Z-score* were *mean_ CV2*, *CV*, *burst-like spike ratio* and *permutation entropy.* The covariance function that gave the best results was the Rational Quadratic covariance function, which has been explained in Section 5.0.2. As shown in Fig. 5.7, the r value, the Pearson correlation coefficient [55], which calculates the correlation between the actual and predicted *FFT based Z-score* was 0.62. This value shows that there is a good correlation between the actual and the predicted value. Also, this correlation was not a matter of chance as the p-value of the Pearson correlation coefficient was significantly less than 0.05.

Further, I created a *confusion matrix* based on the assumption that a CN neuron with a *FFT based Z-score* greater than or equal to 1.96 is likely to participate in the seizure activity. The threshold of 1.96 is shown by the pink lines in Fig. 5.7. This means that CN neurons that have been correctly identified as participating that is the predicted and the actual *FFT based Z-score* was greater than or equal to 1.96, are classified as true positive (TP). The CN neurons which have been correctly identified as non-participating form the true negatives (TN). The CN neurons that have been incorrectly identified as non-participating or participating are classified as false negative (FN) and false positive (FP) respectively. The values for accuracy, recall, precision and F-score are calculated using the equations 5.6, 5.7, 5.8 and 5.9. Using this classification method, I achieved a precision of 0.66 and a recall of 0.95. This means that 66% of the neurons that were identified as participating were actually participating and 95% of the total neurons that were participating were correctly identified.

The prediction of the second measure *modulation frequency* proved to be

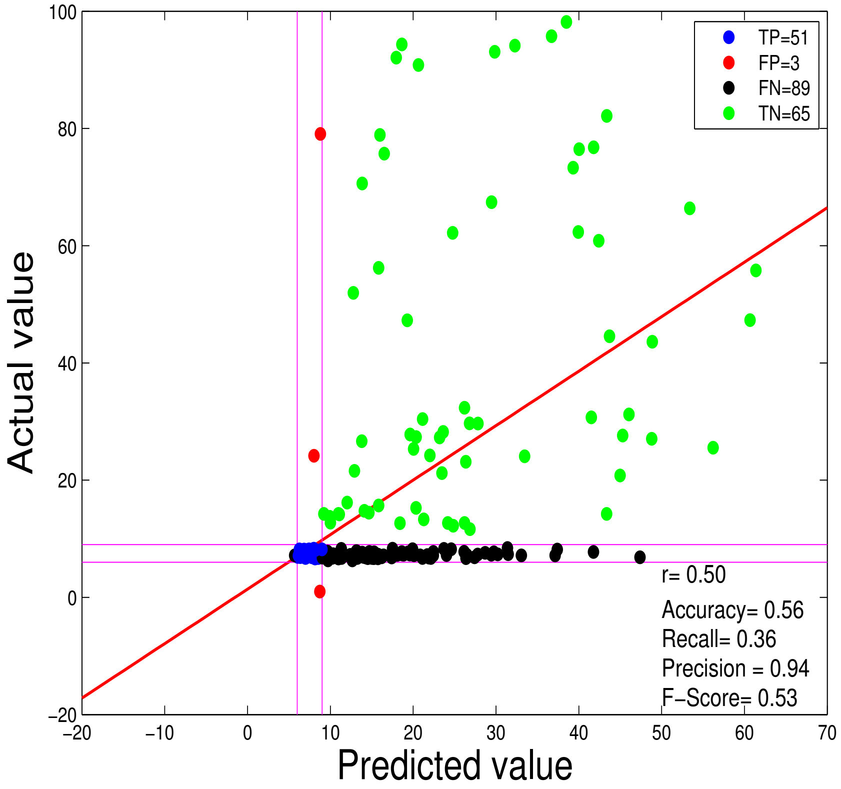

Figure 5.8: shows a plot of actual vs. predicted value of *modulation frequency* produced by the GP model. Here, the predicted value of the *FFT based Z-score* produced by the previous experiment, as shown in the Fig. 5.7, is used as an input along with the feature *CV*. I was able to get an average value of $r = 0.50$ for this prediction. Further, a *confusion matrix* is produced on the assumption that a CN neuron with a *modulation frequency* between 6-9Hz is likely to participate. Even though the precision is 0.94, that is almost all the CN neurons that were identified as participating were actually participating, the recall was low which means that only 36% of the total CN neurons which were actually participating were correctly identified.

more challenging. All the existing features or any combination of the features for any covariance function was not able to get good prediction rates. Interestingly, when I combined the predicted value of *FFT based Z-score* produced by our GP model with the *CV* I was able to get better results. I initially thought that this is a novel way of prediction. However, this concept of using the output of one classifier as an input to another had been explored before

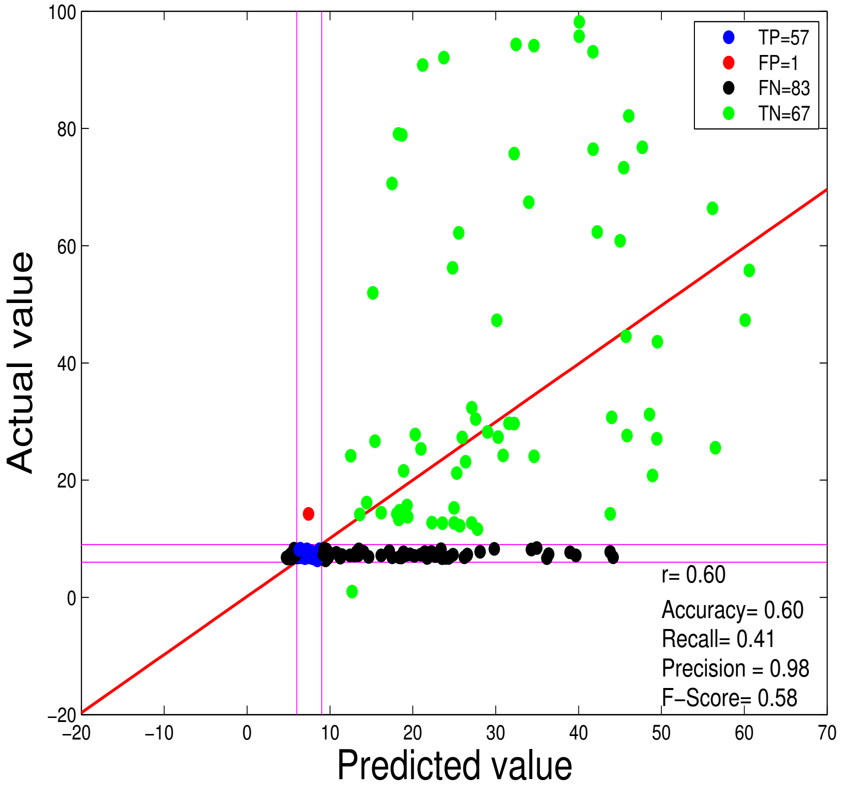

Figure 5.9: shows the plot of actual vs predicted value of *modulation frequency* produced by the GP model. The main difference between this result and the result shown in Fig. 5.8 is that instead of the predicted value of *FFT based Z-score* used as input to the GP model, I use the actual values. When the actual values of *FFT based Z-score* are used, we see an improvement in the r value.

by Wolpert in 1992 and is called stacking [72]. I achieved an r value of 0.50 with $p<0.05$ as shown in the Fig. 5.8. Further, instead of using the predicted value of *FFT based Z-score*, if I used the actual values, I was able to get a slightly better prediction rate. The r value in this case increased to 0.60 with $p<0.05$ as shown in Fig. 5.9. The covariance function used for this GP model was the Rational Quadratic covariance function, which is the same covariance function used in the prediction of *FFT based Z-score.* I did a coarse grid search followed by a fine grid search to find the best value for the hyperparameters. The value of hyperparameters that gave the best result was: *length-scale*=76, *signal-variance* =75 and *alpha*=0.01.

As before, I also created a *confusion matrix* based on the assumption that a CN neuron with a *modulation frequency* between 6 to 9 Hz is likely to participate. The classification in this case was not that successful. Even though our precision value was 0.94 and 0.98 for the predicted and the actual value of *FFT based Z-score*, as shown in Fig. 5.8 and Fig. 5.9 respectively, that is almost all neurons that were identified as participating were actually participating, the recall value was low which meant approximately 64% of the total CN neurons which were participating were not correctly identified.

5.4 Chapter Conclusions

In this chapter, I explored supervised learning and I attempted to predict the values of *FFT based Z-score* and *modulation frequency* from the measures that describe the interictal activity of the CN neurons. I got a good prediction rate of r=0.62 for *FFT based Z-score* and r=0.50 for *modulation frequency*) by the GP models I have constructed. However, if co-efficient of determination (r^2) is taken into consideration, it can be seen that the proportion of the variance explained by the GP model in case of *FFT based Z-score* is just 38%. This means that even though the correlation between the predicted and observed values is significant, it is not strong.

Chapter 6

Computer Simulations and Evolutionary Algorithm

Contents

The analysis of the clustering results, Chapter 4: Section 4.3.3, showed me that there is a difference in the interictal spiking patterns of participating and non-participating neurons. So, I set out to investigate the input conditions in the CN neurons that produce the spiking patterns observed during the interictal periods in the participating neurons. The motivation behind this study was not only to gain an understanding of the input conditions in the participating neurons during the interictal periods but also to investigate the change that occurs in the input conditions when the CN neuron output shifts from an interictal spiking pattern to an ictal spiking pattern.

6.1 CN Neuron Model

In order to simulate a CN neuron and to reproduce the interictal spiking pattern of a participating neuron, I used a morphologically realistic conductance-based model of an excitatory CN projection neuron; for details about the CN neuron model, see Chapter 2: Section 2.4.

As shown in Fig. 2.9 in Chapter 2, the GADnL CN neuron, which is an excitatory CN projection neuron, receives excitatory input from mossy fibres and inhibitory input from Purkinje cells. In the CN neuron model, I use the parameters listed below, with the realistic ranges of values shown, to set the characteristics of the excitatory and the inhibitory input.

- Inhibitory input frequency [0 - 200Hz]
- Excitatory input frequency [0 - 200Hz]
- Inhibitory noise [0 - 1]
- Excitatory noise [0 - 1]
- Inhibitory burst duration [0 - 500ms]
- Excitatory burst duration [0 - 500ms]
- Inhibitory interburst interval [0 - 500ms]

- Excitatory interburst interval [0 - 500ms]
- Inhibitory burst randomness [0 - 100%]
- Excitatory burst randomness [0 - 100%]
- Purkinje cell synchronicity [1, 5, 15, 45, 90, 150, 225, 450]
- Mossy fibre synchronicity [1, 5, 15, 30, 75, 150]
- Inhibitory synaptic weight [0 - 300%]
- Excitatory synaptic weight [0 - 300%]

The first two parameters are used to set the firing rate of the input from the Purkinje cells and the mossy fibres. The noise parameters are used to set the irregularity of Purkinje cell and mossy fibre firing. A noise value of 0 ensures that the input is completely regular, that is, the interspike intervals (ISIs) do not vary and correspond to the inverse of the specified mean firing rate. A noise value of 1 means that the ISIs are drawn from a gamma distribution of the chosen order with the mean ISI corresponding to the inverse of the specified mean rate [43]. The ISI is calculated as shown in the equation 6.1.

$$ISI = (1 - x)y + xyz \tag{6.1}$$

where, x is the irregularity setting, y is the desired mean ISI and z is a random number between 0 and 1 drawn from a gamma distribution of specified order. The gamma distribution in these set of experiments was set to the default value of 3.

The burst duration and burst interval parameters indicate the length of the bursts and the intervals between the bursts, respectively. The burst randomness parameters indicate if the occurrence of the bursts across the inputs is synchronous. All the parameters, except Purkinje cell synchronicity and mossy fibre synchronicity, are real valued numbers. The Purkinje cell synchronicity and the mossy fibre synchronicity determine the number of Purkinje cells and the number of mossy fibres converging on to the CN neuron. According to the current literature, the number of Purkinje cells and, in particular, mossy fibres converging onto a single CN neuron is unclear. Therefore, the number of Purkinje cells converging on to our CN neuron model is set to range from [1-450] and the number of mossy fibres to range from [1-150]. If the value of convergence is set to 1, it is equivalent to having a totally synchronous input. The synaptic weight parameters determine the strength of the connection between the CN neuron and the neuron providing the input.

For each simulation, I varied the values of these input parameters and then recorded the resulting spike train produced by the CN neuron model. Next, I calculated the measures *CV*, *mode ISI* and *burst-like spike ratio*, see Chapter 3: Section 3.2, for the output of the simulation and then projected the result onto the clusters created by the application of the GNG algorithm to the experimental data, see Chapter 4: Section 4.3.3. If the output of the simulation was projected onto a purely participating cluster, I would have managed to replicate the interictal spiking pattern of a CN neuron that participates in absence seizures. Thus, the aim of this experiment was to find the combination of input parameter values which would place the output into a participating cluster. Since there are multiple input parameters that need to be optimised, this is a problem which can be solved effectively using Evolutionary Algorithms.

6.2 Evolutionary Algorithms

Evolutionary algorithms (EAs) are based on the concept of Darwinian evolution [15] and apply the principle of "survival of the fittest" to find solutions to complex optimisation and computational problems.

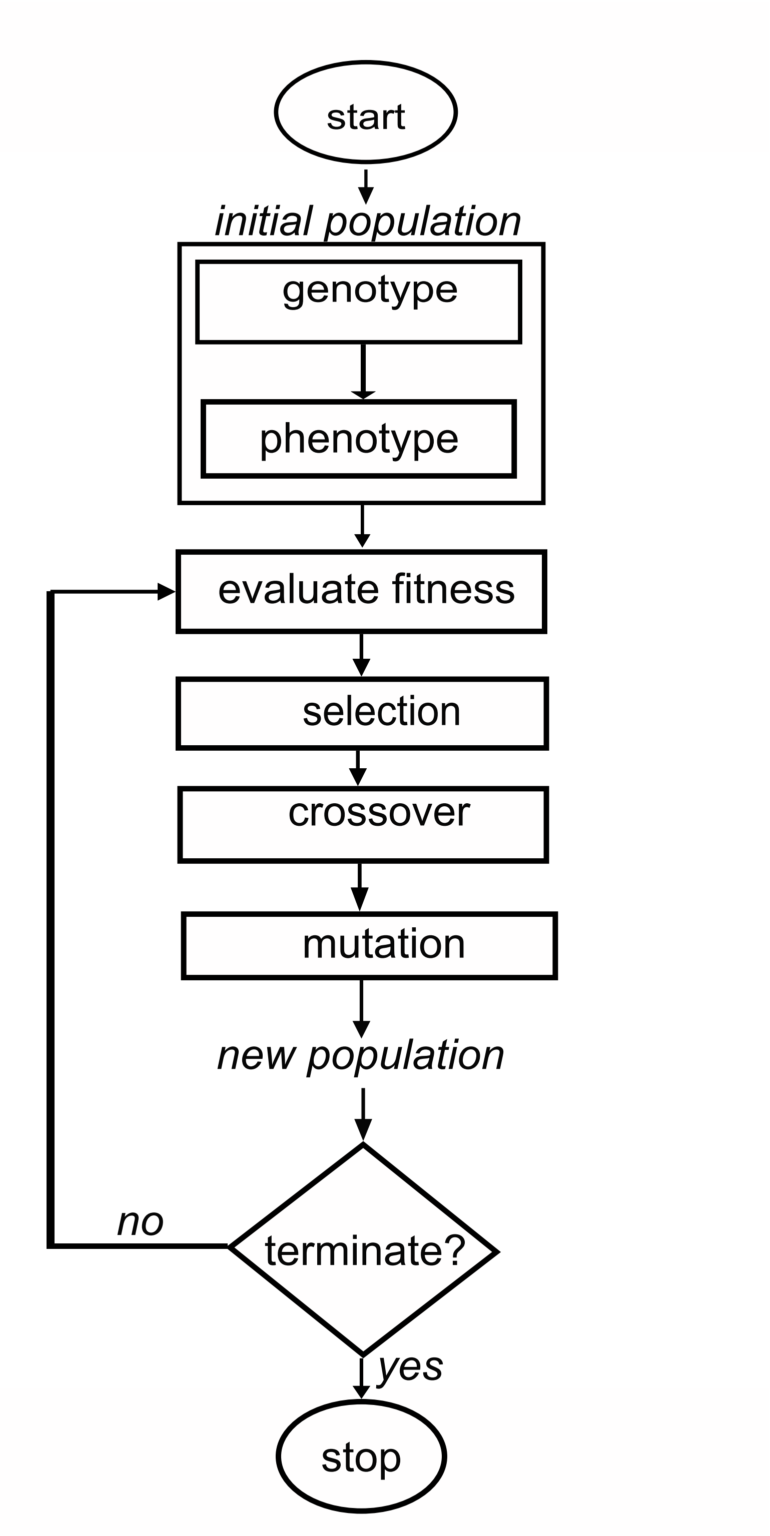

Figure 6.1: Typical steps in an evolutionary algorithm

Since the basis of EAs is derived from biology, many biological terminologies such as chromosomes, genes, genotype etc. are used in the algorithms. In the context of an EA, a chromosome represents a candidate solution, also known as an individual. Genes are parts of the chromosome which are responsible for certain traits of the individual. In this case, the set of parameters that characterise the input to the CN neuron model, listed in Section 6.1, is the chromosome and each parameter represents a gene. The configuration of the genes in the chromosome forms the genotype.

An evolutionary algorithm typically comprises of the steps shown in Fig. 6.1. The EA starts by instantiating a population of genotypes. The genes for each genotype in this initial population are selected randomly from the range of values that each gene is limited to. The genotypes are then converted into phenotypes by means of a mapping function. Next, the performance of this phenotype or individual in providing a solution to the problem is evaluated. The function which evaluates the performance of the phenotype is called the fitness function. The fitness function assigns each individual with a fitness value proportionate to its performance.

Once all the individuals have been evaluated, the best performing individuals are picked. Often, the strategy of elitist selection is used, and these individuals are copied directly to the next generation without any modifications. The rest of the individuals, for the next generation, are generated by the application of crossover and mutation operators.

Crossover is analogous to a process that happens during sexual reproduction where the genes of two parents are exchanged to create the offspring. Exchange of the genes from the parents can occur, for instance, at a single point in the genotype, at two-points, or at random locations. Fig. 6.2 (a), (b) and (c) show an example of a single-point crossover, two-point crossover and a version of uniform crossover, respectively.

Sometimes, in the offspring there are copying errors that occur when the

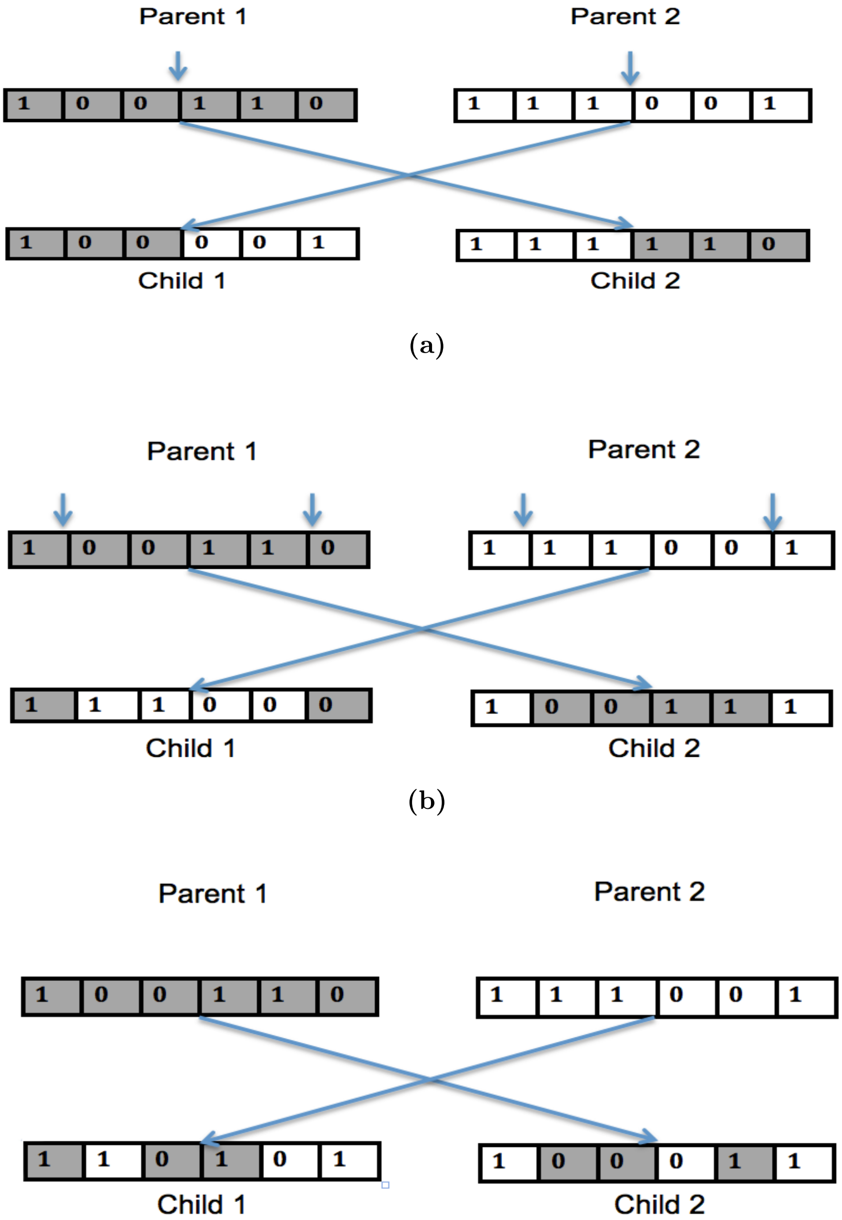

(a)

(b)

(c)

Figure 6.2: (a) single-point crossover (b) two-point crossover (c) a version of uniform crossover. The downward pointing arrows in (a) and (b) indicate crossover points.

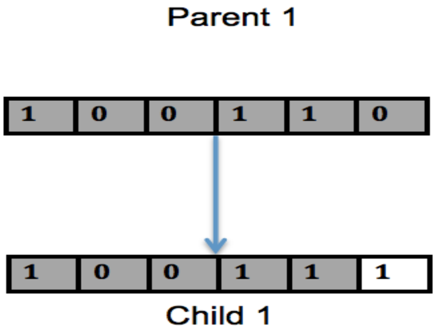

Figure 6.3: shows the process of mutation. Sometimes copying errors occur when the gene is being copied from a parent to the child. The example shows that a bit gets flipped during the copy process.

genes are copied from the parent to the child. This is called mutation. However, the probability of mutation is very small. Fig. 6.3 shows an example of mutation where a bit gets flipped when a gene is being copied from the parent to the child. Crossover and mutation operators introduce more variability in the population.

The following subsections explain how each step of the EA as shown in Fig. 6.1 was implemented in my work.

6.2.1 Initial Population

As mentioned before, the parameters that make up the genotype and their domain are defined in the list in Section 6.1. For the initial population, 100 genotypes are constructed by picking a random value, from the domain, for each parameter. However, additional care is taken so that the majority of the initial population(90%) is made of CN neurons that do not receive a bursting excitatory or inhibitory input. This restriction is put into place because it is unusual for the CN neurons to receive a bursting input from Purkinje cells or mossy fibres. The genotypes are then transformed into phenotypes with the help of the CN neuron model, see Section 6.1.

6.2.2 Fitness Function

After the transformation of the genotype into its phenotype, simulations are carried out for the CN neuron model and the output spike train is recorded. The measures *CV*, *mode ISI* and *burst-like spike ratio*, chapter 3: section 3.2, are calculated for the spike-train produced by the simulation and this output is projected onto the cluster space produced by GNG, see chapter 4, section 4.3.3. The aim of this part of the study is to produce an individual whose output datapoint is positioned in the cluster whose spiking pattern is to be replicated. For example, in order to replicate the interictal spiking pattern of a participating CN neuron, the output of the simulation should be placed into a purely participating cluster.

After the selection of the cluster relevant to the experiment, the fitness of the individual is then determined by the distance between the output of the simulation and the centre of the selected cluster. The closer the output is to the cluster centre, the higher is the fitness of the corresponding individual.

In the first two experiments, listed in 6.3.1 and 6.3.2, the cluster selected for fitness determination is a purely participating cluster, based on the interictal activity of the CN neurons. However, in the next set of experiments, listed in 6.3.3 and 6.3.4, the cluster created from the ictal counterparts of the purely participating cluster, used in 6.3.1 and 6.3.2, is selected for fitness determination.

6.2.3 Selection

Once the fitness function has assigned each individual with a fitness value, 10% of the best performing individuals are picked and copied to the next generation without any modifications. This process is known as elitism. The rest of the new population is generated by applying crossover and mutation operators on the individuals of the previous population, as explained in the following sub-sections.

6.2.4 Crossover

All the individuals from the previous population, even the best 10% already selected for the new population, are eligible for crossover. However, I want the fitter individuals to have a higher probability of getting selected for crossover than the weaker ones. This is implemented by the method of *Roulette Wheel Selection*[2].

This method is similar to the roulette wheel, used in casinos. The slots in the traditional roulette wheel are uniformly distributed and each slot has an equal probability of getting selected. However, in this case, since I want the fitter individuals to have a higher probability of getting selected, the fitter individuals are allocated more slots. The number of slots allocated to each individual is proportionate to its fitness. In this manner, by spinning the roulette wheel, two individuals or parents are selected. Additional care is taken to ensure that the parents are picked from different segments of the roulette wheel, that is, they are different individuals.

The crossover produces two offspring using a version of uniform crossover, explained with the help of Fig. 6.2(c). The number of parameters and the actual parameter to be crossed over in each case were randomly selected from the number of parameters available.

6.2.5 Mutation

The genotypes of the crossed over individuals are then subjected to mutation. The probability of mutation is set to a very low value at 2%. In the case of mutation, the parameter is varied by setting it to a new value drawn from a Gaussian probability distribution around its current value. In case of the integer-valued parameters, convergence of the Purkinje cells and mossy fibres, the nearest value in the list to the mutated value is selected.

Once the new population is formed, the whole process of fitness determination, selection, crossover and mutation is repeated in a loop until the objective of the EA is achieved.

6.3 Evolutionary Algorithm Results

6.3.1 First Run

In the first experiment, I set out to replicate the interictal firing pattern and to find the input conditions leading to output spike patterns observed in the CN neurons that take part in absence seizures. To replicate the interictal firing pattern of a participating CN neuron, I have to place the target for the output datapoint, derived by calculating the measures *CV*, *mode ISI* and *burst-like spike ratio* for the output spike train, into a purely participating cluster. So, I selected the cluster shown by black crosses(+) in Fig. 6.3.1(a), which consisted entirely of participating neurons, and I modified the fitness function to use the centre of this cluster as the target and executed the EA.

As explained in Chapter 1: Section 1.1.3, participating neurons are the CN neurons which phase-lock their spiking activity with spikes in the EEG during absence seizures. There are four purely participating clusters in the clustering result, as shown in the Fig. 4.4, and any one of them could have been chosen as the target for the EA. However, I chose the black cluster as the target cluster for this experiment because it was the most stable cluster when I performed hierarchical agglomerative clustering using different threshold values, to reduce the large number of clusters produced by GNG as explained in Chapter 4: Section 4.3.3.

When the simulations were run, I observed that the fitness value for an individual, given the same input, was slightly different for each run of the

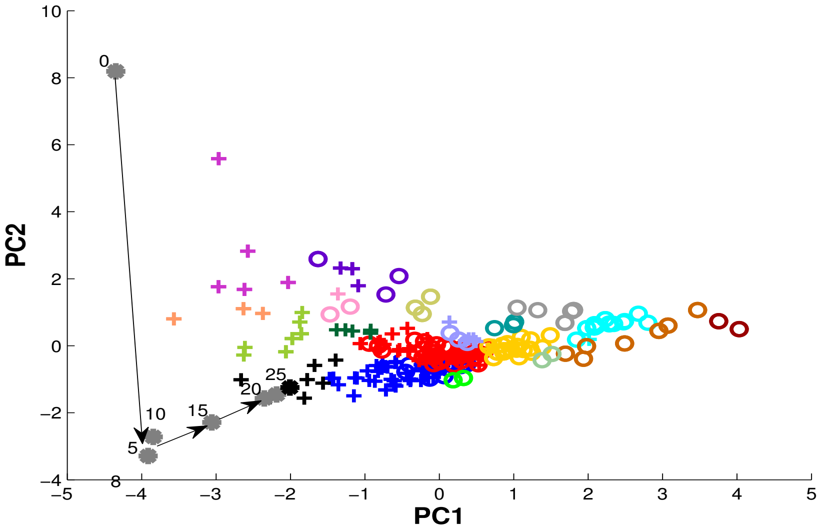

(a)

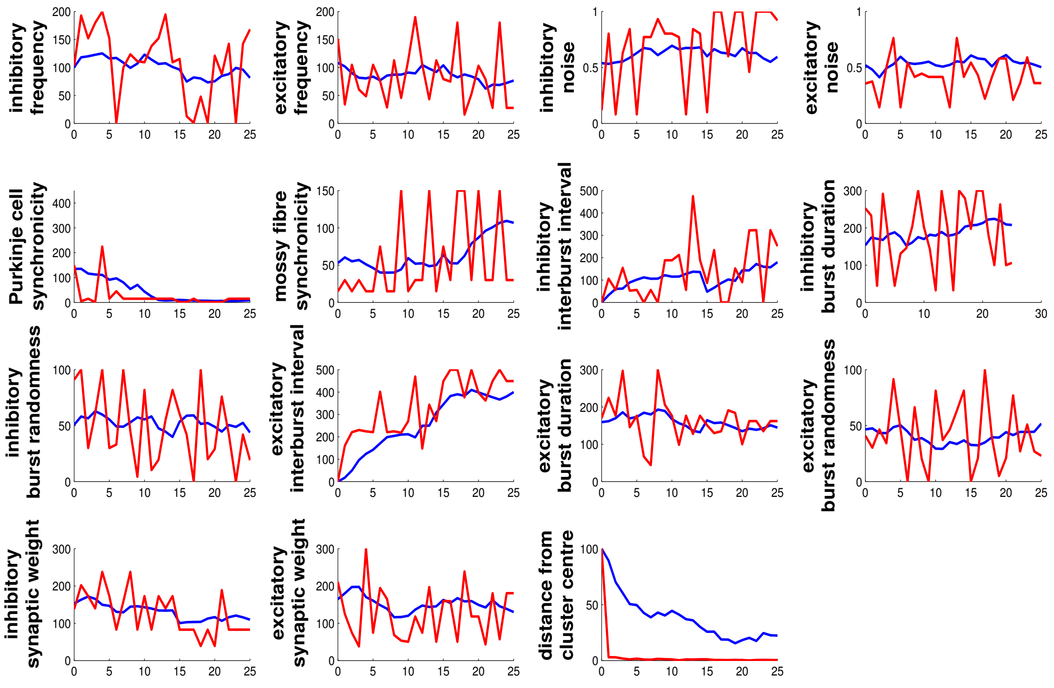

(b)

Figure 6.4: (a) shows the clusters created by the GNG algorithm on experimental data. The crosses (+) indicate participating CN neurons and circles (o) indicate non-participating neurons. The different colours indicate different clusters. The centre of the black cluster, indicated by the black dot, is chosen for the fitness function of the EA. The output of every 5th generation is shown by the grey dots and the arrows indicate the direction of their movement. (b) shows the evolution of values for each parameter that makes up the genotype. There is evolutionary pressure on the values Purkinje cell synchronicity, excitatory interburst interval and inhibitory interburst interval, indicating that the CN neurons that participate in absence seizures receive a bursting and synchronous input from Purkinje cells.

Input parameters	Normalised cross correlation
Inhibitory frequency	0.65
Excitatory frequency	0.54
Inhibitory noise	-0.48
Excitatory noise	-0.53
Purkinje cell synchronicity	0.89
Mossy fibre synchronicity	-0.45
Inhibitory interburst interval	-0.71
Inhibitory burst duration	-0.71
Inhibitory burst randomness	0.34
Excitatory interburst interval	-0.94
Excitatory burst duration	0.44
Excitatory burst randomness	0.27
Inhibitory synaptic weight	0.84
Excitatory synaptic weight	0.39

Table 6.1: shows the normalised cross correlation of each input parameter's mean time series with the mean of the time series representing the distance from cluster centre. The input parameters whose cross correlation is strong are highlighted. The results show that the input parameters Purkinje cell synchronicity, inhibitory interburst interval, inhibitory burst duration, excitatory interburst interval and inhibitory synaptic weight show a strong correlation.

simulation. This was due to the noise that was inherently present in the model. To minimise the effects of this, when determining the fitness of an individual in the EA, I ran the simulation for each individual ten times and used the average fitness value of the ten runs as the true fitness of the individual.

As shown in Fig. 6.4 (a), the output of the best individual in the first generation was located very far from the cluster centre. The best individual of every fifth generation is indicated by a grey dot in the Fig. 6.4 (a) and the movement of the output as the generations progress is indicated by the arrows. The progression of the input parameters for the best individual and the mean value of the parameter for the population, for each generation, is indicated by the red and the blue lines as shown in the subplots of Fig. 6.4(b). The average value of the parameters is considered for our analysis as it is a better indicator of the trend than the best value, which is erratic, due to the

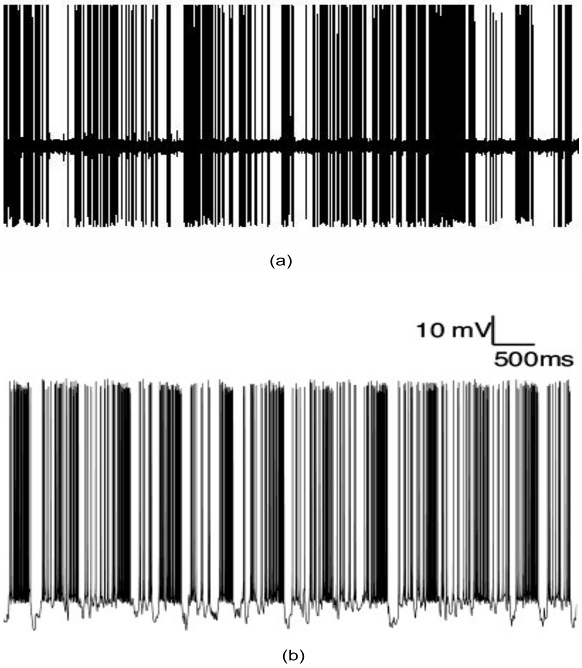

Figure 6.5: (a) interictal spiking activity recorded from a participating CN neuron (b) spike-train produced by the best individual of the last generation of the EA explained in section 6.3.1.

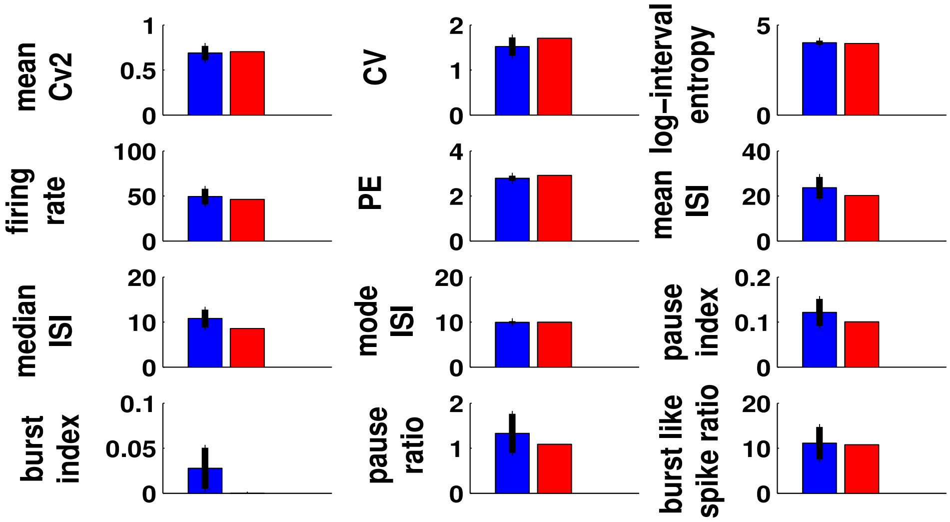

Figure 6.6: The blue bars show the mean of different measures, listed in chapter 3 section 3.2, calculated for the interictal parts of the spike-trains of participating CN neurons, shown by the black (+) in Fig. 6.4(a). The error bars show the standard deviation observed for each corresponding measure. The red bar shows the values for the same measures which were calculated for the spike-train produced by the best individual of the evolutionary algorithm explained in section 6.3.1.

inherent stochastic nature of our CN neuron model.

The results show that there is an evolutionary pressure on some of the parameters, in that there is a noticeable trend over the generations as the best individual moves closer to the centre of the desired cluster. These parameters are: Purkinje cell synchronicity, which reduces over time; excitatory interburst interval, which increases over time; and inhibitory interburst interval, which also increases.

Further, I calculated the cross correlation between the time series representing the mean of each input parameter and the time series representing the mean distance to the cluster centre as shown in table 6.1. This cross-correlation is done to verify our analysis and to bring to notice the parameters that are important, which may not be immediately evident during visual analysis of the graphs. Cross-correlation measures the similarity between two signals at different time lags. Consider two signals x and y. The cross-correlation between these two signals is calculated as shown in Eq. 6.2 where l is the time lag, μ_x, μ_y are the mean of x and y and $\sigma_x, \sigma y$ are their standard deviations respectively . The time-lag accounts for the similarity between the two signals if one of the signals is shifted in time to the left or right. In this experiment, I want to see if a change in an input parameter corresponds to a change in the fitness of the individual. So, I calculate the cross-correlation of the time-series with zero lag only.

$$r = \sum_i [(x_i - \mu_x)(y_{i+l} - \mu_y)]/\sigma_x\sigma_y \tag{6.2}$$

.The input parameters that showed a strong cross-correlation, either positive or negative, are highlighted in the table. These parameters are: Purkinje cell synchronicity, inhibitory synaptic weight, which show a strong positive cross-correlation, and excitatory interburst interval, inhibitory interburst interval and inhibitory burst duration, which show a strong negative cross-correlation. Interestingly the two highest correlations, and probably the two clearest graphical trends, are the Purkinje cell synchronicity and the excitatory interburst interval from the mossy fibre.

Also, I compared the interictal spiking pattern of a participating neuron belonging to the black cluster, which was recorded extracellularly from a participating CN neuron of a mouse, shown in Fig. 6.5(a), with the spiking pattern produced by the best individual of the last generation of the EA, as shown in Fig. 6.5(b). It can be seen that the spiking patterns are similar. Also, I compared the mean values of all the measures, described in Chapter 3, that characterise the interictal spiking pattern of the CN neurons in the black cluster, shown by the blue bars in Fig. 6.6, to the corresponding values of the spike train produced by the best individual of the last generation of the EA, shown by the red bars in Fig. 6.6. The comparison shows that the values of the experimental data and the simulation data are close. This provides additional confirmation that the interictal spiking pattern of a participating neuron has been reproduced with the help of the EA.

6.3.2 Clamping Purkinje Cell Synchronicity

Further, I wanted to explore if there are other input conditions that can place the output of the simulation in the centre of the participating cluster. Also, the possibility of a CN neuron receiving an asynchronous input is more biologically plausible. So, I stopped the parameter: Purkinje Cell synchronicity, from evolving by clamping it at 450, and I allowed the other input parameters to evolve as before during the second EA run. As in the first EA run, the black cluster is the target cluster for the purpose of fitness calculation.

As shown in Fig. 6.7(a), it is still possible to reach the centre of the participating cluster. However, when the Purkinje cell input is asynchronous, some changes in the cross-correlation between the time series representing the

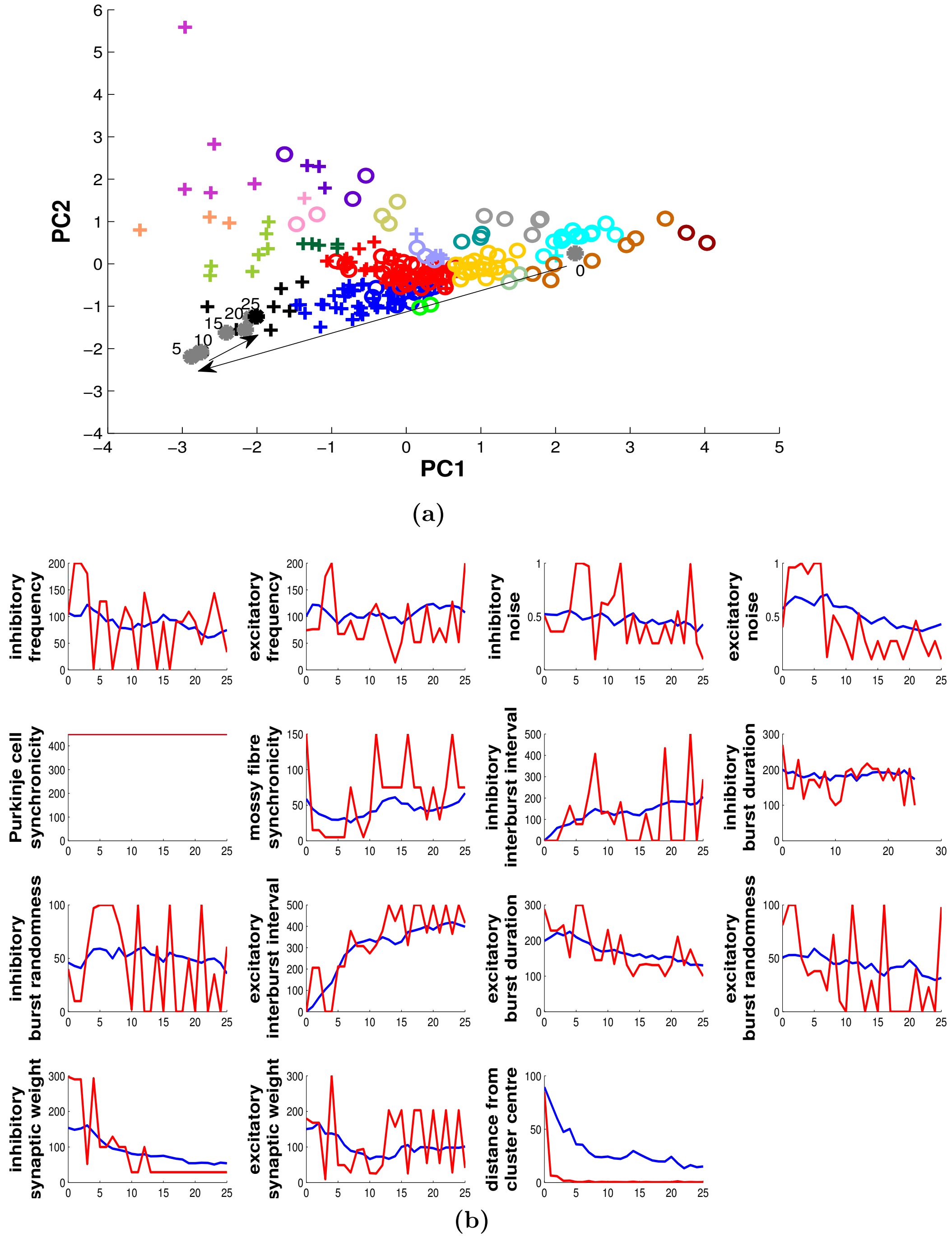

Figure 6.7: (a) shows that the output of the simulations, indicated by the grey dots, can still move to the centre of the selected participating cluster, shown by the black dot, when the Purkinje cell synchronicity is clamped at 450. (b) shows the evolution of parameters when the Purkinje cell input is clamped at its maximally asynchronous value, that is, 450. In this case, there is an evolutionary pressure on the mossy fibre input to be more synchronous along with a bursting excitatory and inhibitory input.

mean of the input parameters for each generation and the time series showing the mean of the distance from the cluster centre can be noticed as shown in the table 6.2.

The parameters: excitatory interburst interval and inhibitory synaptic weight are still important, as in the previous run, as indicated by the cross-correlation values in table 6.2. However, the parameters inhibitory interburst interval and inhibitory burst duration are no longer important. The change that was most interesting was that the mean excitatory synaptic weight, which showed a weak cross-correlation value in the first run, now showed a strong positive cross-correlation with the mean distance from the cluster centre. Again the highest correlation was with the excitatory interburst interval from the mossy fibre.

Input parameters	Normalised cross correlation
Inhibitory frequency	0.62
Excitatory frequency	0.50
Inhibitory noise	0.13
Excitatory noise	0.41
Purkinje cell synchronicity	0
Mossy fibre synchronicity	-0.17
Inhibitory interburst interval	-0.38
Inhibitory burst duration	0.57
Inhibitory burst randomness	-0.65
Excitatory interburst interval	-0.94
Excitatory burst duration	0.67
Excitatory burst randomness	0.52
Inhibitory synaptic weight	0.78
Excitatory synaptic weight	0.74

Table 6.2: shows the normalised cross correlation of each input parameter's mean time series with the mean of the time series representing the distance from the cluster centre. The input parameters whose cross correlation is strong are highlighted. When the Purkinje cell synchronicity is clamped, the input parameters excitatory interburst interval, inhibitory synaptic weight and excitatory synaptic weight show a strong correlation (one negative and the other two positive).

6.3.3 Input Conditions for Ictal Spiking Activity

In the previous experiments, I explored the input conditions required for the CN neuron model to produce a spiking pattern similar to the interictal activity in CN neurons that participate in absence seizures. The next step was to investigate the changes that occur in the input conditions when the same CN neuron changes its spiking behaviour from an interictal to an ictal spiking pattern.

The initial position for this EA is the centre of the black cluster. So, I instantiated the genotypes of the first generation of the EA with the genes of the best individual of the first run of the EA, shown in Fig. 6.4. Then, I plotted the ictal counterparts of the black interictal cluster onto the same cluster space, shown by cyan squares in the Fig. 6.8(a). The distance to the centre of this cluster, shown by the cyan asterisk(*) in Fig. 6.8(a), was used to determine the fitness of the individuals. The objective of the EA was to move the output of the simulation from the interictal cluster centre to the ictal cluster centre.

When the EA was run for some generations, the output of the simulation, shown with the help of grey dots in Fig. 6.8(a), indeed showed movement from the interictal cluster centre to the ictal cluster centre. The evolution of the parameters is shown by the subplots in Fig. 6.8(b). I expected to see a drastic change in some of the parameters that characterise the input, when the spiking pattern changed from interictal to ictal spiking. Surprisingly, this was not the case; a small change in the parameters was sufficient to change the interictal spiking to an ictal spiking pattern. As before, I also calculated the cross-correlation between the time series showing the mean of the input parameters and the time series showing the mean distance from the cluster centre. Only the excitatory interburst interval showed a good cross-correlation value as shown in the table 6.3.

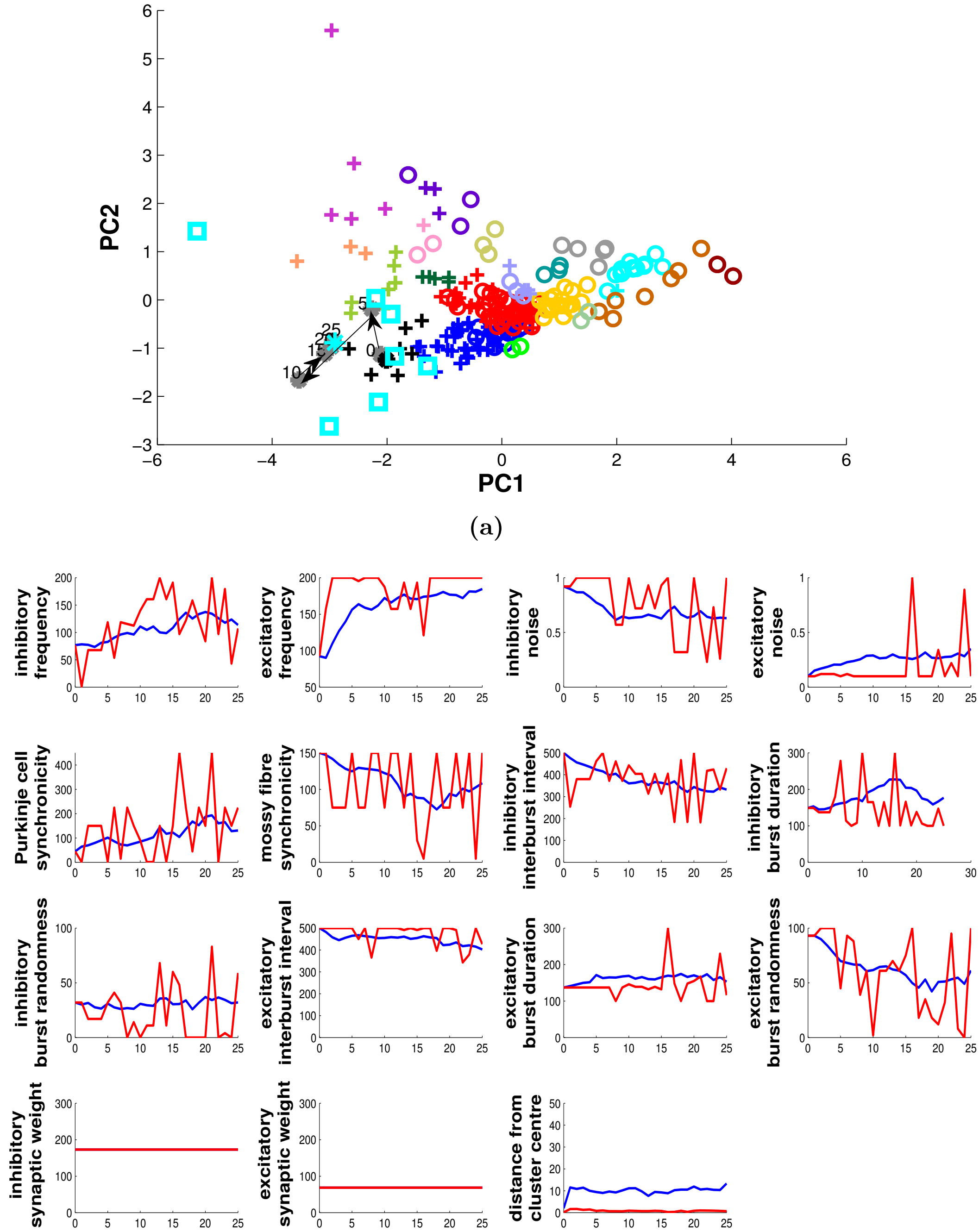

(a)

(b)

Figure 6.8: (a) the cyan squares represent the ictal counterparts of the CN neurons in the black cluster. The cyan asterisk (*) is the centre of this ictal cluster and also the target for fitness calculation. The grey dots show the position of the output datapoint for every 5th generation. The arrows show the progression of the output datapoint. (b) shows the evolution of parameters for 25 generations. I expected a drastic change in the parameters when the output moves from the interictal cluster centre to the ictal cluster centre. However, the plots show that this is not the case and the changes that occur in the parameters are subtle.

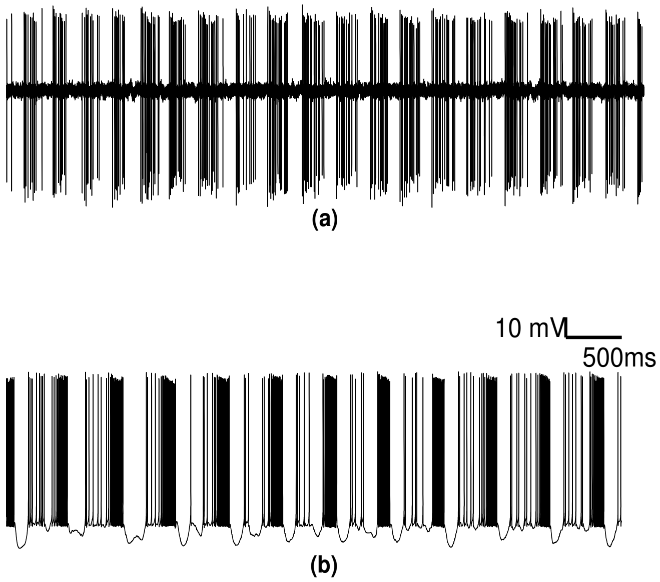

Figure 6.9: (a) ictal spiking pattern recorded extracellularly from a participating CN neuron. (b) spike-train produced by the best individual of the last generation of the EA explained in section 6.3.3.

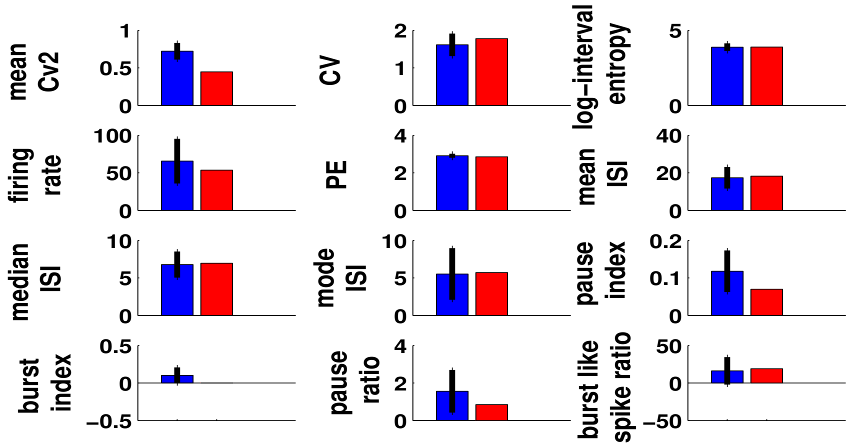

Figure 6.10: The blue bars show the mean of different measures, listed in chapter 3 section 3.2, calculated on the ictal parts of the spike-trains of participating CN neurons, shown by the cyan (□) in Fig. 6.8(a). The error bars show the standard deviation observed for each corresponding measure. The red bar shows the values for the same measures which were calculated on the spike-train produced by the best individual of the evolutionary algorithm explained in sub section 6.3.3.

Input parameters	Normalised cross correlation
Inhibitory frequency	0.31
Excitatory frequency	0.35
Inhibitory noise	-0.32
Excitatory noise	0.49
Purkinje cell synchronicity	0.35
Mossy fibre synchronicity	-0.21
Inhibitory interburst interval	-0.43
Inhibitory burst duration	0.02
Inhibitory burst randomness	0.01
Excitatory interburst interval	-0.64
Excitatory burst duration	0.28
Excitatory burst randomness	-0.29
Inhibitory synaptic weight	0
Excitatory synaptic weight	0

Table 6.3: shows the normalised cross correlation of each input parameter's mean time series with the mean of the time series representing the distance from cluster centre. The input parameters whose cross correlation is strong are highlighted. In this case, only the excitatory interburst interval showed a moderate correlation.

As before, I also assessed whether I have replicated the ictal spike train pattern by comparing the ictal spike trains recorded from a participating CN neurons from a mouse, shown in Fig. 6.9(a) with the spike train produced by the best individual of the last generation of the EA, shown in Fig. 6.9(b). We can see that both spike trains, the spike train recorded from the tottering mice and the one derived from our simulation, show repeated bursts. The actual values for the measures that I use to characterise the spiking activity of a CN neuron, as listed in Chapter 3, were also compared for these spike trains as shown in Fig. 6.10, where the blue bars represent the experimental data and the red bars represent the simulation data. The comparison shows that the values for the measures in both cases are close.

6.3.4 Blocking the Purkinje Cell Input

Next, it was interesting to investigate if it is possible to prevent the CN neurons in the black interictal cluster from participating in the absence seizures. The EA was set up similarly to the previous experiment, that is, the fitness function optimised input conditions so that the output, when projected onto the cluster space, would move closer to the ictal cluster centre, shown by the cyan asterisk (*) in Fig. 6.11. Again, the EA was instantiated with the genes of the best individual of the last generation of the first run, so that the output of the simulation was placed near the centre of the interictal cluster.

The only difference in the setup of this EA when compared to the previous experiment was that the Purkinje cell input to the CN neuron model was blocked by forcing the inhibitory synaptic weight to zero. This gave a very interesting result. Even after the EA was run for the same number of generations as the previous EA run had used to move the best individual to the centre of the ictal cluster, the output of the simulations in this new run never reached the ictal cluster centre but moved to a different interictal cluster. Importantly, this suggests that by blocking the Purkinje cell input, perhaps the CN neurons, which have been shown likely to participate in seizures, could be stopped from participating.

6.4 Chapter Conclusions

I found through the execution of the EA, as shown in the subsection 6.3.1, that the input parameters, Purkinje cell synchronicity, inhibitory and excitatory interburst interval, inhibitory burst duration and inhibitory synaptic weight play a key role in producing a spiking pattern similar to the interictal activity of participating neurons. In plain words, the CN neuron should receive a synchronous and bursting input from Purkinje cells and a bursting input from

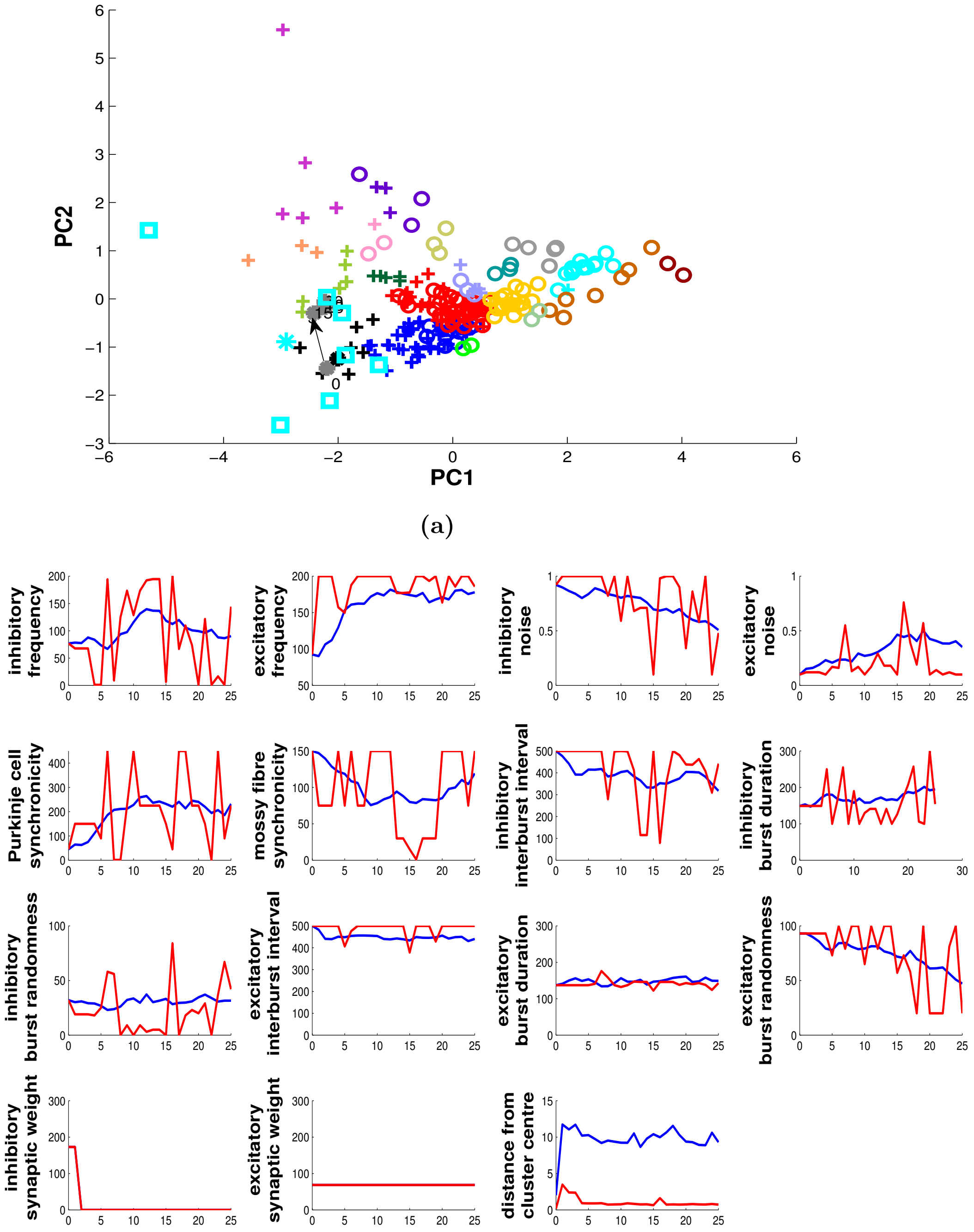

(a)

(b)

Figure 6.11: (a) shows the movement of the output of the simulation when the Purkinje Cell input is blocked by forcing the inhibitory synaptic weight to zero. (b) shows the evolution of input parameters for 25 generations. It can be seen both from (a) and the distance from cluster centre subplot in (b) that the output datapoint never reaches the cluster centre if the Purkinje cell input to the CN neuron is blocked.

mossy fibres.

When the Purkinje cell input is forced to be asynchronous, as this is more biologically plausible, the mean of the input parameters, excitatory interburst interval, inhibitory synaptic weight and excitatory synaptic weight show a strong cross-correlation (negative for excitatory interburst interval and positive for the other two) with the mean distance from the cluster centre.

A small change in the input conditions of these CN neurons is sufficient to change their firing pattern from interictal to ictal. Interestingly, these CN neurons can be stopped from participating in the absence seizures by blocking the input from Purkinje cells. Perhaps this is something that can be investigated biologically on real mice in the laboratory.

Chapter 7

Conclusion

Contents

The main objective of this research was to demonstrate how machine learning and computational modelling can be used to analyse problems in neuroscience. To do so, I have employed a variety of techniques such as spike train analysis, clustering, regression analysis, an evolutionary algorithm and computational modelling to investigate the pathology of mutant mice which exhibit absence seizures. The most interesting aspect of this research is that it combines experimental data, extracted from awake head-restrained mice, and theoretical work to find solutions to the problem at hand. At the beginning of the research I planned to find answers to the following questions:

- What are the properties of CN neurons that participate in absence seizures?
- What are the input conditions present in the CN neurons that are mostly likely to participate in seizures?
- What changes in the input conditions are required to change the output spiking pattern of a Participating CN neuron from an interictal spiking pattern to an ictal spiking pattern?

To answer these questions, I used a combination of machine learning techniques and computational modelling. In fact, I have shown that many interesting features of neuronal data can be found using both supervised and unsupervised data analysis techniques. Moreover, I have shown that the parameter space of model neurons can be successfully explored using evolutionary algorithms.

I have presented two major contributions to knowledge: the first is the result of my investigation into how interictal spiking activity can characterise participating and non-participating CN neurons. I used a clustering method, Growing Neural Gas (GNG), that discovered properties of the type of CN neuron that are more likely to participate in absence seizures. Interestingly, these participating CN neurons were located primarily in the lateral and interpositus region of the cerebellum. Secondly, I used computerised optimisation (an Evolutionary Algorithm) to discover the most important factors in the input conditions present during the interictal periods of the participating CN neurons.

Specifically I discovered that :

- There were five key input parameters, Purkinje cell synchronicity, inhibitory interburst interval, inhibitory burst duration, excitatory interburst interval and inhibitory synaptic weight, that resulted in the simulation of the spiking activity giving an activity similar to that observed in the interictal periods of real participating CN neurons. In other words, a participating CN neuron receives a synchronous and bursting input from the Purkinje cells and a bursting input from the mossy fibre with long intervals (approx. 500ms) in between bursts during the interictal periods.

- It is possible to simulate the interictal activity of participating CN neurons when the input from the Purkinje cell is not synchronous. In this case, the input parameters excitatory interburst interval, inhibitory synaptic weight and excitatory synaptic weight are the key parameters which affect the CN neuron's participation in absence seizures. The most interesting point to note in this experiment is that when the Purkinje cell input is asynchronous, the excitatory input to the CN neuron should be reduced (supported by the decrease in excitatory synaptic weight) to achieve the desired results.

- Instead of a dramatic change in input conditions of the participating CN neurons, a small change is sufficient to change the output from an interictal spiking pattern to an ictal spiking pattern.
- It is possible to stop a participating CN neuron from participating in absence seizures by blocking the Purkinje cell input to the CN neuron.
- It is possible to predict the *FFT based Z-score*, a measure that quantifies the phase-locking behaviour of the CN neuron's spikes with the spikes of the SWDs in the EEG during absence seizures as explained in Chapter 3 (Section 3.1), from the interictal activity of the CN neuron.

7.1 Future Work

There are many possible extensions to this research such as:

- I discovered that by blocking the Purkinje cell input to the CN neuron, we can prevent the Participating CN neuron from taking part in absence seizures. This result can be experimentally tested.
- In this research, I investigate the input conditions required to simulate the interictal activity of a participating CN neuron using a CN neuron model which does not have any P/Q channel mutations related to absence seizures. The P/Q type channel mutations have been observed in

Purkinje cells terminals of the tottering mice and there is evidence that these P/Q type channels are also present in the CN neuron [61]. This experiment can be further extended to study the effect of P/Q type channel mutations in the CN neuron by introducing these additional channels in the CN neuron model.

- Also, the inhibitory input to the model can be changed so that the input from a Purkinje cell incorporates both simple and complex spikes. At present, the CN neuron model receives only simple spikes from Purkinje Cells. From this experiment, we can determine if the complex spikes are instrumental to the input synchronisation from the Purkinje cell and hence the CN neuron's participation in absence seizures.
- We could also extend the research to investigate the effect of the CN neuron input on neural activity in the thalamus, both in the absence and presence of epileptic seizures.

7.2 List of Publications

During the course of my PhD, I presented my work at several conferences and I was also able to co-author a journal paper with our collaborators in Rotterdam. Here is the list of the conference papers, articles and abstracts that were published. The first two publications are not related to the work discussed in this thesis, but are based on the work completed as part of my Master's degree. The full versions of the publications can be found in the appendix.

- Alva, P., De Sousa, G., Torben-Nielsen, B., Davey, N., Adams, R. and Steuber, V. (2012). Comparing developmental approaches to generate neuronal morphologies for pattern recognition. Front. Comput. Neurosci. doi: 10.3389/conf.fncom.2012.55.00212

- Alva, P., De Sousa, G., Torben-Nielsen, B., Maex, R., Davey, N., Adams, R. and Steuber, V. (2013). Evolution of Dendritic Morphologies Using Deterministic and Nondeterministic Genotype to Phenotype Mapping. Artificial Neural Networks and Machine Learning. ICANN 2013, 8131: 319–326. doi:10.1007/978-3-642-40728-4_40

- Alva, P., Kros, L., Maex, R., De Zeeuw, C. I., Adams, R., Davey, N., Steuber, V., Hoebeek, F. E. (2013). A potential role for the cerebellar nuclei in absence seizures. BMC Neuroscience, 14(Suppl 1), P170. doi:10.1186/1471-2202-14-S1-P170

- Alva, P., Kros, L., Eelkman Rooda, O.H.J., De Zeeuw, C. I., Adams, R., Davey, N., Hoebeek, F. E., Steuber, V. (2014). Combining machine learning and simulations of a morphologically realistic model to study modulation of neuronal activity in cerebellar nuclei during absence epilepsy. BMC Neuroscience, 15(Suppl 1), P39. doi:10.1186/1471-2202-15-S1-P39

- Kros, L., Eelkman Rooda, O. H. J., Spanke, J. K., Alva, P., van Dongen, M. N., Karapatis, A., Tolner, E. A., Strydis, C., Davey, N., Winkelman, B. H. J., Negrello, M., Serdijn, W. A., Steuber, V., van den Maagdenberg, A. M. J. M., De Zeeuw, C. I. and Hoebeek, F. E. Absence seizures stopped by closed-loop activation of cerebellar output. FENS Forum Abstr 2014. OpenURL

- Kros, L., Eelkman Rooda, O. H. J., Spanke, J. K., Alva, P., van Dongen, M. N., Karapatis, A., Tolner, E. A., Strydis, C., Davey, N., Winkelman, B. H. J., Negrello, M., Serdijn, W. A., Steuber, V., van den Maagdenberg, A. M. J. M., De Zeeuw, C. I. and Hoebeek, F. E. (2015), Cerebellar output controls generalized spike-and-wave discharge occurrence. Ann Neurol., 77: 1027-1049. doi: 10.1002/ana.24399

- Alva, P., Kros, L., Eelkman Rooda, O.H.J., De Zeeuw, C. I., Adams, R., Davey, N., Hoebeek, F. E., Steuber, V. (2015). Optimization of input parameters to a CN neuron model to simulate its activity during and between epileptic absence seizures.[pending publication]

Bibliography

[1] P. Ashrafi, G. Moss, S. Wilkinson, N. Davey, and Y. Sun. The application of machine learning to the modelling of percutaneous absorption: An overview and guide. *SAR and QSAR in Environmental Research*, 26(3):181–204, 2015. (Cited on pages 71, 72, 73 and 78.)

[2] J. E. Baker. Reducing bias and inefficiency in the selection algorithm. In *Proceedings of the Second International Conference on Genetic Algorithms and their Application (Hillsdale, New Jersey: L. Erlbaum Associates)*, pages 14–21, 1987. (Cited on page 100.)

[3] C. Bandt and B. Pompe. Permutation entropy: A natural complexity measure for time series. *Physical Review Letters*, 88(17):174102, 2002. (Cited on page 42.)

[4] A. Berényi, M. Belluscio, D. Mao, and G. Buzsàki. Closed-loop control of epilepsy by transcranial electrical stimulation. *Science*, 337:735–737, 2012. (Cited on page 19.)

[5] A. Berg, S. Berkovic, M. Brodie, J. Buchhalter, J. Cross, W. van Emde Boas, and J. Engel. Revised terminology and concepts for organization of seizures and epilepsies:report of the ilae commision on classification and terminology,2005-2009. *Epilepsia*, 51(4):676–685, 2010. (Cited on page 16.)

[6] U. Bhalla and J. Bower. Exploring parameter space in detailed single neuron models:simulations of the mitral and granule cells of the olfactory bulb. *J Neurophysiol*, 69(6):1948–1965, 1993. (Cited on page 4.)

[7] J. Bower and D. Beeman. *The Book of Genesis:Exploring realistic neural models with the GEneral NEural SImulationSystem.* New York: Springer, 1998. (Cited on page 5.)

[8] N. Brunel and M. Van Rossum. Lapicque's 1907 paper: from frogs to integrate-and-fire. *Biol. Cynern.*, 97(5-6):337–339, 2007. (Cited on page 5.)

[9] V. Chan-Palay. *Cerebellar dentate nucleus: organization, cytology and transmitters.* Berlin: Springer-Verlag., 1977. (Cited on page 27.)

[10] S. Chen and D. Hillman. Colocalization of neurotransmitters in the deep cerebellar nuclei. *J Neurocytol*, 22:81–91, 1993. (Cited on page 27.)

[11] D. Chong and L. Hirsch. Which eeg patterns warrant treatment in the critically ill? reviewing the evidence for treatment of periodic epileptiform discharges and related patterns. *J Clin. Neurophysiol.*, 22(2):79 – 91, Apr 2005. (Cited on page 4.)

[12] V. Crunelli and N. Leresche. A role for gabab receptor in excitation and inhibition of thalamocortical cells. *Trends Neurosci.*, 14(16-21), 1991. (Cited on pages 6, 18 and 33.)

[13] V. Crunelli and N. Leresche. Childhood absence epilepsy: Genes, channels, neurons and networks. *Nature Reviews Neuroscience*, 3:371–382, May 2002. (Cited on page 16.)

[14] L. Danober, C. Deransart, A. Depaulis, M. Vergnes, and C. Marescaux. Pathophysiological mechanisms of genetic absence epilepsy in the rat. *Progress in Neurobiology*, 55:27–57, May 1998. (Cited on pages ii, 6, 15, 18 and 33.)

[15] C. R. Darwin. *The origin of species.* New York:P.F. Collier & Son, 1909–14. (Cited on page 94.)

[16] E. De Schutter and J. Bower. An active membrane model of the cerebellar purkinje cell. i. simulation of current clamps in slice. *J Neurophysiol*, 71(1):375–400, 1994. (Cited on page 5.)

[17] E. De Schutter and V. Steuber. Patterns and pauses in purkinje cell simple spike trains: experiments, modeling and theory. *Neuroscience*, 162(3), 2009. (Cited on page 6.)

[18] A. Destexhe. Spike-and-wave oscillations, 2007. (Cited on page 7.)

[19] G. V. Dijck, M. M. Van Hulle, S. A. Heiney, P. M. Blazquez, H. Meng, D. E. Angelaki, A. Arenz, T. W. Margrie, A. Mostofi, S. Edgley, F. Bengtsson, C.-F. Ekerot, H. Jörntell, J. W. Dalley, and T. Holtzman. Probabilistic identification of cerebellar cortical neurones across species. *PLoS ONE*, 8(3):e57669, 2013. (Cited on pages 3 and 41.)

[20] R. Fisher. Fisher's iris dataset. (Cited on page 70.)

[21] C. F. Fletcher, C. M. Lutz, T. O'Sullivan, J. D. Shaughnessy Jr., R. Hawkes, W. N. Frankel, N. G. Copeland, and N. A. Jenkins. Absence epilepsy in tottering mutant mice is associated with calcium channel defects. *Cell*, 87(4):607 – 617, 1996. (Cited on page 8.)

[22] W. Foster, L. Ungar, and J. Schwaber. Significance of conductances in hodgkin-huxley models. *J Neurophysiol*, 70(6):2502–2518, 1993. (Cited on page 4.)

[23] B. Fredette and E. Mugnaini. The gabaergic cerebello-olivary projection in the rat. *Anat Embryol*, 184:225–243, 1991. (Cited on page 27.)

[24] B. Fritzke. A growing neural gas network learns topologies. In G. Tesauro, D. Touretzky, and T. Leen, editors, *Advances in Neural Information Processing Systems 7*, pages 625–632. MIT Press, 1995. (Cited on pages 55, 56, 57 and 58.)

[25] A. Gardner, A. Krieger, G. Vachtsevanos, and B. Litt. One-class novelty detection for seizure analysis from intracranial eeg. *Journal of Machine Learning Research*, 7:1025 – 1044, 2006. (Cited on page 4.)

[26] I. Gligorijević, M. Welkenhuysen, D. Prodanov, W. Eberle, B. Nuttin, C. Bartic, and S. Van Huffel. Statistical analysis of neural spike trains for evaluation of functional differences in brain activity. In *Proceedings Of Biosignal*, 2010. (Cited on pages 42 and 43.)

[27] P. Gloor, M. Avoli, and G. Kostopoulos. *Thalamo-cortical relationships in generalized epilepsy with bilaterally synchronous spike-and-wave discharge*, pages 190–212. BirkhaÈuser Boston Inc.: Boston., 1990. (Cited on page 18.)

[28] M. Hines and N. Carnevale. The neuron simulation environment. *Neural Comput*, 9(6):1179–209, 1997. (Cited on page 5.)

[29] A. Hodgkin and A. Huxley. The components of membrane conductance in the giant axon of loligo. *J of Physiol*, 116:473–496, 1952. (Cited on page 5.)

[30] A. Hodgkin and A. Huxley. Currents carried by sodium and potassium ions through the membrane of the giant axon of loligo. *J of Physiol*, 116:449–472, 1952. (Cited on page 5.)

[31] A. Hodgkin and A. Huxley. The dual effect of membrane potential on sodium conductance in the giant axon of loligo. *J of Physiol*, 116:497–506, 1952. (Cited on page 5.)

[32] A. Hodgkin and A. Huxley. A quantitative description of membrane current and its application to conduction and excitation in nerve. *J of Physiol*, 117:500–544, 1952. (Cited on page 5.)

[33] A. Hodgkin, A. Huxley, and B. Katz. Measurement of current–voltage relations in the membrane of the giant axon of loligo. *J of Physiol*, 116:424–448, 1952. (Cited on page 5.)

[34] F. Hoebeek, S. Khosrovani, L. Witter, and C. I. De Zeeuw. Purkinje cell input to cerebellar nuclei in tottering: Ultrastructure and physiology. *The Cerebellum*, 7(4):547–558, 2008. (Cited on page 17.)

[35] G. Holt, W. Softky, C. Koch, and R. Dougas. Comparison of discharge variability in vitro and in vivo in cat visual cortex neurons. *Journal of Neurophysiology*, 75(5):1806–1814, May 1996. (Cited on page 41.)

[36] Q. Huys and L. Paninski. Smoothing of, and parameter estimation from, noisy biophysical recordings. *Plos Computational Biology*, 2009. (Cited on page 4.)

[37] M. Inoue, J. Duysens, J. M. H. Vossen, and A. M. L. Coenen. Thalamic multiple-unit activity underlying spike-wave discharges in anesthetized rats. *Brain Res.*, 612:35–40, 1993. (Cited on page 17.)

[38] A. K. Jain, M. N. Murty, and P. J. Flynn. Data clustering: A review. *ACM Comput. Surv.*, 31(3):264–323, sep 1999. (Cited on pages 50, 51, 52, 53 and 60.)

[39] A. Jouvenceau, L. H. Eunson, A. Spauschus, V. Ramesh, S. M. Zuberi, D. M. Kullmann, and M. G. Hanna. Human epilepsy associated with dysfunction of the brain p/q-type calcium channel. *The Lancet*, 358:801–807, September 2001. (Cited on page 16.)

[40] E. R. Kandel, J. H. Schwartz, and T. M. Jessell. *Principles of Neural Science*. New York : McGraw-Hill, Health Professions Division, ©2000., 2000. (Cited on pages 19, 22, 23 and 25.)

[41] L. Kros, O. H. J. Eelkman Rooda, J. K. Spanke, P. Alva, M. N. van Dongen, A. Karapatis, E. A. Tolner, C. Strydis, N. Davey, B. H. J. Winkelman, M. Negrello, W. A. Serdijn, V. Steuber, A. M. J. M. van den Maagdenberg, C. I. De Zeeuw, and F. E. Hoebeek. Cerebellar output controls generalized spike-and-wave discharge occurrence. *Ann Neurol.*, 77(1027-1049), 2015. (Cited on pages ii, 9 and 35.)

[42] J. Luthman. *Computational modelling of information processing in deep cerebellar nucleus neurons.* PhD thesis, University of Hertfordshire, 2012. (Cited on pages 21 and 24.)

[43] J. Luthman, F. E. Hoebeek, R. Maex, N. Davey, R. Adams, C. I. De Zeeuw, and V. Steuber. Std-dependent and independent encoding of input irregularity as spike rate in a computational model of a cerebellar nucleus neuron. *Cerebellum*, 10:667–682, 2011. (Cited on pages 31, 33 and 93.)

[44] A. Lüttjohann and G. van Luijtelaar. Dynamics of networks during absence seizure's on- and offset in rodents and man. *Front. Physiol.*, 2015. (Cited on pages ii and 15.)

[45] C. D. Manning, P. Raghavan, and H. Schütze. *Introduction to Information Retrieval.* Cambridge University Press, 2008. (Cited on page 61.)

[46] C. Marescaux, M. Vergnes, and A. Depaulis. Genetic absence epilepsy in rats from strasbourg–a review. *J Neural Transm Suppl*, 35:37–69, 1992. (Cited on page 17.)

[47] T. Martinetz. Competitive hebbian learning rule forms perfectly topology preserving maps. In *ICANN'93*, pages 427–434. Springer London, 1993. (Cited on pages 56 and 57.)

[48] T. Martinetz and K. Schulten. *A" neural-gas" network learns topologies.* University of Illinois at Urbana-Champaign, 1991. (Cited on pages 55 and 56.)

[49] J. Montes, E. Gomez, A. Merchan-Perez, J. DeFelipe, and J.-M. Pena. A machine learning method for the prediction of receptor activation in the simulation of synapses. *PLoS ONE*, 2013. (Cited on page 4.)

[50] K.-R. Muller, M. Krauledat, G. Dornhege, S. Jahnichen, G. Curio, and B. Blankertz. A note on the berlin brain-computer interface. In *Human Interaction with Machines: Proceedings of the 6th International Workshop held at the Shanghai JiaoTong University*, 2005. (Cited on page 4.)

[51] F. Nadim, O. Olsen, E. De Schutter, and R. Calabrese. Modeling the leech heartbeat elemental oscillator. i. interaction of intrinsic and synaptic currents. *J Comput Neurosci*, 2, 215-235. (Cited on page 4.)

[52] V. Nimmrich and G. Gross. P/q-type calcium channel modulators. *British Journal of Pharmacology*, 167(4):741–759, 2012. (Cited on page 17.)

[53] J. Noebels and R. Sidman. Inherited epilepsy: spike-wave and focal motor seizures in the mutant mouse tottering. *Science*, 204(4399):1344–1336, 1979. (Cited on page 17.)

[54] A. Okabe, B. Boots, K. Sugihara, and S. Nok Chiu. *Spatial Tessellations: Concepts and Applications of Voronoi Diagrams.* Wiley, 2000. (Cited on page 57.)

[55] A. J. Onwuegbuzie, L. Daniel, and N. L. Leech. Pearson product-moment correlation coefficient. encyclopedia of measurement and statistics. sage publications, inc. correlation coefficient. encyclopedia of measurement and statistics. sage publications, inc. (Cited on page 87.)

[56] M. Palkovits, E. Mezey, J. Hamori, and J. Szentagothai. Quantitative histological analysis of the cerebellar nuclei in the cat. i. numerical data on cells and on synapses. *Experimental Brain Research*, 28(1-2):189–209, 1977. (Cited on page 24.)

[57] J. Paz, T. Davidson, and E. Frechette. Closed-loop optogenetic control of thalamus as a tool for interrupting seizures after cortical injury. *Nat Neurosci*, 16:64–70, 2013. (Cited on page 19.)

[58] A. L. Person and I. M. Raman. Purkinje neuron synchrony elicits time-locked spiking in the cerebellar nuclei. *Nature*, 481(7382):502–505, 01 2012. (Cited on page 24.)

[59] C. E. Rasmussen and C. Williams. *Gaussian Processes for Machine Learning*. The MIT Press, 2006. (Cited on pages 75, 76, 77 and 78.)

[60] F. Rezwan, Y. Sun, N. Davey, R. Adams, A. G. Rust, and M. Robinson. Using randomised vectors in transcription factor binding site predictions. In *The Ninth International Conference on Machine Learning and Applications*, 2010. (Cited on pages 81, 82 and 83.)

[61] K. Sawada, H. Sakata-Haga, M. Ando, N. Takeda, and Y. Fukui. An increased expression of ca(2+) channel alpha(1a) subunit immunoreactivity in deep cerebellar neurons of rolling mouse nagoya. *Neuroscience Letters*, 316(2):87–90, 2001. (Cited on page 120.)

[62] A. Selim, M. Wahed, and Y. Kadah. Machine learning methodologies in brain-computer interface systems machine learning methodologies in brain-computer interface systems machine learning methodologies in brain-computer interface systems machine learning methodologies in brain-computer interface systems. In *Biomedical Engineering Conference*, 2008. (Cited on page 4.)

[63] R. Sokal and P. Sneath. *Principles of numerical taxonomy.* Freeman, San Francisco-London, 1963. (Cited on page 52.)

[64] V. Steuber, E. De Schutter, and D. Jaeger. Passive models of the neurons in the deep cerebellar nuclei: the effect of reconstruction errors. *Neurocomputing*, 58-60:563–568, 2004. (Cited on page 31.)

[65] V. Steuber, W. Mittwann, F. E. Hoebeek, R. A. Silver, C. I. De Zeeuw, M. Hausser, and E. De Schutter. Cerebellar ltd and pattern recognition by purkinje cells. *Neuron*, 54(1):121–36, Apr 2007. (Cited on page 6.)

[66] V. Steuber, N. W. Schultheiss, R. A. Silver, E. De Schutter, and D. Jaeger. Determinants of synaptic integration and heterogeneity in rebound firing explored with data-driven models of deep cerebellar nucleus cells. *Journal of Computational Neuroscience*, 30(3):633–658, 2011. (Cited on pages ii, 5, 31, 32 and 33.)

[67] S. Sudhakar, B. Torben-Nielsen, and E. De Schutter. Cerebellar nuclear neurons use time and rate coding to transmit purkinje neuron pauses. *PLoS Computational Biology*, 11, 2015. (Cited on page 6.)

[68] O. Temkin. *The Falling Sickness.* Johns Hopkins University Press, 1971. (Cited on page 6.)

[69] M. Uusisaari and T. Knöpfel. Functional classification of neurons in the mouse lateral cerebellar nuclei. *The Cerebellum*, 10(4):637–646, 2007. (Cited on pages 27, 29 and 30.)

[70] M. Uusisaari, K. Obata, and T. Knöpfel. Morphological and electrophysiological properties of gabaergic and non-gabaergic cells in the deep cerebellar nuclei. *Journal of Neurophysiology*, 97(1):901–911, 2007. (Cited on pages 26, 27 and 28.)

[71] M. Vergnes, C. Marescaux, G. Micheletti, J. Reis, A. Depaulis, L. Rumbach, and J. Warter. Spontaneous paroxysmal electroclinical patterns in rat: a model of generalized non-con- vulsive epilepsy. *Neuroscience Letters*, 33:97–101, 1984. (Cited on page 17.)

[72] D. Wolpert. Stacked generalization. *Neural Networks*, 1992. (Cited on page 89.)

[73] D. Wulsin, J. Gupta, R. Mani, J. Blanco, and B. Litt. Modeling eeg waveforms with semi-supervised deep belief nets: Fast classification and anomaly measurement. *J Neural Eng.*, 8(3):036015, 2011. (Cited on page 4.)

[74] R. Xu and D. Wunsch II. Survey of clustering algorithms. *IEEE TRANSACTIONS ON NEURAL NETWORKS,*, 16(3):645–676, 2005. (Cited on pages 50 and 51.)

Appendices

Appendix A

Growing Neural Gas Algorithm

- Place two nodes, n_a and n_b, randomly in the multi-dimensional data space
- Connect n_a and n_b by an edge. Assign a variable, *age*, to the newly created edge. This variable determines when an edge is to be removed.
- Select a data point, d, from the data and find the node nearest to the data point. Assign this node, w, as the winner and the second nearest node the second-winner, s.
- Increment the age of all the edges emanating from w and s
- Add the squared distance between w and d to the local variable of w, *error.*
- Move the node w and its immediate neighbours towards d by a value determined by the constants α and β respectively.
- If w and s are connected by an edge, reset the *age* of the edge to zero. If they are not connected by an edge, create an edge and initialise the *age* of the edge to zero
- Remove all edges with an age greater than the constant D_{max}
- Remove all the nodes that do not have edges emanating from them.
- Repeat the steps 3-9. If the number of data points sampled is an integer multiple of the parameter λ, then insert a new node as follows:
- Select the node with the greatest *error* value n_e. Place the new node n_n halfway between the nodes n_e and its neighbour n_f, with the highest *error* value.
- Remove the original edge connecting n_e and $n_f$and connect the new node n_n to the nodes n_e and n_f by edges.
- Decrease the *error* variables of n_e and n_f by a quantity specified by δ. Initialize the *error* variable of n_f by the new error value calculated for the node n_e
- Decrease all the *error* variables by the constant d.
- Execute steps 3 to 11 until the maximum numbers of nodes have been inserted or a performance criteria has been met.

Algorithm 2: Growing Neural Gas Algorithm

APPENDIX B

Publications

Evolution of Dendritic Morphologies Using Deterministic and Nondeterministic Genotype to Phenotype Mapping

Parimala Alva[1], Giseli de Sousa[1,2], Ben Torben-Nielsen[3], Reinoud Maex[4], Rod Adams[1], Neil Davey[1], and Volker Steuber[1]

[1] STRI, University of Hertfordshire, Hatfield, UK
{p.alva2,r.g.adams,n.davey,v.steuber}@herts.ac.uk
[2] Federal University of Santa Catarina, Brazil
[3] École Polytechnique Fédérale de Lausanne, Switzerland
[4] École Normale Supérieure, France

Abstract. In this study, two morphological representations in the genotype, a deterministic and a nondeterministic representation, are compared when evolving a neuronal morphology for a pattern recognition task. The deterministic approach represents the dendritic morphology explicitly as a set of partitions in the genotype which can give rise to a single phenotype. The nondeterministic method used in this study encodes only the branching probability in the genotype which can produce multiple phenotypes. The main result is that the nondeterministic method instigates the selection of more symmetric dendritic morphologies which was not observed in the deterministic method.

Keywords: pattern recognition, evolutionary algorithm.

1 Introduction

A variety of neurons are present in the brain and different types of neurons exhibit distinct dendritic morphologies. Recent work has shown that dendritic morphologies affect the back propagation of action potentials, synaptic integration and other aspects which have implications for the proper functioning of the neuron[5,7]. However, a clear understanding of the computational implications of dendritic structure does not exist. One approach to try to understand how the dendritic structure is related to function is to optimize the dendritic morphology of a neuronal model for a particular task using an Evolutionary Algorithm. The best individuals produced as a result of the evolution can act as an indicator as to which features of the dendritic morphology are important for that particular function.

In previous work, de Sousa[2] presented an algorithm, hereafter referred to as the de Sousa algorithm, where the dendritic morphology best suited for a pattern recognition task was studied. The purpose of the present study is to verify if the results obtained by the de Sousa algorithm are not merely a consequence

V. Mladenov et al. (Eds.): ICANN 2013, LNCS 8131, pp. 319–326, 2013.

of the way the algorithm is implemented and if they do indeed show general properties of neurons which are best suited for pattern recognition. This is done by applying a different algorithm, the Torben-Nielsen algorithm[1] which uses a nondeterministic method of genotype to phenotype mapping as opposed to the deterministic genotype to phenotype mapping used in the de Sousa algorithm, to the same task of pattern recognition in neurons. It is interesting to see if the two different methods for specifying morphology in the genotype highlight the same features of a dendritic morphology as being important for pattern recognition.

2 Pattern Recognition in Neurons

The pattern recognition capability of neurons enables them to distinguish between learned and novel patterns. In this study, a simple one-shot Hebbian Learning[9] has been used in the neuronal models: if the N binary patterns to be learned are $\boldsymbol{x}^{\mu}$ ($\mu\ is\ 1..N$), then the weight at synapse i is given by $w_i = \sum\limits_{\mu} x_i^{\mu}$. In the recall phase, a set of novel patterns are presented along with the stored patterns. As a consequence of the change in the synaptic weights, the neuronal model produces a higher amplitude of Excitatory Post Synaptic Potentials (EPSPs) for the stored patterns than for the novel patterns (see [8]).

3 Methods

The steps followed by the two algorithms, the de Sousa algorithm and the modified Torben-Nielsen algorithm, are depicted in Fig. 1. We use the term 'modified' because the original algorithm developed by Ben Torben-Nielsen to evolve neuronal models for co-incidence detection could not be used as-is for comparison with the results of the de Sousa algorithm. Some modifications were necessary to ensure a fair comparison between the two algorithms. The modifications made to the algorithm are listed here:

1. The algorithm was modified to generate fixed size trees. The number of terminal nodes, length, diameter, tapering of the compartments, and other parameters relating to the pattern recognition task were set to the values used in the de Sousa algorithm.
2. In the original algorithm, the branch probability at every bifurcation point was a function of the distance of the bifurcation point from the soma of the neuronal model. This was changed and a new method (see Section 3.1) was implemented to give us more variation in the genotypes produced.
3. The ability of the branch to bifurcate, extend or terminate at every branch point was restricted to bifurcate or terminate in order to produce trees with fixed sized compartments.
4. The original algorithm ensures that a single genotype maps to a single phenotype by fixing the random seed used in each optimization run. In the modified version of the algorithm, a single genotype can map to a range of phenotypes.

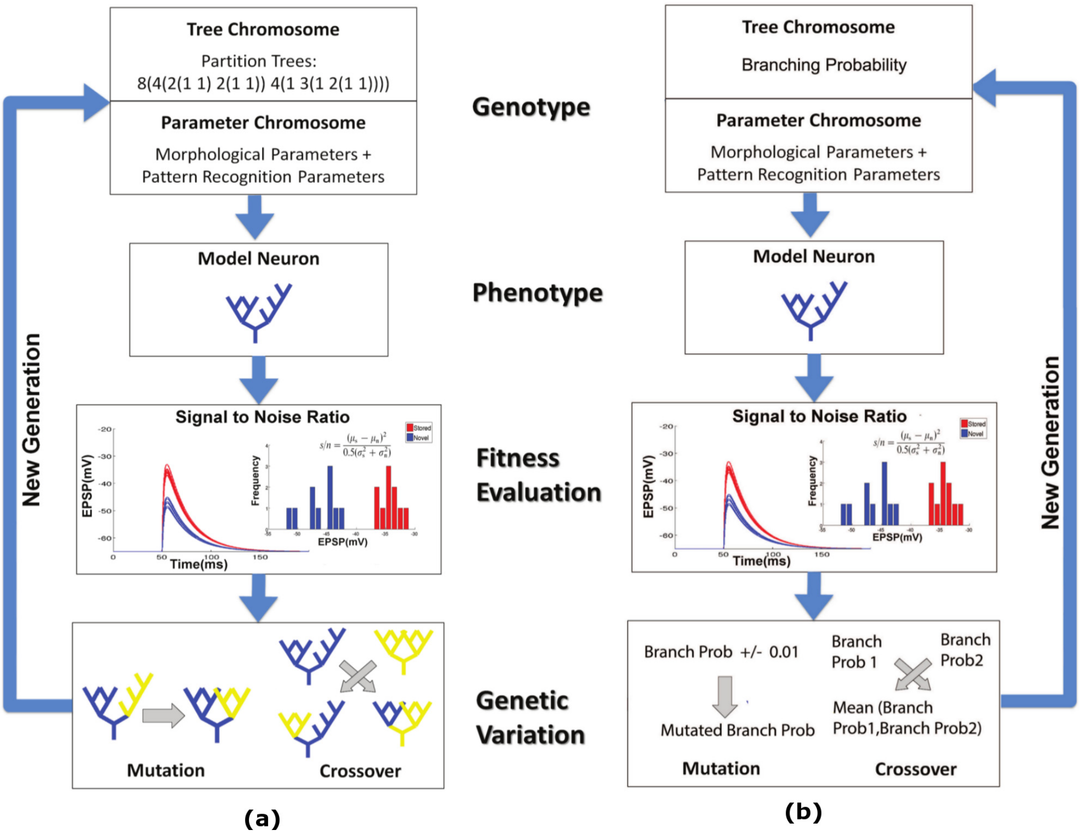

Fig. 1. Steps of the evolutionary algorithm followed by the de Sousa Algorithm (a) and the modified Torben-Nielsen algorithm (b). The de Sousa Algorithm represents the morphology of the neuronal model as partitions in the genotype while the modified Torben-Nielsen algorithm encodes only the branching probability in the genotype.

A detailed description of each step of the Evolutionary Algorithm pertaining to the de Sousa algorithm and the modified Torben-Nielsen algorithm is presented in the following sub-section.

3.1 Genotype Representation

The de Sousa algorithm encodes the exact branching pattern of the dendritic tree in the genotype. The branching pattern of the phenotype is represented as a set of partitions using the method proposed by Van Pelt and Verwer [3].

The modified Torben-Nielsen algorithm uses a nondeterministic method of genotype to phenotype mapping. In this method, the morphology of the entire dendritic tree is specified only by a branching probability, a number between 0 and 1, in the genotype. Other morphological parameters similar to the de Sousa algorithm may also be encoded in the genotype but in the results presented here we kept them fixed.

Algorithm 1. The modified Torben-Nielsen Algorithm for genotype to phenotype mapping.

```
while(number of terminal nodes < 128)
{
    traverse the bottom ply of the tree from left to right
    for(each node visited)
    {
        bifurcate or terminate according to branching probability
    }
    if(no node chooses to bifurcate)
    {
        force the last node visited to bifurcate
    }
 }
```

3.2 Genotype to Phenotype Mapping

The genotype to phenotype mapping in the de Sousa algorithm is fairly straightforward. The partitions in the genotype dictate the morphology of the phenotype. At every bifurcation point, a partition specifies the number of terminal nodes in the right and left sub-tree. In the modified version of the Torben-Nielsen algorithm, the branching probability which is part of the genotype affects the morphology of the phenotype produced. For example, a branching probability value of 0.75 means that at every branch point, the branch has 0.75 probability of bifurcating and 0.25 probability of terminating. Different branching probabilities give rise to different types of dendritic trees in terms of asymmetry and mean depth. The asymmetry index as given by Van Pelt et al.[4] indicates the overall shape while the mean depth metric [2] indicates the average distance between the synapse and the soma of the neuronal model. Figure 2b shows the variation of asymmetry index and mean depth of the phenotypes for sample branching probability values of 0.25, 0.50, and 0.75. From this figure, we can observe that the same branching probability, or the same genotype, can produce a range of phenotypes that vary in terms of asymmetry index and mean depth. Algorithm 1 shows the detailed steps followed in the generation of the phenotype from the genotype using the modified Torben-Nielsen algorithm.

Note that in Algorithm 1 the tree is likely to be skewed to the right, a desirable feature because we wanted also to have asymmetrical trees in our population. The higher frequency of dendritic trees having an asymmetry index of 0.99, as shown in Fig. 2a, is also a result of the forced bifurcation of the last visited node as shown in Algorithm 1. Figure 2b shows the variation of asymmetry index and mean depth of the phenotypes for sample branching probability values of 0.25, 0.50, and 0.75. The tree morphology which is a result of genotype to phenotype mapping, in case of both algorithms, is converted into a neuronal model using the NEURON simulator software[6]. The neuronal model has a membrane capacitance (C_m) of 0.75 μF/cm^2, an axial resistance(R_a) of 150 Ωcm,

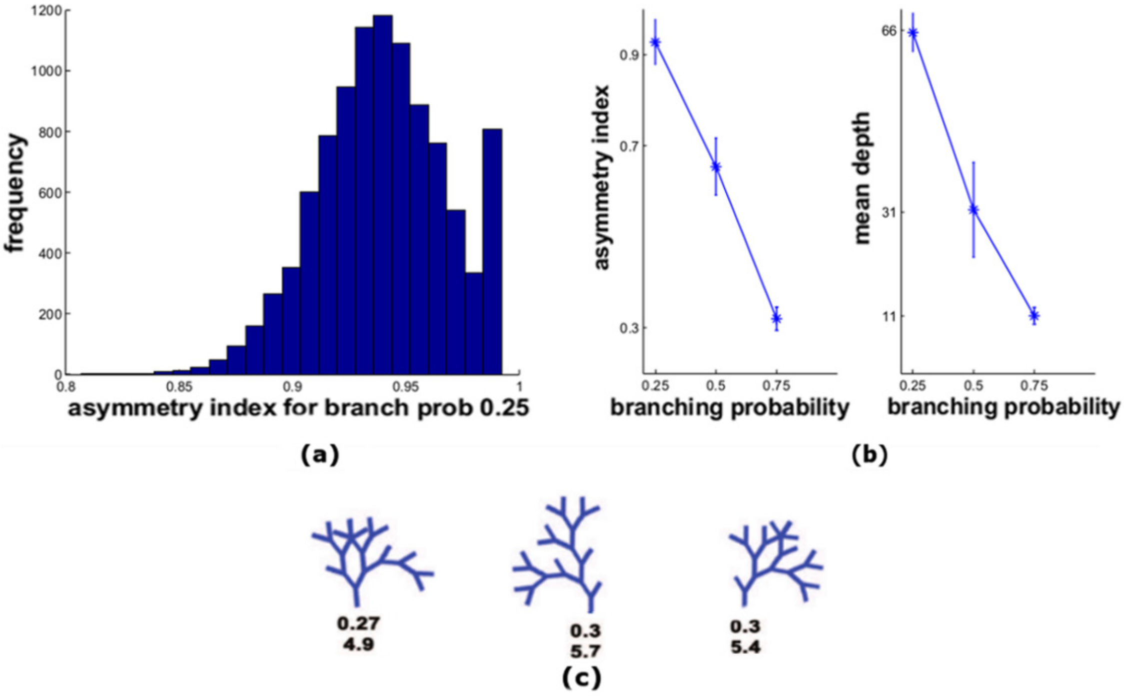

Fig. 2. (a)Histogram showing the distribution of asymmetry indices of the dendritic trees for a branching probability of 0.25 when the modified Torben-Nielsen algorithm is used. (b) Mean and Standard Deviation Graphs showing the range of the asymmetry index and mean depth for sample branching probabilities of 0.25, 0.50, 0.75.(c) Three different tree structures, each having a different asymmetry index (the first row below the tree) and mean depth (second row), produced from the same genotype having a branching probability of 0.75.

a specific membrane resistance (R_m) of 30 kΩcm^2 and a leak reversal potential of $Eleak$=-70 mV. Each compartment of the neuronal model is of equal length and diameter with no tapering. Since this study is limited to studying passive neuronal models, active conductances are not applied to the model.

3.3 Fitness Function

Since the neuronal models used in this study are passive, the response of the neuronal model to the pattern presented is measured by the amplitude of the EPSPs produced in the soma. The ability of the neuron to distinguish between stored and new patterns is determined by the signal to noise ratio of the amplitudes of the EPSP produced by stored and novel patterns (see [8]).

3.4 Genetic Variation

In case of both algorithms, a process of selection is applied to the population to select the best 10 % of the individuals to be propagated to the next generation. As is normally the case, selection, crossover and mutation are applied to the population to produce the next generation.

4 Results

To evaluate the morphology of the dendritic tree best suited for pattern recognition, we observe the change of asymmetry index and mean depth of the dendritic trees. Details of calculation of the metrics, asymmetry index and mean depth, have been given in [2].

4.1 Results of the de Sousa Algorithm

The change of values of the fitness as well as the two morphological metrics are observed over 60 generations of the de Sousa algorithm as shown in Fig. 3a. The initial population for this experiment is biased to consist mainly of asymmmetric morphologies. However, a huge drop in the asymmetry index and mean depth values are observed within the first few generations indicating that neuronal models with more symmetrical morphologies and lower mean depth perform better. However, this does not mean that the asymmetry index and fitness are inversely correlated over the whole range of asymmetry indices. After the dendritic trees achieve an asymmetry index of about 0.4, a further reduction in asymmetry does not increase the fitness of the dendritic trees. When dendritic trees with similar asymmetry index were binned together and their mean depth values evaluated as shown in Fig. 3c, it was noticed that the dendritic trees with asymmetry indices of about 0.4 and lower had very similar values of mean depth. This may explain the plateau in the fitness value after an asymmetry index of 0.4 was reached, and it suggests that perhaps mean depth is a better indicator of pattern recognition performance than asymmetry index.

4.2 Results of the Modified Torben-Nielsen Algorithm

The same experiment, where the initial population was biased to consist mainly of asymmetric morphologies, was executed for the modified Torben-Nielsen algorithm. As shown in Fig. 3b, the results of the experiment follow the same pattern as for the de Sousa algorithm in the case of fitness and mean depth values. The main difference was the change of the asymmetry index of the dendritic trees. In the de Sousa algorithm, the asymmetry index remains at a value of about 0.4 and does not reduce further as this value of asymmetry index is sufficient to produce the best individual for pattern recognition. However, with the modified Torben-Nielsen algorithm, the asymmetry index of the dendritic trees reduces to a value of around 0.2 at the end of 100 generations. This is a consequence of the nondeterministic approach used in this study, which generates a new tree instantiation each time a new individual is passed to the next generation. As shown in Fig. 2a and Fig. 2b, a single genotype can map to different phenotypes that vary in asymmetry index and mean depth. Since there is a considerable variation in the type of phenotype produced by a single genotype, there is an additional pressure on the Evolutionary Algorithm to select a genotype such that all resulting phenotypes perform well. This forces the algorithm to select genotypes which produce, on average, more symmetrical trees

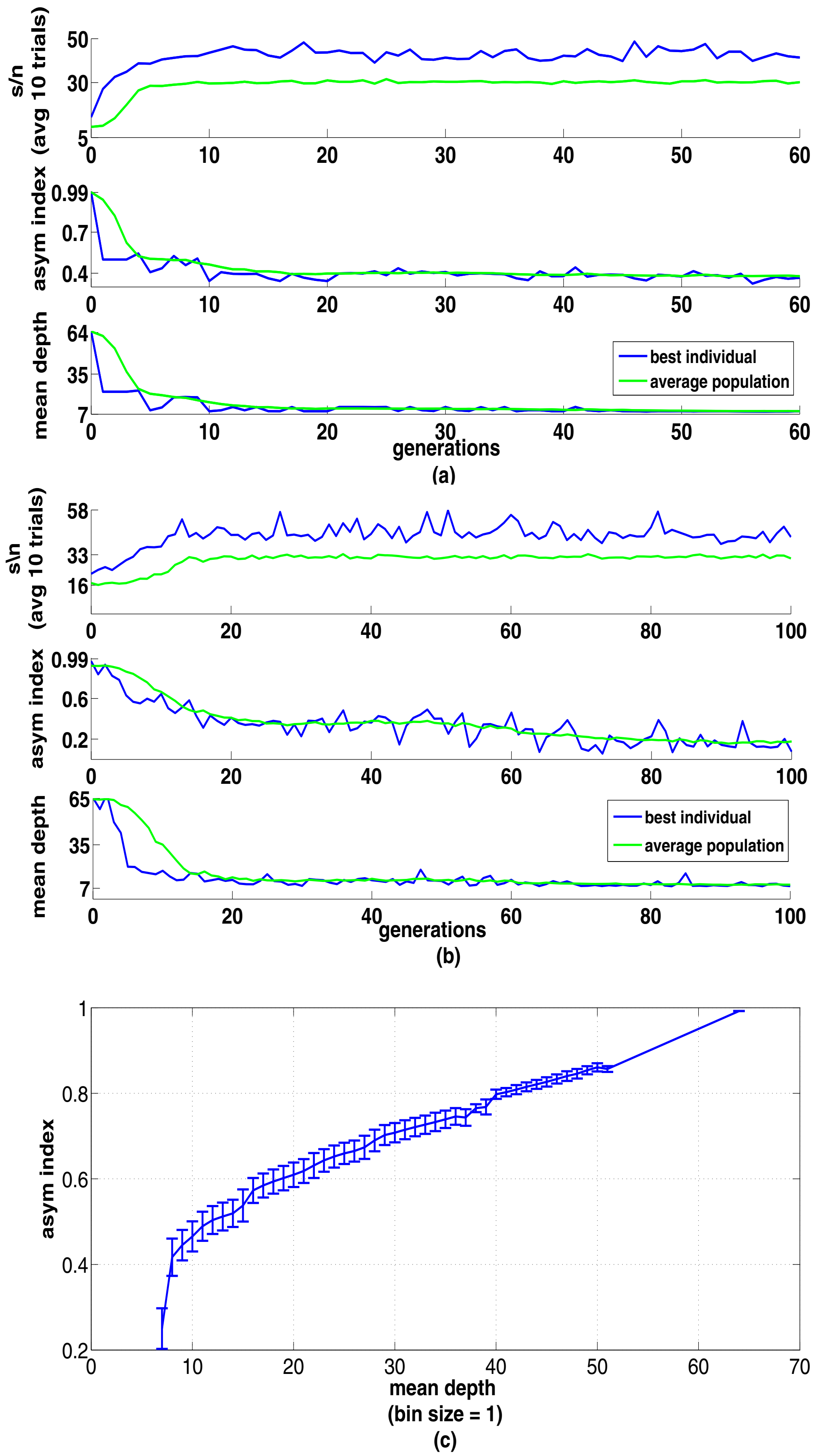

Fig. 3. (a) Change of fitness, asymmetry index and mean depth in the de Sousa algorithm. (b) Change of fitness, asymmetry index and mean depth in the Torben-Nielsen algorithm. (c) Mean depth vs asymmetry index for dendritic trees in the de Sousa algorithm.

than their counterparts which show mixed asymmetry values. The final outcome of this experiment reinforces the results produced by the de Sousa algorithm that symmetrical neuronal morphologies which have low mean depth values are well suited for pattern recognition.

5 Conclusion

Previous work [2] has shown that a Genetic Algorithm will reduce the mean depth of the dendritic tree in order to improve the pattern recognition performance. Here we demonstrate that the same principle applies with a different morphological specification, namely a nondeterministic mapping of the genotype to the dendritic tree morphology. The nondeterministic method of genotype to phenotype mapping showed that when a single genotype can map to an array of phenotypes, the criterion for the selection of genotypes was more stringent, which led to the selection of genotypes that gave rise to more symmetrical morphologies. Symmetric morphologies have a smaller mean depth and therefore lead to less variance in responses and a higher signal to noise ratio. However, in real neurons we do not always find this symmetric morphology because the morphology of a real neuron is governed by other factors such as the need to form synaptic contacts in certain locations.

References

1. Torben-Nielsen, B., Stiefel, K.M.: An inverse approach for elucidating dendritic function. Front. Comput. Neurosci. 4, 128 (2010)
2. de Sousa, G., Maex, R., Adams, R., Davey, N., Steuber, V.: Evolving dendritic morphology and parameters in biologically realistic model neurons for pattern recognition. In: Villa, A.E.P., Duch, W., Érdi, P., Masulli, F., Palm, G. (eds.) ICANN 2012, Part I. LNCS, vol. 7552, pp. 355–362. Springer, Heidelberg (2012)
3. van Pelt, J., Verwer, R.: Growth models (including terminal and segmental branching) for topological binary trees. Bull. Math. Biol. 47, 323–326 (1985)
4. van Pelt, J., Uylings, H.B., Verwer, R.W., Pentney, R.J., Woldenberg, M.J.: Tree asymmetry–A sensitive and practical measure for binary topological trees. Bull. Math. Biol. 54, 759–784 (1992)
5. Spruston, N.: Pyramidal neurons: dendritic structure and synaptic integration. Nat. Rev. Neurosci. 9, 206–221 (2008)
6. Carnevale, N.T., Hines, M.L.: The NEURON Book. Cambridge University Press, Cambridge (2006)
7. Vetter, P., Roth, A., Häusser, M.: Propagation of Action Potentials in Dendrites Depends on Dendritic Morphology. J. Neurophysiol. 85, 926–937 (2001)
8. Steuber, V., De Schutter, E.: Long-term depression and recognition of parallel fibre patterns in a multi-compartmental model of a cerebellar Purkinje cell. Neurocomputing 38-40, 383–388 (2001)
9. Hertz, J., Krogh, A., Palmer, R.G.: Introduction to the Theory of Neural Computation. Addison-Wesley, Reading (1991)

Alva *et al. BMC Neuroscience* 2013, **14**(Suppl 1):P170
http://www.biomedcentral.com/1471-2202/14/S1/P170

BMC Neuroscience

POSTER PRESENTATION **Open Access**

A potential role for the cerebellar nuclei in absence seizures

Parimala Alva[1*], Lieke Kros[2], Reinoud Maex[3], Chris I De Zeeuw[2], Rod Adams[1], Neil Davey[1], Volker Steuber[1], Freek E Hoebeek[2]

From Twenty Second Annual Computational Neuroscience Meeting: CNS*2013
Paris, France. 13-18 July 2013

Absence seizures are characterized by a temporary lapse of consciousness, which typically lasts up to ten seconds, and they are accompanied by spike-wave discharges (SWDs) in cerebral electroencephalogram (EEG) recordings. The oscillatory activity that underlies cortical SWDs has been shown to often originate from a specific focus that can be located in various brain regions, such as the cerebral cortex, thalamus or hippocampus [1]. Yet, the role of the cerebellum, which is anatomically connected to each of these potential foci, is unknown. Here, we used *Cacna1a*^{tottering} *(tg)* mice, an established model for absence epilepsy characterized by a loss-of-function of

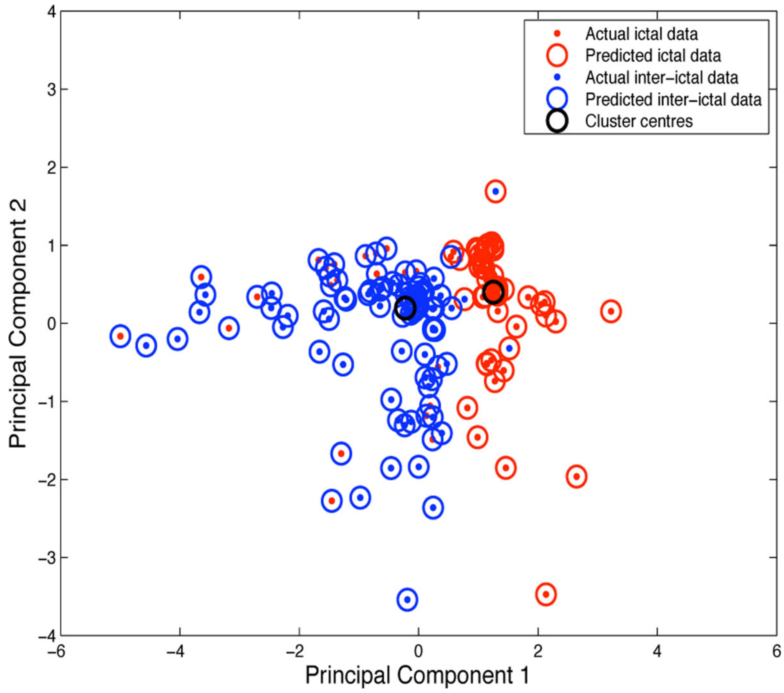

Figure 1 K-Means clustering showing two distinct clusters for ictal and inter-ictal data. The two variables, principal component 1 and principal component 2 are derived by PCA of CV, CV2 and PE of ictal and inter-ictal data.

---

* Correspondence: p.alva2@herts.ac.uk
[1]Science and Technology Research Institute, University of Hertfordshire, Hatfield, AL10 9AB, UK
Full list of author information is available at the end of the article

calcium channels [3], to study how the cerebellar activity changes during absence seizures. Given that recent evidence shows that cerebellar Purkinje cells in *tottering* mice exhibit an altered expression of calcium channels [2] and structurally abnormal synapses in the cerebellar nuclei (CN), it is our hypothesis that the cerebellar output, which is dominated by neurons in the CN, changes during absence seizures.

In the present study, we analysed extracellular spike trains of CN units, and simultaneous EEG recordings, in ten awake head-restrained mice. The recordings were partitioned into equal-length segments of 900 ms and, depending on whether spike-wave discharges occurred in the EEG or not, considered as ictal or inter-ictal data. The metrics considered for analysis were the CV, CV2, firing rate and permutation entropy (PE). When a one-dimensional analysis of the metrics for ictal and inter-ictal data was conducted, it was noted that a single metric was not sufficient to differentiate between the ictal and inter-ictal data. Therefore, the three variables, CV, CV2 and PE, were combined to form two new variables, Principal Component 1 and Principal Component 2 (Figure 1), using Principal Component Analysis (PCA). The two new variables, Principal Component 1 and Principal Component 2, were then subjected to cluster analysis using K-Means clustering having two centers. Firing rate was not considered for PCA and clustering as better results were achieved while excluding it.

The result, shown in Figure 1, depicts two distinct clusters for ictal and inter-ictal data. The confusion matrix for this data denotes true positive where predicted ictal data match actual ictal data (95.7%), true negative where predicted inter-ictal data match actual inter-ictal data (70%), false positive for actual ictal data incorrectly predicted as inter-ictal data (4.3%), and false negatives for actual inter-ictal data incorrectly predicted as ictal data (30%). The F-score achieved by this classification was 0.84. The separation between the ictal and inter-ictal data could further be improved by the application of Support Vector Machines (SVMs). We are currently using a conductance based model of a CN neuron to study which conditions can result in spike patterns associated with seizures.

Author details

[1]Science and Technology Research Institute, University of Hertfordshire, Hatfield, AL10 9AB, UK. [2]Department of Neuroscience, Erasmus Medical Center, Rotterdam, The Netherlands. [3]Department of Cognitive Sciences, École Normale Supérieure, Paris 75005, France.

Published: 8 July 2013

References

1. Danober L, Deransart C, Depaulis A, Vergnes M, Marescaux C: **Pathophysiological mechanisms of genetic absence epilepsy in the rat.** *Progress in Neurobiology* 1998, **55(127)**:57.
2. Hoebeek FE, Khosrovani S, Witter L, De Zeeuw CI: **Purkinje cell input to cerebellar nuclei in tottering: ultrastructure and physiology.** *Cerebellum* 2008, **7(4)**:547-558.
3. Noebels JL, Sidman RL: **Inherited epilepsy: spike-wave and focal motor seizures in the mutant mouse tottering.** *Science* 1979, **204(4399)**:1334-1336.

doi:10.1186/1471-2202-14-S1-P170
Cite this article as: Alva *et al.*: A potential role for the cerebellar nuclei in absence seizures. *BMC Neuroscience* 2013 **14**(Suppl 1):P170.

Alva *et al. BMC Neuroscience* 2014, **15**(Suppl 1):P39
http://www.biomedcentral.com/1471-2202/15/S1/P39

BMC Neuroscience

POSTER PRESENTATION Open Access

Combining machine learning and simulations of a morphologically realistic model to study modulation of neuronal activity in cerebellar nuclei during absence epilepsy

Parimala Alva[1*], Lieke Kros[2], Oscar H J Eelkman Rooda[2], Chris I De Zeeuw[3], Rod Adams[1], Neil Davey[1], Freek E Hoebeek[2], Volker Steuber[1]

From The Twenty Third Annual Computational Neuroscience Meeting: CNS*2014
Québec City, Canada. 26-31 July 2014

Epileptic absence seizures are characterized by synchronized oscillatory activity in the cerebral cortex that can be recorded as so-called spike-and-wave discharges (SWDs) by electroencephalogram. Although the cerebral cortex and the directly connected thalamus are paramount to this particular form of epilepsy, several other parts of the mammalian brain are likely to influence this oscillatory activity. We have recently shown that some of the cerebellar nuclei (CN) neurons, which form the main output of the cerebellum, show synchronized oscillatory activity during episodes of cortical SWDs in two independent mouse models of absence epilepsy [1]. The CN neurons that show this significant correlation with the SWDs are deemed to "participate" in the seizure activity and are therefore used in our current study designed to unravel the potential causes of such oscillatory firing patterns.

Initially, we set out to study if different types of CN neurons are more prone to show modulated firing patterns during seizure activity. We applied Growing Neural Gas (GNG) [2], an unsupervised clustering algorithm, on the interictal activity, i.e., firing patterns recorded in between seizures, using the measures CV, log-interval entropy, permutation entropy and firing rate. Three main groups of neurons were found by the clustering algorithm, in which the neurons were predominantly participating in the seizures. These can be seen on Figure 1 as the green, yellow and pale blue crosses (+). Moreover, these three clusters have the highest CV (and therefore more irregular) and higher log-interval entropy (more unpredictable). Further, we used a Gaussian Process Regression model [3] to predict the extent of participation of the neurons in the seizure activity, based on two measures: Z-score of mean power at seizure frequency (6-9Hz) (FFT based Z-score) and modulation frequency. These characterize the extent to which CN neurons phase-lock their spiking activity to the spikes in the EEG during seizures. We achieved a good prediction rate ($r = 0.56$, $p < 0.05$ for FFT based Z-score;

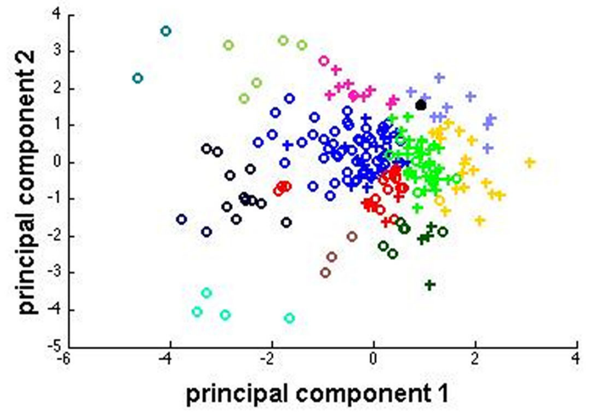

Figure 1 shows 2D projection, using principal component analysis, of the clusters formed as a result of GNG clustering of the CN neuron interictal activity using CV, Log-Interval Entropy, Firing rate and Permutation Entropy. The crosses (+) indicate cells that participate in the seizure and (o) indicate the cells that do not participate based on the measures, FFT based Z-score and modulation frequency. The black dot indicates the output from the computer simulations

---

* Correspondence: p.alva2@herts.ac.uk
[1] Science and Technology Research Institute, University of Hertfordshire, Hatfield AL10 9AB, UK
Full list of author information is available at the end of the article

$r = 0.45$, $p < 0.05$ for modulation frequency) using this method. Also, we are using a compartmental model of a CN neuron with realistic morphology [4] to investigate the input conditions that can generate interictal activity found in the participating neurons. Our results indicate that bursting in the Purkinje cell or mossy fiber input can cause behavior that is similar to the interictal activity found in participating neurons. The black dot in Figure 1 shows the output from the CN neuron model, provided with a bursting Purkinje cell input, when it is subjected to clustering with the experimental data. Desynchronization of the burst occurrence in the input did not alter the position of the data point drastically[0]. Currently, we are in the process of applying an evolutionary algorithm to explore in detail the input conditions that can that lead to the spiking behavior that is associated with seizures.

Authors' details
[1]Science and Technology Research Institute, University of Hertfordshire, Hatfield AL10 9AB, UK. [2]Department of Neuroscience, Erasmus Medical Center, Rotterdam, The Netherlands. [3]Netherlands Institute for Neuroscience, Royal Dutch Academy for Arts and Sciences, Amsterdam, Netherlands.

Published: 21 July 2014

References

1. Kros , *et al*: Absence seizures stopped by closed-loop activation of cerebellar output. *FENS Forum Abstr* 2014.
2. Fritzke B: A Growing Neural Gas Network Learns Topologies. *Neural Information Processing Systems* 1994, **7**:625-632.
3. Rasmussen CE, Williams CKI: Gaussian Processes for Machine Learning. The MIT Press; 2006.
4. Steuber V, Schultheiss N, Silver RA, Schutter E, Jaeger D: Determinants of synaptic integration and heterogeneity in rebound firing explored with data-driven models of deep cerebellar nucleus cells. *J Comp Neurosci* 2011, **30(3)**:633-658.

doi:10.1186/1471-2202-15-S1-P39
Cite this article as: Alva *et al.*: Combining machine learning and simulations of a morphologically realistic model to study modulation of neuronal activity in cerebellar nuclei during absence epilepsy. *BMC Neuroscience* 2014 **15**(Suppl 1):P39.

Cerebellar Output Controls Generalized Spike-and-Wave Discharge Occurrence

Lieke Kros, PhD,[1] Oscar H. J. Eelkman Rooda, MD, MSc,[1]
Jochen K. Spanke, MSc,[1] Parimala Alva, MSc,[2] Marijn N. van Dongen, PhD,[3]
Athanasios Karapatis, BEng,[3] Else A. Tolner, PhD,[4] Christos Strydis, PhD,[1]
Neil Davey, PhD,[2] Beerend H. J. Winkelman, PhD,[5] Mario Negrello, PhD,[1]
Wouter A. Serdijn, PhD,[3] Volker Steuber, PhD,[2]
Arn M. J. M. van den Maagdenberg, PhD,[4,6]
Chris I. De Zeeuw, MD, PhD,[1,5] and Freek E. Hoebeek, PhD[1]

Objective: Disrupting thalamocortical activity patterns has proven to be a promising approach to stop generalized spike-and-wave discharges (GSWDs) characteristic of absence seizures. Here, we investigated to what extent modulation of neuronal firing in cerebellar nuclei (CN), which are anatomically in an advantageous position to disrupt cortical oscillations through their innervation of a wide variety of thalamic nuclei, is effective in controlling absence seizures.
Methods: Two unrelated mouse models of generalized absence seizures were used: the natural mutant *tottering*, which is characterized by a missense mutation in *Cacna1a*, and inbred *C3H/HeOuJ*. While simultaneously recording single CN neuron activity and electrocorticogram in awake animals, we investigated to what extent pharmacologically increased or decreased CN neuron activity could modulate GSWD occurrence as well as short-lasting, on-demand CN stimulation could disrupt epileptic seizures.
Results: We found that a subset of CN neurons show phase-locked oscillatory firing during GSWDs and that manipulating this activity modulates GSWD occurrence. Inhibiting CN neuron action potential firing by local application of the γ-aminobutyric acid type A (GABA-A) agonist muscimol increased GSWD occurrence up to 37-fold, whereas increasing the frequency and regularity of CN neuron firing with the use of GABA-A antagonist gabazine decimated its occurrence. A single short-lasting (30–300 milliseconds) optogenetic stimulation of CN neuron activity abruptly stopped GSWDs, even when applied unilaterally. Using a closed-loop system, GSWDs were detected and stopped within 500 milliseconds.
Interpretation: CN neurons are potent modulators of pathological oscillations in thalamocortical network activity during absence seizures, and their potential therapeutic benefit for controlling other types of generalized epilepsies should be evaluated.

ANN NEUROL 2015;77:1027–1049

Absence epilepsy is among the most prevalent forms of generalized epilepsy among children and is characterized by sudden periods of impaired consciousness and behavioral arrest.[1,2] Like other types of generalized epilepsies, absence seizures are electrophysiologically defined by oscillatory activity in cerebral cortex and the thalamic complex.[3] Thalamocortical oscillations are primarily caused by excessive cortical activity and can be identified in the electrocorticogram (ECoG) as generalized spike-and-wave discharges (GSWDs).[3,4] The underlying excessive cortical activity not only excites thalamic neurons, but also provides potent bisynaptic inhibition

View this article online at wileyonlinelibrary.com. DOI: 10.1002/ana.24399

Received Nov 7, 2014, and in revised form Mar 2, 2015. Accepted for publication Mar 3, 2015.

Address correspondence to Dr Hoebeek, Department of Neuroscience, Erasmus MC, Wytemaweg 80, 3015 CN, Rotterdam, the Netherlands.
E-mail: f.hoebeek@erasmusmc.nl

From the [1]Department of Neuroscience, Erasmus Medical Center, Rotterdam, the Netherlands; [2]Science and Technology Research Institute, University of Hertfordshire, Hatfield, United Kingdom; [3]Bioelectronics Section, Faculty of Electrical Engineering, Mathematics, and Computer Science, Delft University of Technology, Delft, the Netherlands; [4]Department of Neurology, Leiden University Medical Center, Leiden, the Netherlands; [5]Netherlands Institute for Neuroscience, Royal Dutch Academy for Arts and Sciences, Amsterdam, the Netherlands; and [6]Department of Human Genetics, Leiden University Medical Center, Leiden, the Netherlands

Additional Supporting Information may be found in the online version of this article.

by means of cortical axonal collaterals to the inhibitory reticular thalamic nucleus.[3,5–7] Excess tonic γ-aminobutyric acid (GABA)-mediated inhibition in thalamus may also contribute to absence seizures.[3,7,8] Oscillatory cortical activity thereby poses a dual excitation–inhibition effect on thalamic neurons, which drives thalamocortical network oscillations.[5,7–9]

Recent studies in several rodent models indicate that direct stimulation of thalamic nuclei[10] or cerebral cortex[11] can be effective in disrupting thalamocortical oscillations and thereby stopping generalized oscillations in thalamocortical networks, such as GSWDs. Apart from direct interventions in thalamus and cortex, thalamic afferents can affect the balance in excitation and inhibition and thereby potentially mediate thalamocortical oscillations. One of the initial stimulation sites to prevent seizures in epileptic patients was the cerebellar cortex.[12–18] Yet, as shown in 3 controlled, blind studies,[19–21] the impact of these cerebellar surface stimulations was highly variable and probably reflects irregularities in the converging inputs from superficial and deeper parts of the cerebellar cortex neurons to the cerebellar nuclei (CN).[22]

Given the considerable divergence of excitatory axonal projections from the CN to a wide range of motor, associative, and intralaminar thalamic nuclei,[4,6,23–29] we considered this region an ideal candidate to effectively modulate thalamocortical oscillations. We hypothesized that altering the firing patterns of CN neurons should affect GSWD occurrence. To test this hypothesis, we utilized homozygous *tottering* (*tg*) mice that frequently show absence seizures and harbor a P601L missense mutation in the *Cacna1a* gene that encodes the pore-forming α_{1A}-subunit of voltage-gated $Ca_V2.1$ Ca^{2+} channels.[30,31] Once we established that *tg* CN neurons showed oscillatory action potential firing patterns comparable to that found in rat models for absence epilepsy,[32] we assessed the effect of increasing or decreasing CN neuronal firing on GSWD occurrence by local pharmacological interventions using modulators of $GABA_A$-mediated neurotransmission. In addition, we generated a closed-loop detection system for on-demand optogenetic stimulation to stimulate CN neurons with millisecond precision. Finally, to exclude the possibility that our design of intervention is tailored to the specific pathophysiology of *tg* mice, we extended our key experiments to an unrelated mouse model for absence epilepsy: the *C3H/HeOuJ* inbred mouse line.[33]

Materials and Methods

All experiments were performed in accordance with the European Communities Council Directive. Protocols were reviewed and approved by local Dutch experimental animal committees.

Animals

Data were collected from 4- to 30-week-old homozygous and wild-type littermates of natural mutant *tg* mice and 8- to 10-week-old inbred *C3H/HeOuJ* mice. Male and female *tg* and wild-type littermates were bred using heterozygous parents. The colony, which was originally obtained from Jackson Laboratory (Bar Harbor, ME), was maintained in *C57BL/6NHsd* purchased from Harlan Laboratories (Horst, the Netherlands). Conformation of the presence of the *tg* mutation in the *Cacna1a* gene was obtained by polymerase chain reaction using 5′-TTCTGGGTACCAGATACAGG-3′ (forward) and 5′-AAGTGTCGAAGTTGGTGCGC-3′ (reverse) primers (Eurogentech, Seraing, Belgium) and subsequent digestion using restriction enzyme *NsbI* at the age of postnatal day (P) 9 to P12. Male inbred *C3H/HeOuJ* mice were purchased from Charles River Laboratories (Wilmington, MA).

Experimental Procedures

SURGERY. Mice were anesthetized with isoflurane (4% in 0.5l/min O_2 for induction and 1.5% in 0.5l/min O_2 for maintenance). The skull was exposed, cleaned, and treated with OptiBond All-In-One (Kerr Corporation, Orange, CA) to ensure adhesion of a light-curing hybrid composite (Charisma; Heraeus Kulzer, Hanau, Germany) to the skull to form a pedestal. Subsequently, five 200μm Teflon-coated silver ball tip electrodes (Advent Research Materials, Eynsham, UK) or five 1mm stainless steel screws were subdurally implanted for cortical recordings by ECoG. Four of the electrodes were bilaterally positioned above the primary motor cortex (+1mm anterior-posterior [AP]; ±1mm medial - lateral [ML] relative to bregma) and primary sensory cortex (−1mm AP; ± 3.5mm ML). A fifth electrode was placed in the rostral portion of the interparietal bone to serve as reference (−1mm AP relative to lambda). The electrodes and their connectors were fixed to the skull and embedded in a pedestal composed of the hybrid composite or dental acrylic (Simplex Rapid; Associated Dental Products, Kemdent Works, Purton, UK). To enable optogenetic control of neuronal activity in CN, a subset of *tg* and *C3H/HeOuJ* mice received 2 small (~0.5mm in diameter) craniotomies in the interparietal bone (−2mm AP relative to lambda; ±1.5–2mm ML) to initially accommodate the injection pipette and later the optical fibers. CN were stereotactically injected bilaterally with 100 to 120nl of the AAV2-hSyn-ChR2(H134R)-EYFP vector (kindly provided by Dr K. Deisseroth [Stanford University] through the Vector Core at the University of North Carolina) at a rate of ~20nl/min 3 to 6 weeks prior to recordings. To allow electrophysiological recordings from CN neurons, all mice received bilateral craniotomies (~2mm diameter) in the occipital bone without disrupting the dura mater. Finally, a dental acrylic recording chamber (Simplex rapid) was constructed. The exposed tissue was covered with tetracycline-containing ointment (Terra-cortril; Pfizer, New York, NY) and the recording chamber was sealed with bone wax (Ethicon, Somerville, NJ). After surgery, the mice recovered for at least 5 days (or 3 weeks in the case of virally injected mice) in their home cage and were allowed two ~3-hour sessions on consecutive days during which the mice were left undisturbed to accommodate to the setup.

ELECTROPHYSIOLOGICAL RECORDINGS. During the accommodation session, the animals' motor behavior was visually inspected for behavioral correlates of the oscillatory cortical activity during episodes of GSWDs. No consistent patterns of movement were identified during such epileptic activity, as described before in *tg* and other rodent models of absence epilepsy.[30,32,34] Recordings were performed in awake, head-fixed animals, lasted no longer than 4 consecutive hours, and were performed during various times of day. No consistent pattern was identified in ECoG frequency spectra with respect to the day–night cycle.[35] While being head-restrained, mice were able to move all limbs freely. Body temperature was supported using a homeothermic pad (FHC, Bowdoin, ME). For extracellular single unit recordings, custom-made, borosilicate glass capillaries (outer diameter = 1.5mm, inner diameter = 0.86mm, resistance = 8–12MΩ, taper length = ~8mm, tip diameter = ~1μm; Harvard Apparatus, Holliston, MA) filled with 2M NaCl were positioned stereotactically using an electronic pipette holder (SM7; Luigs & Neumann, Ratingen, Germany). CN were localized by stereotactic location as well as the characteristic sound and density of neuronal activity.[36] To record from medial CN (MCN), electrodes were advanced through vermal lobules 6 to 7 with 0° jaw angle relative to the interaural axis to a depth of 1.6 to 2.4mm. To record from interposed nuclei (IN), electrodes were advanced through the paravermal or hemispheric part of lobules 6 to 7 using a yaw angle of ~10° relative to the interaural axis to a depth of 1.8 to 2.7mm. To record from lateral CN (LCN), electrodes were advanced through the paravermal or hemispheric part of lobules 6 to 7 using a yaw angle of ~25° relative to the interaural axis to a depth of 2.7 to 4mm. A subset of electrophysiological recording sites was identifiable following Evans blue injections (see below) and confirmed the accuracy of our localization technique. ECoGs were filtered online using a 1 to 100Hz band pass filter and a 50Hz notch filter. Single unit extracellular recordings and ECoGs were simultaneously sampled at 20kHz (Digidata 1322A; Molecular Devices, Axon Instruments, Sunnyvale, CA), amplified, and stored for offline analysis (CyberAmp & Multiclamp 700A, Molecular Devices).

PHARMACOLOGICAL MODULATION OF CN NEURONAL ACTION POTENTIAL FIRING. To bilaterally target the CN for pharmacological intervention, their location was first determined as described above, after which we recorded 1 hour of "baseline" ECoG. Next, a borosilicate glass capillary (Harvard Apparatus; tip diameter = ~5μm) filled with 1 of the following mixtures replaced the recording pipette to allow high spatial accuracy of the injection: to decrease CN neuronal action potential firing, we applied 0.5% muscimol ($GABA_A$-agonist; Tocris Bioscience, Bristol, UK) dissolved in 1M NaCl (Sigma-Aldrich, St Louis, MO); to increase CN neuronal action potential firing, we applied 100µM gabazine ($GABA_A$- antagonist; Tocris) dissolved in 1M NaCl; or 1M NaCl for sham injections. The experimenter was blinded for the solutions injected. The solution was bilaterally administered to CN by pressure injections of ~150nl at a rate of ~50nl/min, following which 1 hour of postinjection ECoG was recorded. As an additional control, similarly sized injections of saline with either gabazine or muscimol were administered to lobules 6 and 7 and Crus I and Crus II of the cerebellar cortex. The drugs were injected superficially (0.7–1mm from the surface) to avoid spread to the CN. The locations of the injections were identified with the use of electrophysiological recordings and stereotactic coordinates, and most (19 of 26) CN injections were histologically confirmed using the fluorescence of Evans blue (1% in 1M saline supplied to the injected solution; Supplementary Fig).[37] To verify the effects of muscimol, gabazine, and vehicle, we recorded extracellular activity in the injected area during 20 to 50 minutes after the injections. Immediately after acquiring the postinjection ECoG, an overdose of sodiumpentobarbital (0.15ml intraperitoneally) was administered allowing transcardial perfusion (0.9% NaCl followed by 4% paraformaldehyde in 0.1M phosphate buffer [PB]; pH = 7.4) to preserve the tissue for histological verification of the injections.

OPTOGENETIC STIMULATION OF CN NEURONS. Optic fibers (inner diameter = 200μm, numerical aperture = 0.39; Thor labs, Newton, NJ, USA) were placed ~200μm from the injection site and connected to 470nm or 590nm light-emitting diodes (LEDs; Thor labs), or ~200μm above the brain, that is, in the "wrong location." Light intensity at the tip of the implantable fiber was 550 ± 50μW/mm^2 (measured after each experiment). Activation of LEDs by a single 30- to 300-millisecond pulse was triggered manually (open-loop) or by a closed-loop detection system (as described below). In each mouse, 4 stimulation protocols were used: (1) bilateral stimulation (470nm), (2) unilateral stimulation (470nm), (3) bilateral stimulation (590nm), and (4) bilateral stimulation (470nm) with optical fibers outside of the CN (to exclude potential effects of visual input on the GSWD occurrence.[30,32] After the last experimental session, animals were sedated and perfused (as described above) to preserve tissue for histological verification of channelrhodopsin-2 (ChR2) expression.

IMMUNOFLUORESCENCE. After perfusion, the cerebellum was removed and postfixed in 4% paraformaldehyde in 0.1M PB for 1.5 hour, placed in 10% sucrose in 0.1M PB at 4°C overnight, and subsequently embedded in gelatin in 30% sucrose (in 0.1M PB). Embedded brains were postfixed for 2.5 to 3 hours in 30% sucrose and 10% formaldehyde (in Milli-Q; Millipore, Billerica, MA) and placed overnight in 30% sucrose (in 0.1M PB) at 4°C. Forty-micrometer-thick transversal slices were serially collected for immunofluorescent 4′,6-diamidino-2-phenylindole (DAPI) staining. To confirm correct localization of the injections, fluorescence was assessed with images captured using a confocal laser scanning microscope (LSM 700; Zeiss, Lambrecht, Germany) at 555nm (Evans blue), 405nm (DAPI), and 488 to 527nm (green fluorescent protein/yellow fluorescent protein range) and optimized for contrast and brightness manually (Zen 2009 software, Zeiss). The fluorescent images were captured using a tile-scan function of the Zen software with a ×10 objective and have been optimized for representation using Adobe Illustrator (Creative Suite 6; Adobe Systems, San Jose, CA).

Data Analyses

OFFLINE GSWD DETECTION. To accurately determine start and end of absence GSWDs and the locations of ECoG spikes (negative ECoG peaks during episodes of GSWDs), a custom-written GSWD detection algorithm (LabVIEW, National Instruments, Austin, TX) was used. In short, we detected those time points in the ECoG for which the first derivative of the filtered ECoG traces (3rd order Butterworth 1Hz high pass) changed polarity. The amplitude differences between each point and both its neighbors were summed to detect fast, continuous amplitude changes and potential GSWDs with a manually set amplitude threshold. Series of GSWDs were marked when: (1) 5 threshold-exceeding data points appeared within 1 second and (2) each of the intervals between the points was <300 milliseconds. Furthermore, we separated GSWDs by applying the following 4 rules: (1) a point is the first spike of a GSWD episode if there are no other spikes in the previous 300 milliseconds, (2) a point is the last spike of a GSWD episode if there are no other spikes in the next 350 milliseconds, (3) the inter-GSWD episode interval is ≥1 second, and (4) the minimal GSWD duration is 1 second.

GSWD DEFINITION. An ictal period is defined as starting at the first ECoG spike of a GSWD and ending at the last ECoG spike. Unless stated otherwise, spike-and-wave discharges that lasted >1 second and appeared in both M1 and S1 were considered GSWDs.

An interictal period is defined as the time in between GSWDs starting 2 seconds after 1 GSWD and ending 2 seconds before the next GSWD.

DETECTION OF ACTION POTENTIALS IN EXTRACELLULAR RECORDINGS. Extracellular recordings were included if activity was well isolated and held stable for >100 seconds. Action potential detection in extracellular traces was performed using threshold-based analyses with customized MATLAB (MathWorks, Natick, MA) routines incorporating principal component analysis of the spike waveform or with the MATLAB-based program SpikeTrain (Neurasmus, Erasmus MC Holding, Rotterdam, the Netherlands).

GSWD-RELATED FIRING PATTERN MODULATION. A custom-written algorithm in LabVIEW was used to assess whether CN neurons showed GSWD-modulated firing patterns during GSWDs in the ECoG of the contralateral primary sensory cortex (in the case of medial CN neurons) or primary motor cortex (in the case of interposed or lateral CN neurons). The minimum duration per episode was set at 2 seconds to construct GSWD-triggered raster plots and peri-GSWD time histograms (PSTHs) with a 5-millisecond bin width, which allowed us to determine: (1) modulation amplitude: the amplitude difference between the peak and trough near $t = 0$; (2) modulation frequency: frequency of the sine wave that fits the PSTH best; and (3) mean power at GSWD frequency: a fast Fourier transform (fft) between 6 and 9Hz (GSWD frequency range). Next, the interspike intervals (ISIs) used for this PSTH were randomly shuffled 500 times and converted into a new PSTH with 5-millisecond bin width to create normal distributions of modulation amplitude and mean power at GSWD frequency. Z scores were calculated for the real and shuffled data by applying: $Z = (X - \mu)/\sigma$, where $X =$ the value based on the original PSTH, $\mu =$ the mean of the bootstrapped normal distribution, and $\sigma =$ its standard deviation (SD). Cells were identified as GSWD modulated if: (1) the modulation amplitude was significantly higher than expected by chance ($Z \geq 1.96$, $p \leq 0.05$), (2) the cell modulated at GSWD frequency (6–9Hz), and (3) the mean power at GSWD frequency was significantly higher than expected by chance ($Z \geq 1.96$, $p \leq 0.05$). Because all CN neurons that showed significant Z scores of mean power at GSWD frequency also showed significantly higher modulation amplitudes, the former was used for further analyses. The term Z score refers to mean power at GSWD frequency unless stated otherwise.

COHERENCE. To determine the spectral coherence between the activity of a CN neuron and the ECoG signal during GSWDs, a custom-written MATLAB routine was used. The extracellular signal was time-binned at 1-millisecond precision, convolved with a sinc(x)-kernel (cutoff frequency = 50Hz) and downsampled to 290 Hz. The ECoG signal was directly downsampled to 290 Hz. The magnitude squared coherence was calculated per GSWD episode using Welch's averaged, modified periodogram method and is defined as: $C_{xy}(f) = |P_{xy}(f)|^2/P_{xx}(f)*P_{yy}(f)$ with the following parameters: window = 290 (Hamming), noverlap = 75%, length of fft (nfft) = 290, sampling frequency = 290 (due to the window size, only GSWDs > 1.5 seconds were considered). The coherence value per GSWD was defined as the maximum coherence in the 6 to 9Hz frequency band; a weighted average per cell based on GSWD duration was used.

FIRING PATTERN PARAMETERS. Firing patterns parameters were assessed using custom-written LabVIEW-based programs calculating firing frequency, coefficient of variation (CV) of ISIs = $\sigma_{\mathrm{ISI}}/\mu_{\mathrm{ISI}}$, $\mathrm{CV2} = 2|ISI_{n+1} - ISI_n|/(ISI_{n+1} + ISI_n)$, and burst index = number of action potentials within bursts/total number of action potentials in a recording, where a burst is defined as ≥3 consecutive action potentials with an ISI ≤ 10 milliseconds. CV reports regularity of firing throughout the whole recording and CV2 quantifies the regularity of firing on a spike-to-spike basis.[38] Firing pattern parameters were specifically calculated for ictal and interictal periods.

REGRESSION ANALYSES OF INTERICTAL CN ACTIVITY. To evaluate whether there is a type of CN neuron that is predisposed for ictal phase-locking during GSWDs, we analyzed the neurons' interictal activity using a custom-made MATLAB routine, aiming to probe the predictability of the ictal activity. We used Gaussian process regression,[39] which is considered to be among the best nonlinear regression methods, to determine whether the GSWD modulation of the activity was predictable from the interictal activity of the neurons. The measures that enabled the prediction of the modulation amplitude most accurately were CV, log-interval entropy, firing frequency, and permutation entropy. The interictal parts of the extracellular recordings were divided into 1-second bins. To calculate the log-interval entropy, in which entropy measures the predictability of a system, first a natural logarithm of the intervals, in milliseconds, was taken to construct a histogram with a bin width of 0.02 log_e (time). Furthermore, a Gaussian convolution was performed using a kernel of one-sixth SD of the *log*(ISIs).

The entropy of the ISI histogram $p(I_i)$ was calculated by:

$$\mathrm{Ent}(I) = -\sum_{i=1}^{N} p(I_i)\log_2 p(I_i) \tag{1}$$

Furthermore, we analyzed the permutation entropy, which is calculated as the predictability of the order of neighboring ISIs rather than the actual values of the ISIs.[40]

NORMALIZED GSWD OCCURRENCE AND DURATION. GSWDs were detected using the offline ECoG detection algorithm described above. Total number of GSWDs and average GSWD duration were calculated and normalized to baseline values.

ASSESSMENT OF CELLULAR RESPONSES TO OPTOGENETIC STIMULATION. Action potentials were detected as described above. A custom-written LabVIEW program was used to construct light-triggered raster plots and peri–stimulus time histograms with a 5-millisecond bin width. Changes in CN neuronal firing rate upon optical stimulation were subsequently determined by calculating the total number of action potentials during light pulses divided by the total length of the pulse and compared with the baseline firing rate (calculated from the total recording time excluding the optogenetic stimulation). In the current study, we consider differences in action potential firing rate exceeding 25% as responsive.

ASSESSMENT OF IMPACT OF OPTOGENETIC CEREBELLAR OUTPUT STIMULATION ON GSWDS. The start and end of seizures were identified using the offline GSWD detection method described above. A custom-written LabVIEW program was used to assess the effectiveness of optogenetic stimulation in stopping GSWDs. Only light pulses triggered prior to the natural end of the seizure were used for analysis. The time difference between the light pulse and the end of the seizure was calculated. The seizure was considered "stopped by the optogenetic stimulation" when this time difference did not exceed 150 milliseconds. Mean power at GSWD frequency (6–9Hz) was calculated using FFT of the ECoG signal recorded during 1-second or 0.5-second (in the case of closed-loop optogenetic stimulation) time periods before and after the light pulse. Averaged responses to light pulses are represented per animal and per stimulus condition by averaging complex Morlet wavelets of 4-second windows ranging from 2 seconds before to 2 seconds after the stimulus.

ASSESSMENT OF ONSET OF OPTICAL CEREBELLAR NUCLEI STIMULATION RELATIVE TO GSWD CYCLE. The time difference between the onset of stimulation and the last spike before stimulation was calculated and divided by the median length of 1 GSWD during that episode, representing 1 cycle of 360°. The outcome was subsequently multiplied by 360. Note that the optogenetic stimuli were not initiated with a fixed delay after the occurrence of an ECoG spike; the delay depended on the visual interpretation and reaction speed of the experimenter (for manual activation of the LED) or on the closed-loop detection system for which the delay depends on the variability of the ECoG directly prior to the GSWDs (see below and van Dongen et al[41]).

CLOSED-LOOP GSWD DETECTION. The GSWD detection system has been implemented using a real-time, digital wavelet-filter setup. The analog pre-filter used for digitization has 4 functions: (1) amplification, (2) offset injection to match the signal to the input range of the analog to digital converter (ADC), (3) artifact removal by using a second-order 0.4Hz high-pass filter, and (4) antialiasing by means of a second-order 23.4Hz low-pass filter. The filter is realized using discrete components on a prototype printed circuit board (PCB). Following the PCB, the wavelet filter functionality is implemented on a TI Sitara AM335x ARM microprocessor (Texas Instruments, Dallas, TX). It first digitizes the signal from the analog filter with its integrated ADC using a sampling frequency of 100Hz. Subsequently the signal is filtered using a wavelet filter and the GSWD episode is detected using signal thresholding. Upon detection an output LED is switched on to stimulate the target area in the cerebellum. Wavelet filters have previously been successfully applied for real-time GSWD detection.[42] Here we applied a complex Morlet wavelet at 6.7Hz that resembled a GSWD. The wavelet filter was implemented as a finite impulse response filter by truncating the ideal complex Morlet wavelet as described earlier.[43] Using the 2 thresholds that are set manually during a recording session, the GSWDs are detected during a positive, high-threshold crossing and the detection is ended upon a negative, low-threshold crossing.

STATISTICAL ANALYSES. Statistical differences in firing pattern parameters between independent groups of CN neuronal recordings (eg, from *tg* mice, their wild-type littermates, GSWD-modulated and non–GSWD-modulated, before and after gabazine injection) were determined using multivariate analyses of variance (MANOVAs) with firing frequency, CV, CV2, and burst index as dependent variables and group as independent variable. When a MANOVA showed a significant result, post hoc analyses of variance (ANOVAs) were used to assess contributions of individual firing pattern parameters with Bonferroni corrected *p*-values.

Differences in coherence value between GWSD-modulated and non–GWSD-modulated cells were assessed using unpaired samples *t* tests. Cochran and Cox adjustment for the standard error of the estimate and the Satterthwaite adjustment for the degrees of freedom were used because equality of variances was not assumed.

Differences in normalized number of GSWD episodes and their duration between traces pre- and postinjection of either muscimol, gabazine, or saline were tested by using nonparametric Friedman ANOVAs with 1 within-subjects factor (ie, time period) with 2 levels (baseline and postinjection).

Differences in mean power at 6 to 9Hz before and after a light pulse were tested using values from all individual pulses by use of repeated measures analysis of covariance (ANCOVA) with 1 within-subjects factor (ie, period) with 2 levels (before and after light pulse) and mouse number added as covariate to correct for variance in the within-subject factor explained by variance between mice. To test whether the time difference between the last ECoG spike before optogenetic stimulation and the subsequent spike deviates from the median interval between 2 ECoG spikes in "stopped seizures," a similar statistical approach was used. A repeated measures ANCOVA was used with 1 within-subject factor with 2 levels, both and ECoG spike intervals. Mouse number was again added as covariate. Because the number of seizures not terminated by the optogenetic stimulation was low, a nonparametric Friedman ANOVA was used to test the same difference.

To determine whether the phase angle of the optogenetic stimulation onset was related to the success rate of stopping GSWDs, we compared the phase angle distribution of successful attempts to that of the unsuccessful attempts. We tested for significant differences between these distributions using the nonparametric 2-sample Kuiper test.

A p-value ≤ 0.05 (α) was considered significant unless Bonferroni correction was used; in that case, a p-value of α/n was considered significant. Two-tailed testing was used for all statistical analyses and all were performed using SPSS 20.0 software (IBM, Armonk, NY). Exact information and outcomes regarding statistical testing are depicted in Tables 1 to 7.

Results

GSWD-Related CN Neuronal Activity

We first investigated whether CN neuronal activity and ECoG were correlated during spontaneous episodes of GSWDs in awake head-fixed homozygous *tg* mice (Fig 1). We found no significant differences in GSWD occurrence ($t_{24} = -0.002$, $p = 0.998$) and GSWD duration ($t_{24} = 0.195$, $p = 0.847$) between male and female *tg* mice, which is in line with data from other experimental animal models of absence epilepsy (reviewed by van Luijtelaar et al[44]). Therefore, we grouped data of both genders. GSWDs appeared simultaneously in bilateral primary motor (M1) and sensory cortices (S1) at 7.6 ± 0.6Hz with an average duration of 3.6 ± 1.4 seconds (n = 17 mice). The GSWD frequency and appearance were comparable to earlier reports of awake *tg* and other rodent models of absence epilepsy.[30,32,34,45] During these GSWDs, action potential firing of a subset of CN neurons was phase-locked to GSWDs. A typical GSWD-modulated CN neuron showed oscillatory action potential firing at GSWD frequency; repetitive firing was observed during the wave in the ECoG, whereas the spike was accompanied by a pause in CN neuronal activity. These GSWD-modulated CN neurons showed significantly increased coherence with ECoG during seizures ($p \leq 0.001$; see Table 1). In each CN type (MCN, IN, and LCN), a substantial portion of the recorded CN neurons showed GSWD-modulated firing, with the highest percentage (73%; 49 of 67 neurons) in the IN and 35% (35 of 100 neurons) and 44% (19 of 43 neurons) in the MCN and LCN, respectively. We found no statistical difference ($p = 0.512$) in the phase of modulation of neuronal firing relative to the GSWD cycle for these 3 nuclei.

To assess whether GSWD-modulated CN neurons differed from non-modulating CN neurons in baseline activity, we compared their interictal firing patterns. During interictal periods GSWD-modulated CN neurons showed a higher firing frequency and a more irregular, burstlike firing pattern compared with non-modulated neurons (p-values < 0.01), and both modulated and non-modulated groups showed a more irregular firing pattern and increased burst index compared to CN neurons recorded from wild-type littermates (p-values < 0.01; see Fig 1G, Table 1). Gaussian process regression[39] revealed that in *tg* mice interictal CN neuronal firing was correlated with the ictal firing pattern; 94% of neurons that phase-locked their activity to GSWDs could be predicted correctly, based on their interictal firing pattern (see Fig 1H). These data indicate that a large subset of neurons within each CN consistently shows seizure-modulated activity, that is, that these GSWD-modulated CN neurons are different from non-modulated neurons in basic, interictal firing patterns and that GSWD-related modulation can be predicted based on these interictal firing patterns.

Impact on GSWD Occurrence of Pharmacological Interventions That Modulate CN Action Potential Firing

CN neurons provide excitatory input to thalamic neurons[4,6,23–29] and thereby potentially contribute to the excitation–inhibition balance that sets thalamic activity patterns. Excess tonic inhibition of thalamic activity has been linked to the occurrence of absence seizures,[3,7,8] and therefore we hypothesized that a decrease in CN output in *tg* should increase the occurrence of GSWDs,

TABLE 1. CN Action Potential Firing

Tested Data	Compared Groups	N	p	t or F-value	Statistical Test
Differences in phase relation between CN modulation and GSWD cycle					
Phase relation	MCN	100	0.512	$F(2,100) = 0.674$	Watson–Williams multiple sample test
	IN	67			
	LCN	43			
Differences in CN neuronal action potential firing					
Coherence	*tg* GSWD-modulated	103	<0.001[a]	$t(195.9) = 13.35$	Independent samples t test
	tg non-modulated	107			
Overall	Wild type	94	<0.001[a]	$F(4,192) = 68.72$	MANOVA (Pillai's trace)
	tg GSWD-modulated interictal	103			
Firing frequency	Wild type	94	0.095	$F(1,195) = 2.81$	ANOVA (Bonferroni)
	tg GSWD-modulated interictal	103			
Coefficient of variation	Wild type	94	<0.001[a]	$F(1,195) = 58.88$	ANOVA (Bonferroni)
	tg GSWD-modulated interictal	103			
CV2	Wild type	94	<0.001[a]	$F(1,195) = 34.63$	ANOVA (Bonferroni)
	tg GSWD-modulated interictal	103			
Burst index	Wild type	94	<0.001[a]	$F(1,195) = 230.86$	ANOVA (Bonferroni)
	tg GSWD-modulated interictal	103			
Overall	Wild type	94	<0.001[a]	$F(4,196) = 16.66$	MANOVA (Pillai's trace)
	tg non-modulated interictal	107			
Firing frequency	Wild type	94	0.092	$F(1,199) = 2.86$	ANOVA (Bonferroni)
	tg non-modulated interictal	107			
Coefficient of variation	Wild type	94	<0.001[a]	$F(1,199) = 15.13$	ANOVA (Bonferroni)
	tg non-modulated interictal	107			
CV2	Wild type	94	<0.01[a]	$F(1,199) = 6.79$	ANOVA (Bonferroni)
	tg non-modulated interictal	107			
Burst index	Wild type	94	<0.001[a]	$F(1,199) = 37.99$	ANOVA (Bonferroni)
	tg non-modulated interictal	107			

TABLE 1: Continued

Tested Data	Compared Groups	N	p	t or F-value	Statistical Test
Overall	*tg* GSWD-modulated interictal	103	<0.001[a]	$F(4,205) = 17.84$	MANOVA (Pillai trace)
	tg non-modulated interictal	107			
Firing frequency	*tg* GSWD-modulated interictal	103	<0.001[a]	$F(1,208) = 16.31$	ANOVA (Bonferroni)
	tg non-modulated interictal	107			
Coefficient of variation	*tg* GSWD-modulated interictal	103	<0.01[a]	$F(1,208) = 7.12$	ANOVA (Bonferroni)
	tg non-modulated interictal	107			
CV2	*tg* GSWD-modulated interictal	103	<0.01[a]	$F(1,208) = 9.47$	ANOVA (Bonferroni)
	tg non-modulated interictal	107			
Burst index	*tg* GSWD-modulated interictal	103	<0.001[a]	$F(1,208) = 62.6$	ANOVA (Bonferroni)
	tg non-modulated interictal	107			

Corresponds to Figure 1.
[a] Statistically significant.
ANOVA = analysis of variance; CN = cerebellar nuclei; GSWD = generalized spike-and-wave discharge; IN = interposed nuclei; LCN = lateral cerebellar nuclei; MANOVA = multivariate analysis of variance; MCN = medial cerebellar nuclei.

whereas increased CN output should have the opposite effect. To test this, we locally applied (see Fig 2, Supplementary Fig) either $GABA_A$-agonist muscimol, which stopped CN neuronal action potential firing (no statistical comparison was possible due to complete cessation of action potential firing), or $GABA_A$-antagonist gabazine (SR-95531), which consistently increased the frequency ($p < 0.01$) and regularity of CN neuronal firing ($p < 0.001$; see Table 2). Upon bilateral CN injections with muscimol, the occurrence of GSWDs increased by 160 to 3,700% postinjection ($p < 0.01$; recorded for 60 minutes; peak of seizure occurrence 34.5 ± 16.5 minutes after injection; n = 10). In contrast, bilateral CN injections with gabazine significantly reduced the occurrence of GSWDs ($p < 0.05$; first seizure occurred 32.5 ± 17.4 minutes after injection; n = 10) and bilateral sham injections did not change GSWD occurrence ($p = 0.18$). The duration of GSWDs was not significantly changed following muscimol, gabazine, or saline injections in the CN (muscimol: $p = 0.21$; gabazine: $p = 0.32$; saline: $p = 0.41$). As a control, we also injected similar quantities of gabazine or muscimol into the cerebellar cortex; this had no significant effect on the GSWD occurrence (p = 0.66 and 0.32, respectively) or duration ($p = 0.66$ for both gabazine and muscimol injections). Thus, pharmacological manipulation of neuronal activity in the CN, but not the cerebellar cortex, is highly effective in modulating the occurrence of GSWDs in *tg* mice. Notably, we observed that muscimol and gabazine were most effective when the injections were in the IN and/or LCN (no statistical difference in impact on GSWD-occurrence after IN and/or LCN injections; $p = 0.70$; Mann–Whitney U test) compared to injections in the MCN ($p = 0.07$ for muscimol and $p < 0.05$ for gabazine; see Supplementary Fig, Table 3). To study whether these differences in impact of pharmacological interventions aimed at the MCN or the IN and LCN were due to a variable effect on neuronal activity, we also performed single unit recordings in the injected CN. Regardless of the injected nucleus, muscimol effectively silenced all action potential firing and gabazine consistently increased the firing frequency and the regularity of action potential firing (all p-values < 0.01 for firing frequency, CV, and CV2; see Table 4). These findings indicate that although effects of muscimol and gabazine on the neuronal activity were similar throughout all CN, the effect of manipulating activity in the IN and LCN seems to exert a larger impact on GSWD-occurrence in the mutants than targeting the

MCN. Instead, pharmacological interventions in the CN of wild-type littermates (n = 2) did not evoke GSWD-episodes (data not shown).

Although it has been shown that pharmacological interventions can have sex-specific differences in animal models of epilepsy[46] that may contribute to the variability of the current results, our ECoG recordings did not show a trend toward a sex-specific impact of CN-specific muscimol or gabazine application (see Fig 2F–H). This finding was corroborated by the finding that muscimol was equally effective in stopping CN action potential

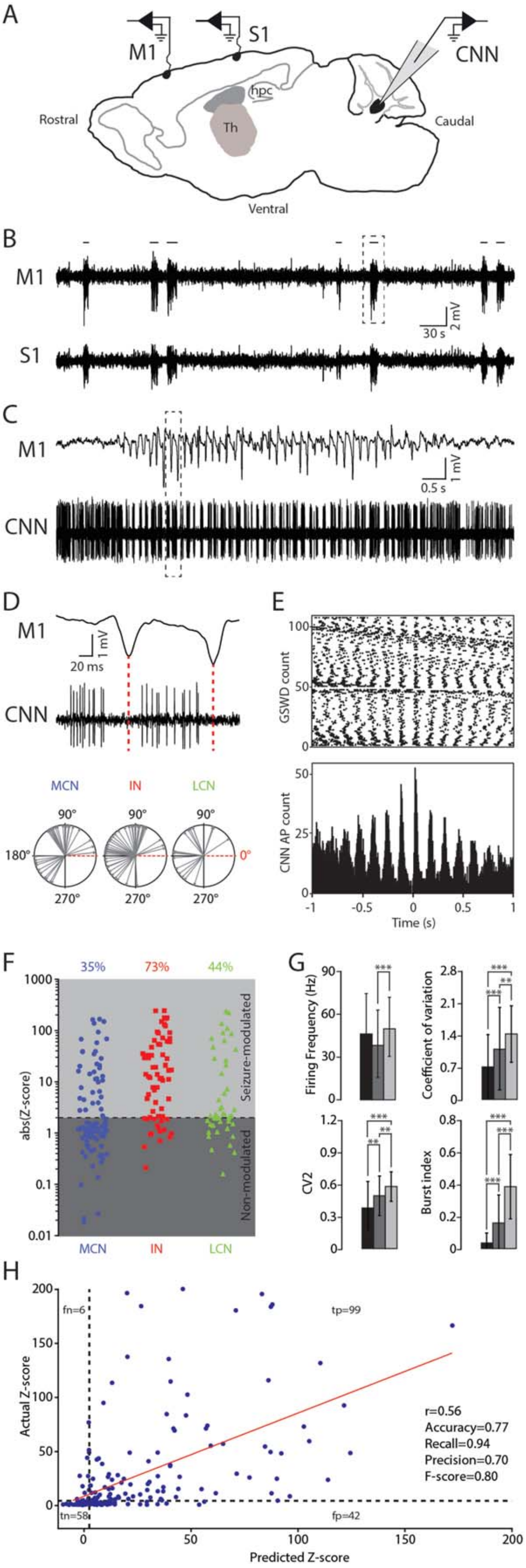

FIGURE 1

FIGURE 1: Cerebellar nuclei (CN) neuronal action potential firing patterns are modulated during generalized spike-and-wave discharges (GSWDs). (A) Schematic of recording sites for electrocorticogram (ECoG) from primary motor (M1) and sensory (S1) cortices and extracellular single unit CN neuronal (CNN) recordings (Th = thalamus, hpc = hippocampus). (B) ECoG from M1 and S1 with GSWD episodes (horizontal lines), indicating absence seizures. (C) Zoom of M1 episode outlined in B and simultaneously recorded action potential firing of a single CN neuron. (D; top panel) Zoom of outlined M1 and CNN recording in C. Red lines align ECoG spike with pause in CNN action potential firing. Bottom panel: Compass plot of phase difference between ECoG spike and modulated CNN action potential firing. IN = interposed nuclei; LCN = lateral CN; MCN = medial CN. (E) Raster plot and accompanying peri–spike-and-wave discharge time histogram of CNN action potentials (AP) for 3 consecutive seizures (t = 0 is aligned with each ECoG spike). (F) Distribution of absolute *Z* scores of mean power at GSWD frequency as determined by fast Fourier transform for MCN, IN, and LCN. Note that none of the negative *Z* scores was below −1.96, and therefore showing absolute *Z* scores does not change the number of data points below and above the 1.96 cutoff score (corresponding to $p < 0.05$; *horizontal dashed line*). Total number of recorded neurons: MCN, n = 100; IN, n = 67; LCN, n = 43. (G) Bar plots representing firing frequency, coefficient of variation, coefficient of variation 2 (CV2), and burst index for CN neurons recorded in wild-type littermate (n = 94; black) and seizure-modulated (n = 103; light gray) and non-modulated CN neurons recorded in *tg* (n = 107; dark gray). For clarity, we truncated the negative error bars. **$p < 0.01$, ***$p < 0.001$ (multivariate analysis of variance, post hoc analyses of variance with Bonferroni correction; see Table 1). (H) Result of the Gaussian process regression to predict the *Z* score from interictal activity parameters (CV, firing frequency, log-interval entropy, and permutation entropy) represented as a confusion matrix. The prediction is characterized as being a true positive (tp) when the predicted *Z* score is >1.96 *(dotted line)* and the actual *Z* score is >1.96. A true negative (tn) is scored when both predicted and actual *Z* scores are <1.96. False positive (fp) and false negative (fn) refer to neurons that have been incorrectly predicted as GSWD modulated and GSWD non-modulated, respectively. Note that we were able to achieve a precision of 0.70 and a recall of 0.94, which means that 70% of CN neurons (n = 210) that were predicted as GSWD modulated actually were GSWD modulated, and 94% of all GSWD-modulated neurons have been identified correctly by the model. The Pearson correlation coefficient (*r*) between the predicted *Z* score and the actual *Z* score was 0.56 with $p \leq 0.05$.

firing in both male and female mice. Together, these effects indicate that in the *tg* animal model of absence epilepsy CN output forms an integral component of the neuronal networks involved in generalized epilepsy and may operate as a potent modulator of GSWD occurrence, irrespective of the gender.

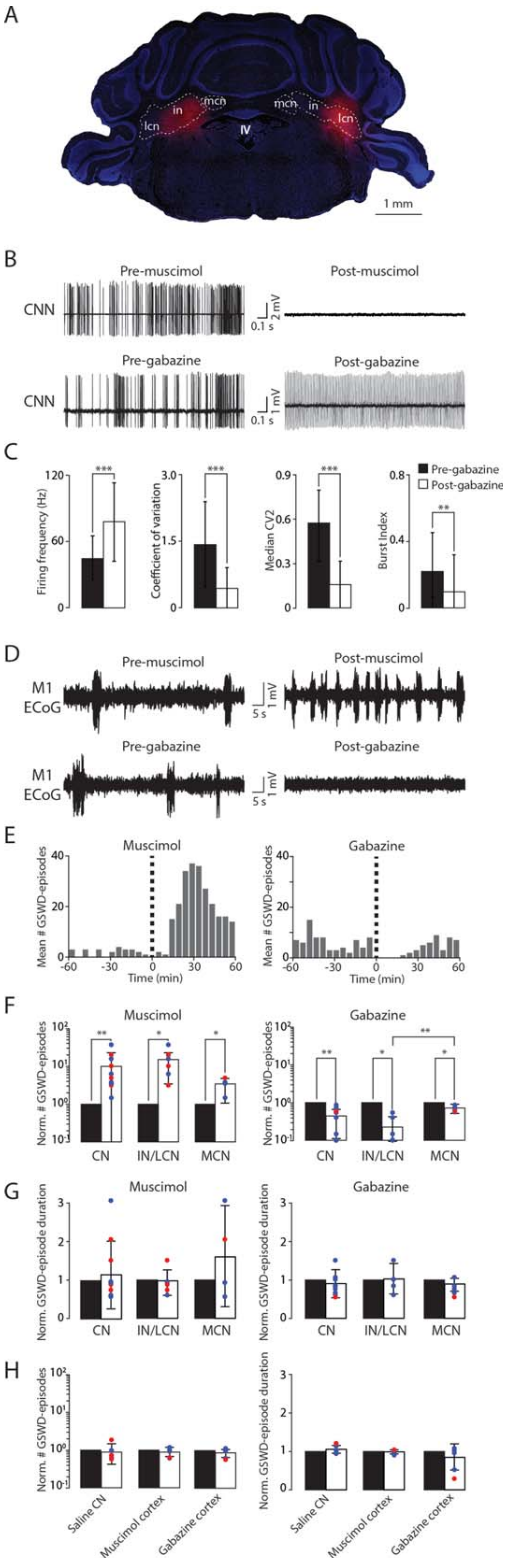

FIGURE 2

Optogenetic Stimulation of Cerebellar Nuclei

The promising impact of long-lasting pharmacological interventions at the level of the cerebellar output prompted us to explore whether short-lasting neuromodulation would be equally effective in stopping GSWDs, that is, whether disrupting oscillatory CN neuronal activity immediately stops GSWDs. To test this hypothesis, we virally expressed light-sensitive ChR2 cation channels in CN neurons (see Fig 3). The optically evoked alteration of CN neuronal firing (see below; Fig 5A) had a robust effect on GSWD occurrence, in that most if not all episodes abruptly stopped within 150 milliseconds of the onset of bilateral stimulation (n = 4; presented per mouse: 76% [male], 84% [female], 92% [female], and 100% [female] stopped) and in that the power at GSWD frequency was significantly reduced ($p < 0.001$; see Fig 3, Table 5). Moreover, unilateral optical stimulation of CN

FIGURE 2: Bimodal modulation of generalized spike-and-wave discharge (GSWD) occurrence by pharmacological manipulation of cerebellar nuclei (CN) neuronal (CNN) action potential firing. (A) Confocal image of coronal cerebellar slice with bilateral muscimol injections (blue = 4′,6-diamidino-2-phenylindole (DAPI); red = Evans blue indicating the injection sites; IN = interposed nucleus; IV = 4th ventricle; LCN = lateral CN; MCN = medial CN). (B) Examples of CNN recordings before and after bilateral muscimol (top) and gabazine (bottom) injections. (C) Bar plots for the impact of gabazine on CNN firing as quantified by the difference between pre- and postgabazine injections (n = 81 and n = 55, respectively) in firing frequency, coefficient of variation, median CV2, and burst index; **$p<0.01$, ***$p<0.001$ (multivariate analysis of variance, post hoc analyses of variance [ANOVAs] with Bonferroni corrections; see Table 2). (D; top) Representative electrocorticogram (ECoG) of primary motor cortex (M1) ECoG before and after muscimol injection; (bottom) representative M1 ECoG before and after gabazine injection. (E) Time course of the effects of muscimol (left) and gabazine (right) on the average number of GSWD episodes (bin size = 5 minutes). (F, G) Normalized number of seizures (F) and normalized seizure duration (G) before and after muscimol (left) and gabazine (right) injections (1 hour each) for bilateral injections in all CN (n = 10 for both gabazine and muscimol), in IN/LCN (n = 6 for muscimol and 5 for gabazine), and in MCN (n = 4 for muscimol and 5 for gabazine). Note that for quantification of the seizure duration after gabazine injection, only 9 mice are included in all CN and 4 mice in the IN/LCN group, because 1 mouse did not show any GSWDs postinjection. Blue dots indicate data recorded from male mice and red dots from female. *$p<0.05$, **$p<0.01$ (Friedman ANOVAs and Mann–Whitney *U* tests; see Tables 2 and 3). (H) Normalized number of GSWD episodes (left) and normalized GSWD episode duration (right) for control experiments; saline injections in the CN and muscimol and gabazine injections in superficial cerebellar cortical areas.

TABLE 2. Impact of Pharmacological Manipulations on CN Firing and GSWD Occurrence

Tested Data	Compared Groups	N	p	F	Statistical Test
Effects of bilateral CN gabazine injections on CNN activity					
Overall	*tg* pregabazine	81	<0.001[a]	$F(4,131) = 39.83$	MANOVA (Pillai's trace)
	tg postgabazine	55			
Firing frequency	*tg* pregabazine	81	<0.001[a]	$F(1,134) = 37.15$	ANOVA (Bonferroni)
	tg postgabazine	55			
Coefficient of variation	*tg* pregabazine	81	<0.001[a]	$F(1,134) = 61.21$	ANOVA (Bonferroni)
	tg postgabazine	55			
CV2	*tg* pregabazine	81	<0.001[a]	$F(1,134) = 117.63$	ANOVA (Bonferroni)
	tg postgabazine	55			
Burst index	*tg* pregabazine	81	<0.01[a]	$F(1,134) = 8.71$	ANOVA (Bonferroni)
	tg postgabazine	55			
Effects of pharmacological manipulations of CN neurons on GSWDs					
GSWD occurrence	*tg* presaline CN	6	0.180		Friedman's ANOVA
	tg postsaline CN				
	tg premuscimol CN	10	<0.01[a]		Friedman's ANOVA
	tg postmuscimol CN				
	tg pregabazine CN	10	<0.01[a]		Friedman's ANOVA
	tg postgabazine CN				
	tg premuscimol cortex	5	0.655		Friedman's ANOVA
	tg postmuscimol cortex				
	tg pregabazine cortex	5	0.317		Friedman's ANOVA
	tg postgabazine cortex				
GSWD duration	*tg* presaline CN	6	0.414		Friedman's ANOVA
	tg postsaline CN				
	tg premuscimol CN	10	0.206		Friedman's ANOVA
	tg postmuscimol CN				
	tg pregabazine CN	10	0.317		Friedman's ANOVA
	tg postgabazine CN				
	tg premuscimol cortex	5	0.655		Friedman's ANOVA
	tg postmuscimol cortex				
	tg pregabazine cortex	5	0.655		Friedman's ANOVA
	tg postgabazine cortex				

Corresponds to Figure 2C, F–H.
[a] Statistically significant.
ANOVA = analysis of variance; CN = cerebellar nuclei; CNN = CN neuronal; GSWD = generalized spike-and-wave discharge; MANOVA = multivariate analysis of variance.

neurons proved equally effective in stopping GSWDs in all recorded cortices, regardless of the laterality (n = 3 females; presented per mouse: 89%, 92%, and 100% stopped; power reduction: $p < 0.001$). Bilateral cerebellar stimulation was ineffective when a different wavelength (590nm) was applied (n = 3 females; presented per

TABLE 3. Impact of Local Pharmacological Manipulations on GSWD Occurrence

Tested Data	Compared Groups	*N*	*p*	Statistical Test
GSWD occurrence pre vs post	*tg* premuscimol IN/LCN	6	$<0.05^a$	Friedman's ANOVA
	tg postmuscimol IN/LCN			
	tg premuscimol MCN	4	$<0.05^a$	Friedman's ANOVA
	tg postmuscimol MCN			
	tg pregabazine IN/LCN	5	$<0.05^a$	Friedman's ANOVA
	tg postgabazine IN/LCN			
	tg pregabazine MCN	5	$<0.05^a$	Friedman's ANOVA
	tg postgabazine MCN			
GSWD occurrence medial vs lateral CN	*tg* postmuscimol IN/LCN	6	0.067	Mann–Whitney *U* test
	tg postmuscimol MCN	4		
	tg postgabazine IN/LCN	5	$<0.01^a$	Mann–Whitney *U* test
	tg postgabazine MCN	5		
GSWD duration pre vs post	*tg* premuscimol IN/LCN	6	0.102	Friedman's ANOVA
	tg postmuscimol IN/LCN			
	tg premuscimol MCN	4	1.00	Friedman's ANOVA
	tg postmuscimol MCN			
	tg pregabazine IN/LCN	5	1.00	Friedman's ANOVA
	tg postgabazine IN/LCN			
	tg pregabazine MCN	5	0.180	Friedman's ANOVA
	tg postgabazine MCN			
GSWD duration medial vs lateral CN	*tg* postmuscimol IN/LCN	6	0.352	Mann–Whitney *U* test
	tg postmuscimol MCN	4		
	tg postgabazine IN/LCN	5	0.413	Mann–Whitney *U* test
	tg postgabazine MCN	5		

Corresponds to Figure 2F–G.
[a]Statistically significant.
ANOVA = analysis of variance; CN = cerebellar nuclei; GSWD = generalized spike-and-wave discharge; IN = interposed nuclei; LCN = lateral cerebellar nuclei; MCN = medial cerebellar nuclei.

mouse: 0%, 0%, and 5% stopped; power reduction: $p = 0.37$) or when the optical fiber was placed outside the CN region (n = 3 females; presented per mouse: 0%, 5%, and 8% stopped; power reduction: $p = 0.28$).

The type of seizure detection and on-demand stimulation described above renders the procedure conceptually unsuitable for clinical implementation in that it would require constant online evaluation and decision making by medics.[47] Therefore, we developed a brain–machine interface (BMI) approach by engineering a closed-loop system for online detection of GSWDs and subsequent optogenetic stimulation.[41] Using offline analysis, we optimized the performance of a wavelet-based GSWD detection filter up to an accuracy of 96.5% and a median latency of 424 milliseconds. When applied online, this on-demand, closed-loop stimulation proved efficient in detecting and stopping GSWDs; bilateral optical stimulation of ChR2-expressing CN neurons stopped 93.4% of GSWDs and unilateral stimulation stopped 91.8% of GSWDs, which is also represented by the GSWD frequency power reduction (n = 3 female; $p < 0.001$; see Fig 3E, F, Table 5). Together, these data highlight that in a clinically applicable BMI setting single pulse stimulation of CN

TABLE 4. Impact of Local Pharmacological Manipulations on CN Spiking Activity

Tested Data	Compared Groups	N	p	F-value	Statistical Test
Overall	*tg* pregabazine IN/LCN	40	<0.001[a]	$F(4,62) = 12.41$	MANOVA (Pillai's trace)
	tg postgabazine IN/LCN	27			
Firing frequency	*tg* pregabazine IN/LCN	40	<0.01[a]	$F(1,65) = 8.80$	ANOVA (Bonferroni)
	tg postgabazine IN/LCN	27			
Coefficient of variation	*tg* pregabazine IN/LCN	40	<0.001[a]	$F(1,65) = 23.18$	ANOVA (Bonferroni)
	tg postgabazine IN/LCN	27			
CV2	*tg* pregabazine IN/LCN	40	<0.001[a]	$F(1,65) = 25.13$	ANOVA (Bonferroni)
	tg postgabazine IN/LCN	27			
Burst index	*tg* pregabazine IN/LCN	40	<0.01[a]	$F(1,65) = 10.22$	ANOVA (Bonferroni)
	tg postgabazine IN/LCN	27			
Overall	*tg* pregabazine MCN	41	<0.001[a]	$F(4,64) = 40.55$	MANOVA (Pillai's trace)
	tg postgabazine MCN	28			
Firing frequency	*tg* pregabazine MCN	41	<0.001[a]	$F(1,67) = 37.53$	ANOVA (Bonferroni)
	tg postgabazine MCN	28			
Coefficient of variation	*tg* pregabazine MCN	41	<0.001[a]	$F(1,67) = 60.04$	ANOVA (Bonferroni)
	tg postgabazine MCN	28			
CV2	*tg* pregabazine MCN	41	<0.001[a]	$F(1,67) = 153.36$	ANOVA (Bonferroni)
	tg postgabazine MCN	28			
Burst index	*tg* pregabazine MCN	41	0.614	$F(1,67) = 0.61$	ANOVA (Bonferroni)
	tg postgabazine MCN	28			
Overall	*tg* pregabazine IN/LCN	40	<0.001[a]	$F(4,76) = 6.28$	MANOVA (Pillai's trace)
	tg pregabazine MCN	41			
Firing frequency	*tg* pregabazine IN/LCN	40	0.438	$F(4,79) = 0.61$	ANOVA (Bonferroni)
	tg pregabazine MCN	41			
Coefficient of variation	*tg* pregabazine IN/LCN	40	0.037	$F(4,79) = 4.51$	ANOVA (Bonferroni)
	tg pregabazine MCN	41			
CV2	*tg* pregabazine IN/LCN	40	0.494	$F(4,79) = 0.47$	ANOVA (Bonferroni)
	tg pregabazine MCN	41			
Burst index	*tg* pregabazine IN/LCN	40	<0.001[a]	$F(4,79) = 13.53$	ANOVA (Bonferroni)
	tg pregabazine MCN	41			
Overall	*tg* postgabazine IN/LCN	27	<0.001[a]	$F(4,50) = 4.29$	MANOVA (Pillai's trace)
	tg postgabazine MCN	28			
Firing frequency	*tg* postgabazine IN/LCN	27	0.344	$F(4,53) = 0.91$	ANOVA (Bonferroni)
	tg postgabazine MCN	28			
Coefficient of variation	*tg* postgabazine IN/LCN	27	≤ 0.001[a]	$F(4,53) = 13.55$	ANOVA (Bonferroni)
	tg postgabazine MCN	28			
CV2	*tg* postgabazine IN/LCN	27	<0.01[a]	$F(4,53) = 10.16$	ANOVA (Bonferroni)
	tg postgabazine MCN	28			
Burst index	*tg* postgabazine IN/LCN	27	0.801	$F(4,53) = 0.64$	ANOVA (Bonferroni)
	tg postgabazine MCN	28			

[a] Statistically significant.

ANOVA = analysis of variance; IN = interposed nuclei; LCN = lateral cerebellar nuclei; MANOVA = multivariate analysis of variance; MCN = medial cerebellar nuclei.

neurons suffices to stop GSWDs and that unilateral stimulation is sufficiently powerful to disrupt bilateral thalamocortical oscillations.

Key Findings Are Replicated in an Unrelated Mouse Model of Absence Epilepsy

To exclude the possibility that our current findings in *tg* are unique to their pathophysiology,[30,48,49] we repeated key experiments in *C3H/HeOuJ*, an inbred strain with an absence epilepsy phenotype[33] that is unrelated to *tg*. Extracellular recordings in awake ECoG-monitored *C3H/HeOuJ* mice confirmed that a smaller but substantial portion (35%) of CN neurons showed phase-locked action potential firing and significant coherence with ECoG ($p < 0.001$) during GSWDs and that this oscillatory firing was more irregular than their interictal firing pattern ($p < 0.001$; Fig 4, Table 6). Similar to *tg* mutants (see Fig 2), *C3H/HeOuJ* mice showed significantly more seizures following local muscimol injections into CN ($p < 0.05$; see Fig 4, Table 6). Moreover, also in *C3H/HeOuJ* mice optogenetic stimulation reliably stopped GSWD episodes (n = 3; presented per mouse: 82%, 87%, and 91% stopped) and both bilateral and unilateral stimuli significantly reduced power at GSWD frequency ($p < 0.01$ and $p < 0.001$, respectively); the closed-loop detection and intervention system reduced the GSWD frequency power ($p < 0.001$ for bilateral and $p < 0.05$ for unilateral stimulation); and neither optical stimulation at 590nm nor stimulation outside of CN significantly reduced the GSWD frequency power ($p = 0.43$ and $p = 0.81$, respectively). Thus, the main findings from CN treatment of absence seizures in *tg* could be replicated in *C3H/HeOuJ* mutants.

Optogenetic Stimulation of Presumptively Excitatory CN Neurons Affects GSWDs

To investigate the mechanism underlying the potent interruption of GSWDs by optogenetic stimulation of CN in *tg* and *C3H/HeOuJ*, we quantified the responses of CN neurons to bilateral optical stimulation. In *C3H/HeOuJ* and *tg* injected with AAV2-hSyn-ChR2(H134R)-EYFP, 33 of 50 responsive cells (66%) showed increased action potential firing, whereas 17 (34%) showed decreased firing (see Fig 5A). A further 16 recorded neurons showed no response to optical stimulation. This variety of responses is in line with the properties of the construct that was used to transfect CN neurons with ChR2. Because human synapsin (hSyn) is not specific to a certain type of neuron,[50] both excitatory and inhibitory CN neurons expressed ChR2. Excitatory responses can

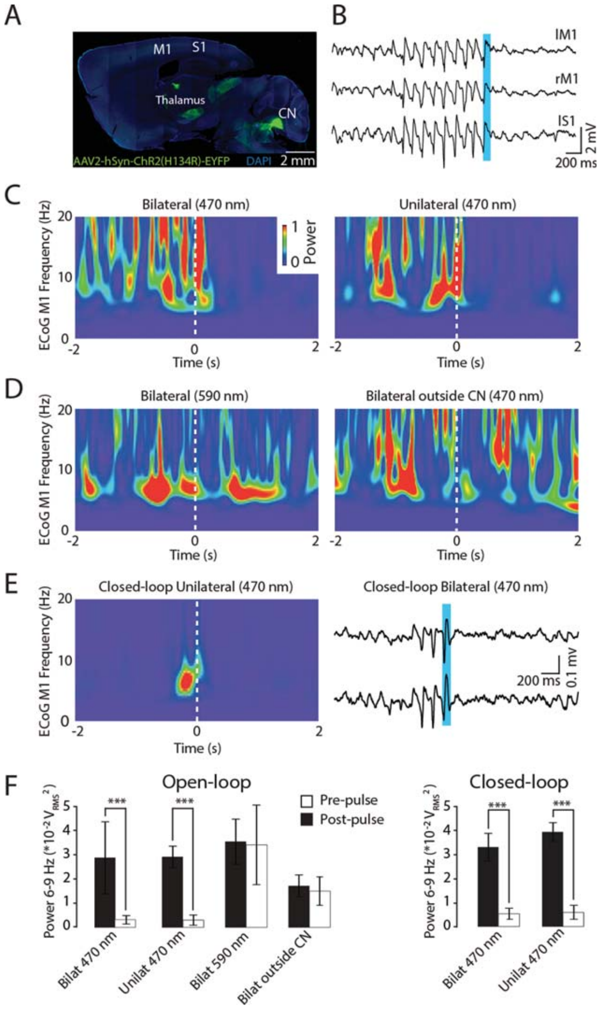

FIGURE 3

FIGURE 3: Optogenetic stimulation of cerebellar nuclei reliably stops generalized spike-and-wave discharges (GSWDs). (A) Confocal image of sagittal brain section showing channelrhodopsin-2 (ChR2) expression in cerebellar nuclei (CN) with projections to the thalamus (M1, S1 represent primary motor and sensory cortex, respectively). (B) Representative electrocorticogram (ECoG) of bilateral M1 (left M1 [lM1], right [rM1], and left S1 [lS1] recording), which exemplifies how bilateral optogenetic stimulation (470nm light pulse of 100 milliseconds indicated by the *vertical blue bar*) stops GSWDs in all recorded cortices. (C) Mean ECoG wavelet spectrogram of contralateral M1 for all bilateral (n = 25; left panel) and unilateral stimuli (n = 11; right panel) presented to a single mouse at 470nm. (D) As in C for (left) 590nm stimuli (n = 36) and (right) stimulation at 470nm outside of CN (n = 18). (E; right) Typical example of the effect of bilateral closed-loop stimulation on GSWD recorded in contralateral M1 and S1 and (left) mean ECoG wavelet spectrogram of all unilateral stimuli (n = 44) presented to 1 mouse. (F) ECoG theta-band power before and after open-loop (bilateral: 3 females, 1 male, n = 178; unilateral: 3 female, n = 43) stimulations with the wrong wavelength (590nm; 3 females, n = 107) and stimulations outside the CN (3 females; n = 185) as well as the responses to closed-loop stimulation at 470nm in the CN (bilateral: 3 females, n = 227; unilateral: 3 females, n = 49). ***$p < 0.001$ (repeated measures analysis of covariance; see Table 5).

TABLE 5. Effect of Optogenetic CN Stimulation on GSWD-Related Power

Tested Data	Compared Groups	N	p	F-value	Statistical Test
Open-loop bilateral 470nm	*tg* prestimulation	178	<0.001[a]	$F(1,176) = 74.87$	Repeated measures ANCOVA
	tg poststimulation				
Open-loop unilateral 470nm	*tg* prestimulation	43	<0.001[a]	$F(1,41) = 35.25$	Repeated measures ANCOVA
	tg poststimulation				
590nm	*tg* prestimulation	107	0.367	$F(1,65) = 0.82$	Repeated measures ANCOVA
	tg poststimulation				
470nm outside CN	*tg* prestimulation	185	0.283	$F(1,65) = 1.16$	Repeated measures ANCOVA
	tg poststimulation				
Closed-loop bilateral 470nm	*tg* prestimulation	227	<0.001[a]	$F(1,65) = 456.3$	Repeated measures ANCOVA
	tg poststimulation				
Closed-loop unilateral 470nm	*tg* prestimulation	49	<0.001[a]	$F(1,65) = 97.58$	Repeated measures ANCOVA
	tg poststimulation				

Corresponds to Figure 3.
[a] Statistically significant.
ANCOVA = analysis of covariance; CN = cerebellar nuclei; GSWD = generalized spike-and-wave discharge.

be recorded from neurons that express ChR2, and inhibitory responses can be recorded from neurons that do not express ChR2 but that receive input from ChR2-positive inhibitory neurons, but neurons devoid of ChR2 expression either in their membrane or synaptic afferents will not show any response.

Next, we questioned to what extent the impact of optogenetic stimulation of CN neuronal action potential firing depends on the phase of the thalamocortical oscillations, that is, to what extent the disruption of GSWD-modulated CN firing was evoked during cortical excitation (the ECoG spike) and/or cortical inhibition (the ECoG wave).[51] Because we did not design our stimulation protocol to be activated with a fixed delay relative to the GSWDs, we could answer this question by comparing the phase values of the onset of effective stimuli relative to the spike-and-wave cycle in M1 and S1 cortices with those of ineffective stimuli (see Fig 5). For both M1 and S1, success rates were lowest when the stimulus was applied up to 60° before the peak of a spike (ie, 300°–360° in Fig 5C lower panels), but the overall differences of these distributions did not reach statistical significance (M1: $p = 0.13$; S1: $p = 0.29$). However, effective stimuli evoked a significant shortening ($p < 0.01$) of the interval between the last 2 ECoG spikes, which is indicative of an excitatory effect on cortical activity (Fig. 5D),[51] and the timing of the last ECoG spike could be predicted by the time of the stimulus onset relative to the spike-and-wave cycle ($p < 0.001$; see Fig 5E, Table 7). Together, our combined electrophysiological and optogenetic data indicate that optogenetic CN stimulation is most effective when applied during the "wave" of the GSWD, during which cortical neurons are normally silent.

Discussion

In this study, we show that in 2 unrelated mouse models of absence epilepsy the activity of CN neurons can be utilized to modulate the occurrence of GSWDs. We provide evidence that pharmacological interventions at the level of CN can exert slow, but long-term, effects and that optogenetic stimulation of CN neurons can exert fast, short-term control. The different dynamics of these experimental approaches, with converging outcomes, align with the hypothesis that CN neurons can control the balance of excitation and inhibition in the thalamus, thereby resetting the oscillatory activity in thalamocortical loops. In both *tg* and *C3H/HeOuJ* strains of mice, a substantial subset of CN neurons showed phase-locked action potential firing during GSWDs, which is in line with a previous study of oscillating cerebellar activity during GSWDs in WAG/Rij and F344/BN rats.[32] We observed that 35% of neuronal recordings in the MCN showed GSWD-modulated patterns, whereas the portions

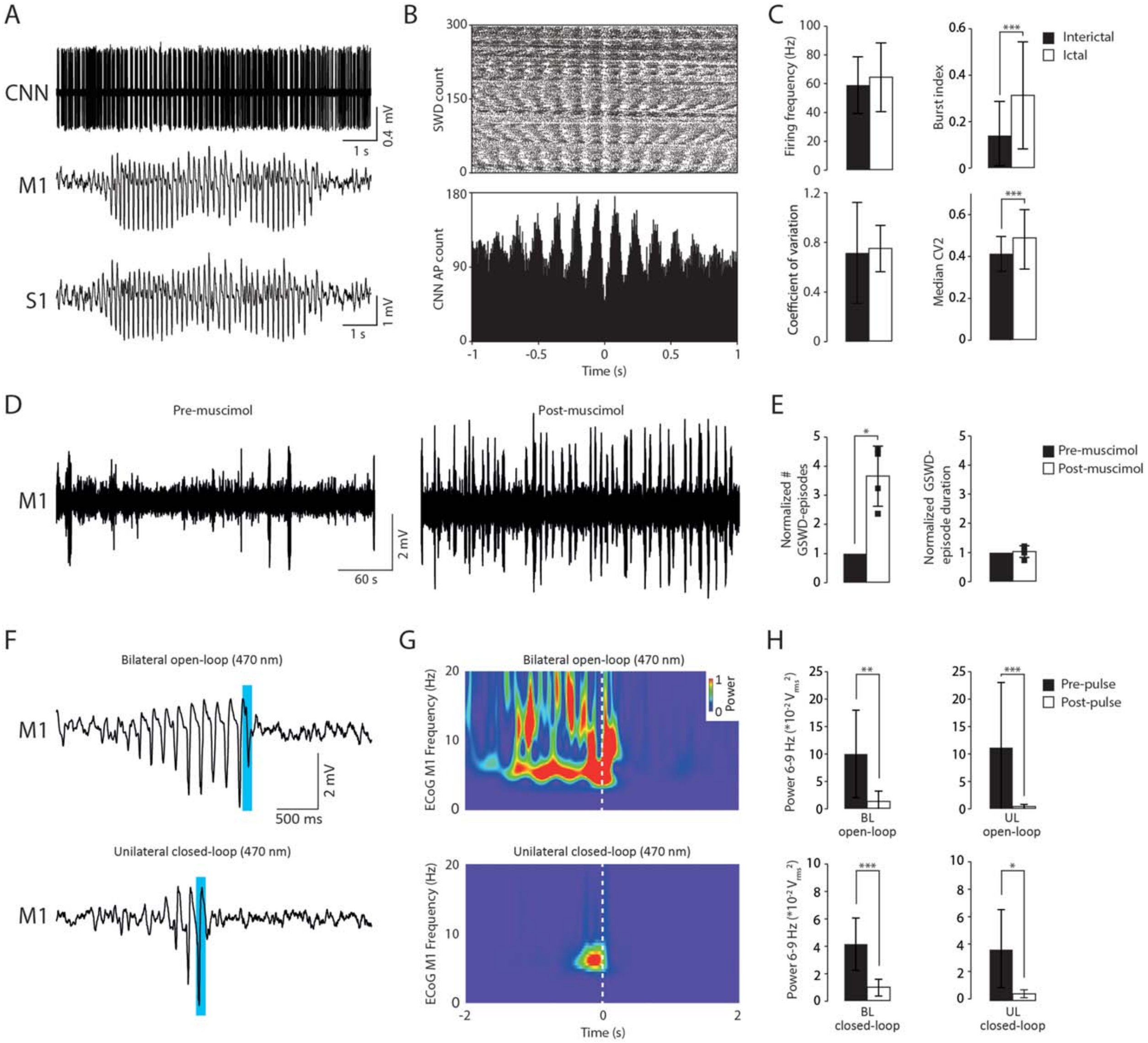

FIGURE 4: Modulation of phase-locked cerebellar nuclei (CN) neuronal (CNN) activity stops generalized spike-and-wave discharges (GSWDs) in *C3H/HeOuJ mice*. (A) Simultaneously recorded primary motor (M1) and sensory (S1) cortex electrocorticograms (ECoGs) and CNN activity. (B) Raster plot and peri–stimulus time histogram of single CNN activity (t = 0 indicates each ECoG spike). AP = action potential; SWD = spike-and-wave discharge. (C) Summary bar plots representing the mean differences in firing pattern parameters between interictal and ictal periods (n = 28). ****p* < 0.001 (repeated measures analysis of variance [ANOVA] with Bonferroni corrections; see Table 6). (D) Representative M1 ECoG before and after muscimol injection and (E) corresponding normalized seizure occurrence and duration. **p* < 0.05 (Friedman ANOVA; see Table 6). (F–H) Open-loop (top) and closed-loop (bottom) optogenetic stimulation stops GSWDs as shown by: (F) typical example trace; (G) ECoG wavelet spectrogram averaged over all bilateral open-loop (n = 11; top panel) stimuli in a single mouse and over all unilateral closed-loop stimuli (n = 18; bottom panel) in another mouse; and (H) ECoG theta-band power before and after optical stimulation for bilateral open-loop stimuli (n = 3 mice, n = 19 stimulations; top left panel), unilateral open-loop stimuli (n = 3 mice, n = 19 stimulations), bilateral closed- loop stimuli (n = 3 mice, n = 46 stimulations), and unilateral closed-loop stimuli (n = 3 mice, n = 30 stimulations). **p* < 0.05, ***p* < 0.01 ****p* < 0.001 (repeated measures ANCOVA; see Table 6).

of GSWD-modulated neurons in the IN and LCN were higher (73% and 44%, respectively). Except for an anatomical evaluation of the local density of large and small soma-diameter CN neurons in the mouse brain[52] and computational studies on the clustering analysis of CN neuronal action potential firing in *tg*,[53,54] few experimental data are available that allow us to unequivocally pinpoint the type(s) of CN neurons responsible for modification of GSWD activity. With respect to the extracellular recordings, we presumably recorded mostly

TABLE 6. Neuronal Firing and Effect of CN Manipulations on GSWD Occurrence

Tested Data	Compared Groups	*N*	*p*	*t* or *F*-value	Statistical Test
Differences in CN neuronal action potential firing					
Coherence	*C3H/HeOuJ* GSWD-modulated	28	$<0.001^a$	$t(66.6) = 5.92$	Independent samples *t* test
	C3H/HeOuJ non-modulated	51			
Firing frequency	*C3H/HeOuJ* GSWD-modulated ictal	28	0.138	$F(1,27) = 2.34$	Repeated measures ANOVA (Bonferroni)
	C3H/HeOuJ GSWD-modulated interictal				
Coefficient of variation	*C3H/HeOuJ* GSWD-modulated ictal	28	0.708	$F(1,27) = 0.14$	Repeated measures ANOVA (Bonferroni)
	C3H/HeOuJ GSWD-modulated interictal				
CV2	*C3H/HeOuJ* GSWD-modulated ictal	28	$<0.001^a$	$F(1,27) = 21.35$	Repeated measures ANOVA (Bonferroni)
	C3H/HeOuJ GSWD-modulated interictal				
Burst index	*C3H/HeOuJ* GSWD-modulated ictal	28	$<0.001^a$	$F(1,27) = 15.64$	Repeated measures ANOVA (Bonferroni)
	C3H/HeOuJ GSWD-modulated interictal				
Effects of pharmacological manipulations of CN neurons on GSWDs					
GSWD occurrence	*C3H/HeOuJ* premuscimol	4	$<0.05^a$		Friedman's ANOVA
	C3H/HeOuJ postmuscimol				
GSWD duration	*C3H/HeOuJ* premuscimol	4	0.317		Friedman's ANOVA
	C3H/HeOuJ postmuscimol				
Effects of optogenetic CN stimulation on GSWD-related power					
Open-loop bilateral 470nm	*C3H/HeOuJ* prestimulation	37	$<0.01^a$	$F(1,35) = 8.17$	Repeated measures ANCOVA
	C3H/HeOuJ poststimulation				
Open-loop unilateral 470nm	*C3H/HeOuJ* prestimulation	19	$<0.001^a$	$F(1,17) = 20.32$	Repeated measures ANCOVA
	C3H/HeOuJ poststimulation				
590nm in CN	*C3H/HeOuJ* prestimulation	47	0.809	$F(1,45) = 0.06$	Repeated measures ANCOVA
	C3H/HeOuJ poststimulation				

TABLE 6: Continued

Tested Data	Compared Groups	N	p	t or F-value	Statistical Test
470nm outside CN	*C3H/HeOuJ* prestimulation	56	0.425	$F(1,54) = 0.65$	Repeated measures ANCOVA
	C3H/HeOuJ poststimulation				
Closed-loop bilateral 470nm	*C3H/HeOuJ* prestimulation	46	<0.001[a]	$F(1,44) = 14.20$	Repeated measures ANCOVA
	C3H/HeOuJ poststimulation				
Closed-loop unilateral 470nm	*C3H/HeOuJ* prestimulation	30	<0.05[a]	$F(1,28) = 4.60$	Repeated measures ANCOVA
	C3H/HeOuJ poststimulation				

Corresponds to Figure 4.
[a] Statistically significant.
ANCOVA = analysis of covariance; ANOVA = analysis of variance; CN = cerebellar nuclei; GSWD = generalized spike-and-wave discharge.

from CN neurons with a large soma-diameter,[55] which incorporates mainly excitatory glutamatergic neurons,[56] but in the MCN also inhibitory glycinergic projection neurons.[57] Interestingly, GSWD-modulated CN neurons also showed characteristic firing patterns during the periods in between seizures. During these interictal periods, they fired at higher frequencies with a more irregular and burstlike pattern than the CN neurons that did not comodulate with GSWDs. Thus, the interictal firing pattern of CN neurons in *tg* and *C3H/HeOuJ* mice appears to reliably predict whether these cells will show oscillations phase-locked to GSWDs during seizures.

Pharmacological manipulation of neuronal activity in the cerebellum proved effective when the injections of muscimol or gabazine were aimed at the CN, but not when the cerebellar cortex was targeted.

We found that gabazine application was effective in reducing GSWD occurrence in all CN, with the most pronounced effects in IN and LCN. Along the same line, muscimol injections in IN and LCN evoked the biggest increase in GSWD occurrence. Effects of MCN injections were smaller but still significant. Because we know little about the density of individual types of neurons throughout the murine MCN, IN, and LCN,[52,56] and considering the similarity in effects of gabazine and muscimol on neuronal activity in these nuclei, we cannot draw a firm conclusion about a potentially differential effect of either gabazine or muscimol on the respective nuclei. These data raise the possibility that the difference in impact on GSWD occurrence between manipulation of MCN versus that of IN and LCN does not reflect a difference in intrinsic activity, but rather a difference in their efferent projections to the brainstem, midbrain, and thalamus.[24] Although all CN have been shown to project to a wide range of thalamic subnuclei, such as the ventrolateral, ventromedian, centrolateral, centromedian, and parafascicular nuclei,[24,58] and thereby connect to a variety of thalamocortical networks, the impact of IN and LCN has been shown to focus on the primary motor cortex, whereas MCN impact more diffusely on thalamocortical networks.[59]

CN axons that project to the thalamus have been shown to originate from glutamatergic neurons, which synapse predominantly perisomatically and evoke substantial excitatory responses.[4,6,23–29] Upon CN injections with muscimol, we must in effect have substantially reduced the level of excitation of thalamic neurons and thereby disturbed the balance of inhibition and excitation in thalamocortical networks in favor of inhibition. One of the main consequences of hyperpolarizing the membrane potential of thalamic neurons through this inhibition is activation of hyperpolarization-activated depolarizing cation currents (I_h) and $Ca_V3.1$ (T-type) Ca^{2+} channel currents, which typically results in the burstlike action potential firing that can drive GSWDs in thalamocortical networks.[7,8,60,61] Moreover, in *tg* thalamic relay neurons show increased T-type Ca^{2+} channel currents,[62] which probably act synergistically with the decreased excitation following muscimol treatment, likely further increasing GSWD occurrence. In contrast, when we applied gabazine to CN, the balance of inhibition and excitation in the thalamocortical networks probably shifted toward excitation and thereby may have prevented the activation of I_h and T-type Ca^{2+} channel currents, reducing the occurrence of burst firing and GSWDs. The successful application of short periods of optogenetic excitation of CN neurons not only confirmed the deoscillating impact of gabazine, but further refined it by revealing that GSWDs can be most efficiently stopped when the interval between ECoG spikes, that is, wavelength of the oscillations, is instantly shortened and thereby reset. Given the relatively low success rate of optogenetic stimulation in the period just preceding the "spike" state of the GSWDs, which reflects the excitation state of the thalamocortical relay neurons, it is parsimonious to explain the effective resetting through optimal interference during the inhibitory or "wave" state of the GSWD.[51] This explanation centered on the resetting hypothesis argues against the possibility that GSWDs were terminated by optogenetic activation of the CN neurons that were inhibited. Regardless of the net effect of CN stimulation on thalamocortical networks, the current approach proved equally effective when applied bilateral or unilateral. Most likely, instantly resetting the balance of excitation and inhibition in thalamocortical relay neurons on one side of the brain will also engage the other side through combined ipsi- and contralateral projections from the CN to the thalamus and through interthalamic and intercortical connections.[6,24,63]

It remains to be established to what extent the current findings for absence epilepsy can help to treat epileptic patients suffering from other types of seizures. Our findings on the impact of optogenetic manipulation of CN firing patterns on GSWD occurrence seem to support the (pre)-clinical studies that apply deep brain stimulation (DBS)[64,65] in the CN may be an option to treat epilepsy patients. So far, only 3 clinical studies applying electrical DBS to the CN have been reported, which is in contrast to the dozens of studies performed to investigate the therapeutic use of cerebellar surface stimulation (as reviewed by Krauss and Koubeissi[66]). Although

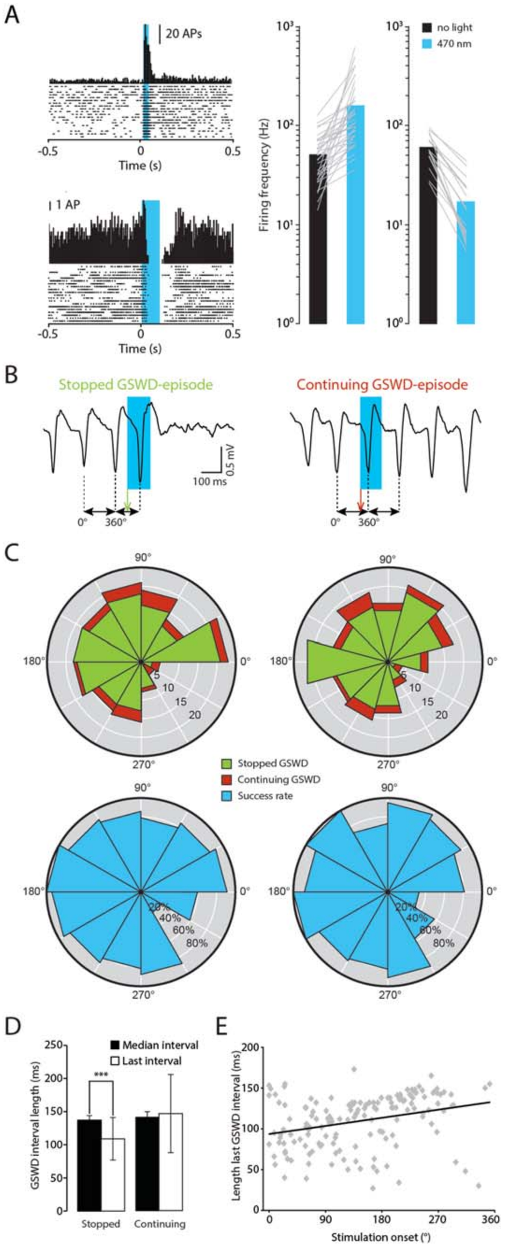

FIGURE 5

FIGURE 5: Excitatory impact of optical cerebellar nuclei (CN) stimulation on cortical activity stops generalized spike-and-wave discharge (GSWD) episodes. (A; left panels) Peri–stimulus time histogram and raster plot indicating increased (top) or decreased (bottom) action potential (AP) firing for individual CN neurons evoked by 470nm light pulses *(blue bars)*. Right panels: Scatterplots represent the individual changes in CN neuronal firing following optical stimulation: (left) increased firing ($n = 33$); (right) decreased firing ($n = 17$). Black and blue bars indicate mean firing frequency when the 470nm light-emitting diode was turned off or on, respectively. (B) Examples of stopped (left) and continuing (right) GSWD episodes upon optogenetic stimulation. Black horizontal arrows represent the median time interval between electrocorticogram (ECoG) spikes, which correspond to 1 cycle of cortical oscillation, here represented as 360°. Green and red vertical arrows represent the onset of the light stimulus. (C) Rose plots of the start of successful and unsuccessful optical stimulation in the 360° GSWD cycle for both primary motor cortex (left) and primary sensory cortex (right). (D) Comparison between the median and the last interval (between the last 2 ECoG spikes) for stopped and continuing GSWD episodes. ***$p < 0.001$ (repeated measures ANCOVA; see Table 7). (E) Scatterplot representing the predictability of the stimulus-related time interval between GSWDs by the phase of stimulation onset. $p < 0.001$ (linear regression analysis; see Table 7).

TABLE 7. Effect of Optogenetic CN Stimulation on ECoG

Tested Data	Compared Groups	*N*	*p*	*F* or *t*-value	Statistical Test
Effects of optogenetic CN stimulation on the time interval between ECoG spikes in M1					
Stopped seizures	Median interval	153	<0.001[a]	$F(1,151) = 99.80$	Repeated measures ANCOVA
	Stimulus-related interval				
Continuing seizures	Median interval	25	0.088		Friedman's ANOVA
	Stimulus-related interval				
Effects of optogenetic CN stimulation on the time interval between ECoG spikes in S1					
Stopped seizures	Median interval	153	<0.01[a]	$F(1,151) = 7.22$	Repeated measures ANCOVA
	Stimulus-related interval				
Continuing seizures	Median interval	25	0.201		Friedman's ANOVA
	Stimulus-related interval				
Predictability of stimulus-related time interval by phase of stimulation onset					
Stopped seizures		153	<0.001[a]	$t(152) = 3.87$	Linear regression

Corresponds to Figure 5.
[a]Statistically significant.
ANCOVA = analysis of covariance; ANOVA = analysis of variance; CN = cerebellar nuclei; ECoG = electrocorticogram.

initially promising, the clinical studies on the effects of cerebellar surface stimulation reported inconsistent results,[12–21] which may partially be due to suboptimal placement of electrodes. Unlike the current results, which show a regional preference for the effect of lateral CN stimulation on GSWD occurrence, it was recently shown that manipulating Purkinje cells in the medial cerebellum is most effective in controlling kainate-induced temporal lobe epilepsy.[67] So far, the studies that applied DBS at the level of CN in an uncontrolled fashion report highly effective decreases in the level of seizures (corresponding to class IC and IIIA of the Engel scale[68]) in a low number of patients characterized with various types of epilepsy.[69–71] Apart from the coherence in location of stimulation (laterally located nucleus dentatus), these studies used a wide variety in CN stimulus regimes, ranging from 3 minutes per day to continuous electrical stimulation for 12 to 14 hours per day. It appears that high-frequency stimulation (>50Hz), but not low-frequency stimulation (1–40Hz), is most effective when applied to the cerebellar dentate nucleus. In the present study, we found that the increase in CN neuronal action potential firing frequency upon optogenetic stimulation was highly variable (see Fig 4), and thus our current results do not provide any ground for a conclusion on whether low- or high-frequency stimulation would be advantageous to stop GSWD episodes. However, our results do provide sufficient data to conclude that the temporal precision determines the level of efficiency, for example, by stimulating with short pulses as soon as an epileptic event starts to occur and if possible in a proper temporal relation with respect to the inhibitory wave of the GSWDs.

Because absence epilepsy is a commonly prevalent but in essence a benign form of generalized epilepsy,[1] DBS will not very likely be considered as a serious option. However, patients diagnosed with other forms of epilepsy who do not benefit sufficiently from medication may be eligible for (cerebellar) DBS.[47] Currently, the options for applying DBS are limited; only the anterior thalamic nucleus is currently described in the US Food and Drug Administration guidelines to treat intractable epilepsy, and although promising, the outcome is limited and can result in cognitive and emotional problems.[72,73] Given the powerful impact of CN stimulation on thalamocortical activity that is shown in the present study, we hypothesize that CN stimulation may also exert very positive effects in these other, more severe kinds of epilepsies.

Acknowledgment

Support was provided by the Netherlands Organization for Scientific Research (NWO)-ALW, MAGW, ZON-MW

(A.M.J.M.v.d.M, C.I.D.Z., F.E.H.); an EU "EUROHEADPAIN" grant (602633; A.M.J.M.v.d.M); LUMC Fellowship, Marie Curie Career Integration grant and CURE SUDEP research award (E.A.T.); the Center for Medical Systems Biology in the framework of the Netherlands Genomics Initiative (A.M.J.M.v.d.M.); Neuro-Basic, European Research Counsel (ERC)-Advanced, and ERC-POC (C.I.D.Z.); and NWO-VENI, NWO-VIDI, and EUR-Fellowship (F.E.H.).

We thank Dr K. Deisseroth for providing the AAV-hSyn-ChR2(H134R)-EYFP construct and Dr T. J. Ruigrok, Dr L. Bosman, Dr P. Holland, Dr. K. Voges, R. Seepers, E. Haasdijk, E. Goedknegt, M. Rutteman, D. Groeneweg, and P. Plak for technical assistance and/or constructive discussions.

Authorship

L.K., O.H.J.E.R., and F.E.H. conceived and designed the study and performed all recordings; L.K., O.H.J.E.R., P.A., J.K.S., E.A.T., C.S., N.D., B.H.J.W., M.N., V.S., C.I.D.Z., and F.E.H. designed the analyses; L.K., O.H.J.E.R., P.A., J.K.S., and F.E.H. performed the analyses; M.N.v.D., A.K., C.S., and W.A.S. designed the closed-loop circuit; W.A.S, V.S., A.M.J.M.v.d.M., C.I.D.Z., and F.E.H contributed financial support; L.K., O.H.J.E.R., P.A., E.A.T, V.S., A.M.J.M.v.d.M., C.I.D.Z., and F.E.H. cowrote the manuscript. L.K. and O.H.J.E.R. contributed equally. C.I.D.Z. and F.E.H. contributed equally and are co-senior authors.

Potential Conflicts of Interest

Nothing to report.

References

1. Berg AT, Berkovic SF, Brodie MJ, et al. Revised terminology and concepts for organization of seizures and epilepsies: report of the ILAE Commission on Classification and Terminology, 2005–2009. Epilepsia 2010;51:676–685.
2. Jallon P, Loiseau P, Loiseau J. Newly diagnosed unprovoked epileptic seizures: presentation at diagnosis in CAROLE study. Coordination Active du Reseau Observatoire Longitudinal de l' Epilepsie. Epilepsia 2001;42:464–475.
3. Snead OC III. Basic mechanisms of generalized absence seizures. Ann Neurol 1995;37:146–157.
4. Norden AD, Blumenfeld H. The role of subcortical structures in epilepsy. Epilepsy Behav 2002;3:219–231.
5. Paz JT, Bryant AS, Peng K, et al. A new mode of corticothalamic transmission revealed in the Gria4(-/-) model of absence epilepsy. Nat Neurosci 2011;14:1167–1173.
6. Jones EG. The thalamus. 2nd ed. New York, NY: Cambridge University Press, 2007.
7. Blumenfeld H, McCormick DA. Corticothalamic inputs control the pattern of activity generated in thalamocortical networks. J Neurosci 2000;20:5153–5162.
8. Cope DW, Di Giovanni G, Fyson SJ, et al. Enhanced tonic GABAA inhibition in typical absence epilepsy. Nat Med 2009;15:1392–1398.
9. Huguenard JR, McCormick DA. Thalamic synchrony and dynamic regulation of global forebrain oscillations. Trends Neurosci 2007; 30:350–356.
10. Paz JT, Davidson TJ, Frechette ES, et al. Closed-loop optogenetic control of thalamus as a tool for interrupting seizures after cortical injury. Nat Neurosci 2013;16:64–70.
11. Berényi A, Belluscio M, Mao D, Buzsàki G. Closed-loop control of epilepsy by transcranial electrical stimulation. Science 2012;337: 735–737.
12. Cooper IS. Effect of chronic stimulation of anterior cerebellum on neurological disease. Lancet 1973;1:206.
13. Cooper IS, Amin I, Riklan M, et al. Chronic cerebellar stimulation in epilepsy. Clinical and anatomical studies. Arch Neurol 1976;33: 559–570.
14. Cooper IS, Riklan M, Watkins S, McLellan D. Safety and efficacy of chronic stimulation. Neurosurgery 1977;1:203–205.
15. Dow RS, Smith W, Maukonen L. Clinical experience with chronic cerebellar stimulation in epilepsy and cerebral palsy. Electroencephalogr Clin Neurophysiol 1977;43:906.
16. Gilman S, Dauth GW, Tennyson VM, et al. Clinical, morphological, biochemical, and physiological effects of cerebellar stimulation. In: Functional electrical stimulation: applications in neural prosthesis. 5th ed. Hambrecht FT, ed. New York, NY: Marcel Dekker, 1977.
17. Levy LF, Auchterlonie WC. Chronic cerebellar stimulation in the treatment of epilepsy. Epilepsia 1979;20:235–245.
18. Bidziński J, Bacia T, Ostrowski K, Czarkwiani L. Effect of cerebellar cortical electrostimulation on the frequency of epileptic seizures in severe forms of epilepsy. Neurol Neurochir Pol 1981;15: 605–609.
19. Wright GD, McLellan D, Brice JG. A double-blind trial of chronic cerebellar stimulation in twelve patients with severe epilepsy. J Neurol Neurosurg Psychiatry 1984;47:769–774.
20. Van Buren JM, Wood JH, Oakley J, Hambrecht F. Preliminary evaluation of cerebellar stimulation by double-blind stimulation and biological criteria in the treatment of epilepsy. J Neurosurg 1978;48:407–416.
21. Velasco F, Carrillo-Ruiz JD, Velasco M, et al. Double-blind, randomized controlled pilot study of bilateral cerebellar stimulation for treatment of intractable motor seizures. Epilepsia 2005;46: 1071–1081.
22. De Zeeuw CI, Hoebeek FE, Bosman LWJ, et al. Spatiotemporal firing patterns in the cerebellum. Nat Rev Neurosci 2011;12:327–344.
23. Aumann TD, Horne MK. Ramification and termination of single axons in the cerebellothalamic pathway of the rat. J Comp Neurol 1996;376:420–430.
24. Teune TM, Van der Burg J, Van der Moer J, Ruigrok TJ. Topography of cerebellar nuclear projections to the brain stem in the rat. Prog Brain Res 2000;124:141–172.
25. Sawyer SF, Tepper JM, Groves PM. Cerebellar-responsive neurons in the thalamic ventroanterior-ventrolateral complex of rats: light and electron microscopy. Neuroscience 1994;63:725–745.
26. Sawyer SF, Young SJ, Groves PM, Tepper JM. Cerebellar-responsive neurons in the thalamic ventroanterior-ventrolateral complex of rats: in vivo electrophysiology. Neuroscience 1994; 63:711–724.
27. Uno M, Yoshida M, Hirota I. The mode of cerebello-thalamic relay transmission investigated with intracellular recording from cells of

the ventrolateral nucleus of cat's thalamus. Exp Brain Res 1970;10: 121–139.

28. Shinoda Y, Futami T, Kano M. Synaptic organization of the cerebello-thalamo-cerebral pathway in the cat. II. Input-output organization of single thalamocortical neurons in the ventrolateral thalamus. Neurosci Res 1985;2:157–180.

29. Bava A, Manzoni T, Urbano A. Effects of fastiginal stimulation on thalamic neurones belonging to the diffuse projection system. Brain Res 1967;4:378–380.

30. Noebels JL, Sidman RL. Spike-wave and focal motor seizures in the mutant mouse tottering. Science 1979;204:1334–1336.

31. Fletcher CF, Lutz CM, O'Sullivan TN, et al. Absence epilepsy in tottering mutant mice is associated with calcium channel defects. Cell 1996;87:607–617.

32. Kandel A, Buzsáki G. Cerebellar neuronal activity correlates with spike and wave EEG patterns in the rat. Epilepsy Res 1993;16:1–9.

33. Tokuda S, Beyer BJ, Frankel WN. Genetic complexity of absence seizures in substrains of C3H mice. Genes Brain Behav 2009;8: 283–289.

34. Marescaux C, Vergnes M, Depaulis A. Genetic absence epilepsy in rats from Strasbourg—a review. J Neural Transm Suppl 1992; 35:37–69.

35. Kaplan BJ, Seyfried TN, Glaser GH. Spontaneous polyspike discharges in an epileptic mutant mouse (tottering). Exp Neurol 1979;66:577–586.

36. Hoebeek FE, Witter L, Ruigrok TJ, De Zeeuw CI. Differential olivo-cerebellar cortical control of rebound activity in the cerebellar nuclei. Proc Natl Acad Sci U S A 2010;107:8410–8415.

37. Loureiro M, Cholvin T, Lopez J, et al. The ventral midline thalamus (reuniens and rhomboid nuclei) contributes to the persistence of spatial memory in rats. J Neurosci 2012;32:9947–9959.

38. Holt GR, Softky WR, Koch C, Douglas RJ. Comparison of discharge variability in vitro and in vivo in cat visual cortex neurons. J Neurophysiol 1996;75:1806–1814.

39. Rasmussen CE, Williams CKI. Gaussian processes for machine learning. Cambridge, MA: MIT Press, 2006.

40. Bandt C, Pompe B. Permutation entropy: a natural complexity measure for time series. Phys Rev Lett 2002;88:174102.

41. van Dongen MN, Karapatis A, Kros L, et al. An implementation of a wavelet-based seizure detection filter suitable for realtime closed-loop epileptic seizure suppression. Paper presented at: Biomedical Circuits and Systems Conference (BioCAS), 2014 IEEE, pp. 504–507; October 22–24, 2014; Lausanne, Switzerland.

42. Osorio I, Frei MG, Wilkinson SB. Real-time automated detection and quantitative analysis of seizures and short-term prediction of clinical onset. Epilepsia 1998;39:615–627.

43. Karel JMH, Haddad SAP, Hiseni S, et al. Implementing wavelets in continuous-time analog circuits with dynamic range optimizatio-n.IEEE Trans Circuits Syst I 2012;59:229–242.

44. van Luijtelaar G, Onat FY, Gallagher MJ. Animal models of absence epilepsies: what do they model and do sex and sex hormones matter? Neurobiol Dis 2014;72(pt B):167–179.

45. van Luijtelaar G, Zobeiri M. Progress and outlooks in a genetic absence epilepsy model (WAG/Rij). Curr Med Chem 2014;21:704–721.

46. Akman O, Moshe SL, Galanopoulou AS. Sex-specific consequences of early life seizures. Neurobiol Dis 2014;72(pt B): 153–166.

47. Fisher RS, Velasco AL. Electrical brain stimulation for epilepsy. Nat Rev Neurol 2014;10:261–270.

48. Hoebeek FE, Khosrovani S, Witter L, De Zeeuw CI. Purkinje cell input to cerebellar nuclei in tottering: ultrastructure and physiology. Cerebellum 2008;7:547–558.

49. Hoebeek FE, Stahl JS, Van Alphen AM, et al. Increased noise level of Purkinje cell activities minimizes impact of their modulation during sensorimotor control. Neuron 2005;45:953–965.

50. Nathanson JL, Yanagawa Y, Obata K, Callaway EM. Preferential labeling of inhibitory and excitatory cortical neurons by endogenous tropism of adeno-associated virus and lentivirus vectors. Neuroscience 2009;161:441–450.

51. Polack PO, Charpier S. Intracellular activity of cortical and thalamic neurones during high-voltage rhythmic spike discharge in Long-Evans rats in vivo. J Physiol 2006;571:461–476.

52. Heckroth JA. Quantitative morphological analysis of the cerebellar nuclei in normal and lurcher mutant mice. I. Morphology and cell number. J Comp Neurol 1994;343:173–182.

53. Alva P, Kros L, Maex R, et al. A potential role for the cerebellar nuclei in absence seizures. BMC Neurosci 2013;14(suppl 1): 170.

54. Alva P, Kros L, Eelkman Rooda OHJ, et al. Combining machine learning and simulations of a morphologically realistic model to study modulation of neuronal activity in cerebellar nuclei during absence epilepsy. BMC Neurosci 2014;15(suppl 1):P39.

55. Rowland NC, Jaeger D. Coding of tactile response properties in the rat deep cerebellar nuclei. J Neurophysiol 2005;94:1236–1251.

56. Uusisaari M, Knopfel T. Functional classification of neurons in the mouse lateral cerebellar nuclei. Cerebellum 2011;10:637–646.

57. Bagnall MW, Zingg B, Sakatos A, et al. Glycinergic projection neurons of the cerebellum. J Neurosci 2009;29:10104–10110.

58. Aumann TD, Rawson JA, Finkelstein DI, Horne MK. Projections from the lateral and interposed cerebellar nuclei to the thalamus of the rat: a light and electron microscopic study using single and double anterograde labelling. J Comp Neurol 1994; 349:165–181.

59. Steriade M. Two channels in the cerebellothalamocortical system. J Comp Neurol 1995;354:57–70.

60. Andersen P, Eccles JC, Sears TA. The ventro-basal complex of the thalamus: types of cells, their responses and their functional organization. J Physiol 1964;174:370–399.

61. Destexhe A, Contreras D, Steriade M. Mechanisms underlying the synchronizing of corticothalamic feedback through inhibition of thalamic relay cells. J Neurophysiol 1998;79: 999–1016.

62. Zhang Y, Mori M, Burgess DL, Noebels JL. Mutations in high-voltage-activated calcium channel genes stimulate low-voltage-activated currents in mouse thalamic relay neurons. J Neurosci 2002;22:6362–6371.

63. Chan-Palay V. Cerebellar dentate nucleus: organization, cytology and transmitters. Heidelberg, Germany: Springer-Verlag, 1977.

64. Chow BY, Boyden ES. Optogenetics and translational medicine. Sci Transl Med 2013;5:177ps5.

65. Creed M, Pascoli VJ, Luscher C. Addiction therapy. Refining deep brain stimulation to emulate optogenetic treatment of synaptic pathology. Science 2015;347:659–664.

66. Krauss GL, Koubeissi MZ. Cerebellar and thalamic stimulation treatment for epilepsy. Acta Neurochir Suppl 2007;97:347–356.

67. Krook-Magnuson E, Szabo GG, Armstrong C, et al. Cerebellar directed optogenetic intervention inhibits spontaneous

hippocampal seizures in a mouse model of temporal lobe epilepsy. Eneuro 2014;1:1–15.

68. Engel J Jr. Outcome with respect to epileptic seizures. Milton J, Jung P, eds. New York, NY: Raven Press, 1987.

69. Chkhenkeli SA, Šramka M, Lortkipanidze GS, et al. Electrophysiological effects and clinical results of direct brain stimulation for intractable epilepsy. Clin Neurol Neurosurg 2004; 106:318–329.

70. Šramka M, Chkhenkeli IS. Clinical experience in intraoperational determination of brain inhibitory structures and application of implanted neurostimulators in epilepsy. Stereotact Funct Neurosurg 1990;54–55:56–59.

71. Šramka M, Fritz G, Galanda M, Nádvorník P. Some observations in treatment stimulation of epilepsy. Acta Neurochir (Wien) 1976; (23 suppl):257–262.

72. Fisher RS. Therapeutic devices for epilepsy. Ann Neurol 2012;71: 157–168.

73. Hartikainen KM, Sun L, Povivaara M, et al. Immediate effects of deep brain stimulation of anterior thalamic nuclei on executive functions and emotion-attention interaction in humans. J Clin Exp Neuropsychol 2014;36:540–550.